Systematic study of separators to improve the performance of passive air-breathing flat-plate microbial fuel cells

by

Sona Kazemi

M.A.Sc., Sharif University of Technology, 2008

B.Sc., Sharif University of Technology, 2005

A THESIS SUBMITTED IN PARTIAL FULFILLMENT OF

THE REQUIREMENTS FOR THE DEGREE OF

DOCTOR OF PHILOSOPHY

in

THE FACULTY OF GRADUATE AND POSTDOCTORAL STUDIES

(Chemical and Biological Engineering)

THE UNIVERSITY OF BRITISH COLUMBIA

(Vancouver)

January 2014

Abstract

Passive air-breathing microbial fuel cells (MFC) are a promising technology for energy recovery from wastewater. The performance of the passive air breathing MFCs is dependent on the separator characteristics, isolating the anaerobic anode from the air-breathing cathode. The separator plays a more important role when the electrodes are placed in close proximity, to reduce the Ohmic resistance.

The goal of the present work was to study the separator characteristics and its effect on the performance of passive air-breathing flat-plate MFCs (FPMFCs), through a combination of experimental and theoretical approaches. This was performed through characterization of 8 separators to investigate the ionic resistivity, oxygen and ethanol crossover, and proton transport number. The separators were then examined in three passive air-breathing FPMFCs with different electrode spacing, using three-dimensional graphite felt anodes and platinum-based cathodes. A numerical model was developed based on the mixed potential theory to investigate the sensitivity of the electrode potentials and the power output to the separator characteristics.

The separator characterization indicated a greater susceptibility to oxygen and ethanol crossover in diaphragms, compared to the ion-exchange membranes (IEMs). Increasing the electrode spacing was also shown to be desirable for the application of diaphragms, as the anodic mixed potentials were reduced.

The peak power density decreased by increasing the mass transfer coefficients of oxygen and ethanol in the separator. The model indicated that this was due to the increased mixed potentials at the anode, caused by the oxygen crossover. The mixed potentials at the cathode did not vary as

the ethanol crossover increased, due to the slow kinetics of ethanol oxidation over Pt. The model also indicated that the peak power was affected by the proton transport number of the separator, which affected the cathode pH. The peak power was not sensitive to the resistivity of the separator due to the overshadowing effect of the oxygen crossover.

The passive air-breathing FPMFC, using a 6 mm thick graphite felt anode, Pt-based cathode, and Nafion®117 membrane, showed the highest peak power density of ca. 0.52 W/m^2, which was higher than those reported for the active air flow FPMFCs in the literature.

Preface

This PhD thesis is divided into 9 chapters. Chapters 4 and 5 have been submitted to peer-reviewed journals, and the materials in Chapters 6, 7, and 8 are being prepared in the manuscript format for publication.

The literature review, experimental design, laboratory work, numerical modeling, data processing and analysis, and thesis preparation was done by Sona Kazemi under the supervision and final approval of Prof. Madjid Mohseni in the Chemical and Biological Engineering Department at the University of British Columbia (UBC) and Dr. Khalid Fatih in the Energy, Mines, and Environment Portfolio at the National Research Council Canada (NRC). The list of the publications is presented as follows:

A version of chapter 4 was submitted as:

1. Kazemi, Sona; Mohseni, Madjid; and Fatih, Khalid; "Passive air-breathing flat-plate microbial fuel cell operation"; Journal of Chemical Technology and Biotechnology, accepted, 2013.

A version of chapter 5 was submitted as:

2. Kazemi, Sona; Fatih, Khalid; and Mohseni, Madjid; "Improved performance of a passive air-breathing flat-plate microbial fuel cell"; submitted, 2013.

A version of chapters 6 and 8 is in preparation as:

3. Kazemi, Sona; Mohseni, Madjid; and Fatih, Khalid; "The important role of separator in the passive air-breathing flat-plate MFCs- part 1"; to be submitted, 2013.

A version of chapter 7 is in preparation as:

4. Kazemi, Sona; Fatih, Khalid; Madjid Mohseni; and Melissa Barazandegan; "The important role of separator in the passive air-breathing flat-plate MFCs- part 2"; to be submitted, 2013.

For the aforementioned publications, all experiments were performed by Sona Kazemi and the numerical model was co-developed by Melissa Barazandegan. All manuscripts were co-authored by Prof. Madjid Mohseni and Dr. Khalid Fatih.

Table of Contents

List of Tables

List of Figures

List of Symbols

Symbol	Definition	Unit
R	Universal Gas Constant	J/mol/K
T	Temperature	K
F	Faraday Constant	C/mol
M_s	Molecular Weight of the Substrate	kg/mol
V	Volume of the Glass Cell	m^3
$\Delta c_{H^+}^{anode}$	Change in the Concentration of Protons in the Anode	mol/m^3
f	Wastewater Flowrate	m^3/s
d	Electrode Spacing	m
σ	Effective Conductivity of the Electrode Matrix	S/m
A	Geometric Surface Area of the Electrode	m^2
a	Specific Surface Area of the Electrode	m^2/m^3
L	Thickness of the Electrode	m
ε	Porosity of the Electrode	-
x	Distance through the Electrode	m
φ	Effectiveness of the Electrode	-
n_{H^+}	Proton Transport Number of the Separator	-
κ_E	Conductivity of Wastewater	S/m
κ	Effective Conductivity of Wastewater	S/m
R_Ω	Ohmic Resistance	$\Omega.m^2$
R_S	Ionic Resistivity of the Separator	$\Omega.m^2$
κ_S	Ionic Conductivity of the Separator	S/m

Z_{im}	Imaginary Component of the Impedance	Ω
Z_{re}	Real Component of the Impedance	Ω
q	Electric Charge	C
E_{cell}	Cell Voltage	V
E_{Ohm}	Ohmic Overpotential	V
E	Operating Electrode Potential	V vs. SHE
E_c	Cathode Potential	V vs. SHE
E_a	Anode Potential	V vs. SHE
E^0	Potential in the Solution Phase	V vs. SHE
E_e°	Standard Half-Cell Potential of the Reaction at 298 K	V vs. SHE
E_{c_e}	Equilibrium Potential of the Reduction Reaction	V vs. SHE
E_{EtOH}^0	Standard half-cell Potential of Ethanol Oxidation at 298 K	V vs. SHE
E_{EtOH}^a	Equilibrium Potential of Ethanol Oxidation at the Anode	V vs. SHE
E_{EtOH}^c	Equilibrium Potential of Ethanol Oxidation at the Cathode	V vs. SHE
$E_{O_2}^0$	Standard half-cell Potential of Oxygen Reduction at 298K	V vs. SHE
$E_{O_2}^a$	Equilibrium Potential of Oxygen Reduction at the Anode	V vs. SHE
$E_{O_2}^c$	Equilibrium Potential of Oxygen Reduction at the Cathode	V vs. SHE
n	Number of Electrons Exchanged in the redox Reaction	-
n_{es}	Moles of Electrons Released per Mole of Substrate	-
n_{EtOH}	Number of Electrons Exchanged in Ethanol Oxidation	-
n_{O_2}	Number of Electrons Exchanged in Oxygen Reduction	-
ΔC	Change in the Substrate Concentration	Kg/m^3
C	Concentration	M

C_F	Concentration of Fuel	M
C_O	Concentration of the Oxidizing Species	M
C_R	Concentration of the Reducing Species	M
C_{EtOH}^{c}	Ethanol Concentration at the Cathode	M
C_{EtOH} or C_{EtOH}^{a}	Ethanol Concentration at the Anode	M
C_{in}	Ethanol Concentration in the Inlet stream	M
C_{out}	Ethanol Concentration in the Outlet stream	M
C_{O_2}	Oxygen Concentration at the Cathode	M
$C_{O_2}^{a}$	Oxygen Concentration at the anode	M
P_{O_2}	Oxygen Partial Pressure at the Cathode	atm
pH_{out}	Outlet pH	-
pH_{in}	Inlet pH	-
$[H^+]_a$	Protons Concentration at the Anode	M
$[H^+]_c$	Protons Concentration at the Cathode	M
$[OH^-]_a$	Hydroxyls Concentration at the Anode	M
$[OH^-]_c$	Hydroxyls Concentration at the Cathode	M
η_c	Cathode Overpotential	V
η_a	Anode Overpotential	V
η_{EtOH}^{a}	Overpotential of Ethanol Oxidation at the Anode	V
η_{EtOH}^{c}	Overpotential of Ethanol Oxidation at the Cathode	V
$\eta_{O_2}^{a}$	Overpotential of Oxygen Reduction at the Anode	V
$\eta_{O_2}^{c}$	Overpotential of Oxygen Reduction at the Cathode	V

P	Electrical Power	Watt
I	Electrical Current	A
j	Local Faradic Current Density	A/m^2
j_S	Current Density in the Solution Phase	A/m^2
j_E	Current Density in the Electrode Matrix	A/m^2
J'	Measured Current Density	A/m^2
J	Predicted Current Density	A/m^2
J_{EtOH}^{c}	Current Density of Ethanol Oxidation at the Cathode	A/m^2
J_{EtOH}^{a}	Current Density of Ethanol Oxidation at the Anode	A/m^2
$J_{O_2}^{c}$	Current Density of Oxygen Reduction at the Cathode	A/m^2
$J_{O_2}^{a}$	Current Density of Oxygen Reduction at the Anode	A/m^2
J_{EtOH}^{amt}	Limiting Current Density of Ethanol Oxidation at the Anode	A/m^2
J_{EtOH}^{act}	Kinetically Controlled Current Density of Ethanol Oxidation at the Anode	A/m^2
J_{EtOH}^{cmt}	Limiting Current Density of Ethanol Oxidation at the Cathode	A/m^2
J_{EtOH}^{cct}	Kinetically Controlled Current Density of Ethanol Oxidation at the Cathode	A/m^2
$J_{O_2}^{amt}$	Limiting Current Density of Oxygen Reduction at the Anode	A/m^2
$J_{O_2}^{amt}$	Kinetically Controlled Current Density of Oxygen Reduction at the Anode	A/m^2
$J_{O_2}^{amt}$	Limiting Current Density of Oxygen Reduction at the Cathode	A/m^2
$J_{O_2}^{amt}$	Kinetically Controlled Current Density of Oxygen Reduction at the Cathode	A/m^2
j^0	Exchange Current Density	A/m^2

$j^0_{B_{EtOH}}$	Exchange Current Density of Ethanol Oxidation in the biofilm	A/m^2
$j^0_{B_{O_2}}$	Exchange Current Density of Oxygen Reduction in the biofilm	A/m^2
j^0_{EtOH}	Exchange Current Density of Ethanol Oxidation on Pt	A/m^2
$j^0_{O_2}$	Exchange Current Density of Oxygen Reduction on Pt	A/m^2
D_O or D_{O_2}	Diffusion Coefficient of Oxygen in the Separator	m^2/s
D_A	Diffusion Coefficient of Acetate in the Separator	m^2/s
D_E or D_{EtOH}	Diffusion Coefficient of Ethanol in the Separator	m^2/s
k_O or k_{O_2}	Mass Transfer Coefficient of Oxygen in the Separator	m/s
k_A	Mass Transfer Coefficient of Acetate in the Separator	m/s
k_E or k_{EtOH}	Mass Transfer Coefficient of Ethanol in the Separator	m/s
K^a_{EtOH}	Effective Mass Transfer Coefficient of Ethanol at the Anode	m/s
$K^a_{O_2}$	Effective Mass Transfer Coefficient of Oxygen at the Cathode	m/s
K^c_{EtOH}	Effective Mass Transfer Coefficient of Ethanol at the Anode	m/s
$K^c_{O_2}$	Effective Mass Transfer Coefficient of Oxygen at the Cathode	m/s
K^B_{EtOH}	Mass Transfer Coefficient of Ethanol in the Biofilm	m/s
$K^B_{O_2}$	Mass Transfer Coefficient of Oxygen in the Biofilm	m/s
$D^E_{O_2}$	Diffusion Coefficient of Oxygen in the Electrolyte	m/s
$K^C_{O_2}$	Mass Transfer Coefficient of Oxygen in the Cathode	m/s
α	Electron Transfer Coefficient	-
$\alpha_{A^A_{EtOH}}$	Anodic Charge Transfer Coefficient of Ethanol Oxidation at the Anode	-
$\alpha_{A^C_{EtOH}}$	Anodic Charge Transfer Coefficient of Ethanol Oxidation at the Cathode	-

$\alpha_{C_{O_2}^{A}}$	Cathodic Charge Transfer Coefficient of Ethanol Oxidation at the Anode	-
$\alpha_{C_{O_2}^{C}}$	Cathodic Charge Transfer Coefficient of Ethanol Oxidation at the Cathode	-
F_{obj}	Objective Function	-

List of Abbreviations

Symbol	Definition
2 mm FPMFC	Flat-Plate Microbial Fuel Cell with Anode Chamber Depth of 2×10^{-3} m
4 mm FPMFC	Flat-Plate Microbial Fuel Cell with Anode Chamber Depth of 4×10^{-3} m
8 mm FPMFC	Flat-Plate Microbial Fuel Cell with Anode Chamber Depth of 8×10^{-3} m
2D	Two-Dimensional
3D	Three-Dimensional
AEM	Anion-Exchange Membrane
AD	Anaerobic Digestion
AS	Activated Sludge
BOD	Biological Oxygen Demand
BPM	Bipolar Membrane
BUG	Bentic Underwater Generator
CE	Coulombic Efficiency
CEM	Cation-Exchange Membrane
COD	Chemical Oxygen Demand
CNC	Computer Numerical Control
DI	De-Ionized

DMFC	Direct Methanol Fuel Cell
DO	Dissolved Oxygen
EFC	Enzaymatic Fuel Cell
EIS	Electrochemical Impedance Spectroscopy
EtOH	Ethanol
FPMFC	Flat-Plate Microbial Fuel Cell
GDE	Gas Diffusion Electrode
GF	Graphite Felt
HFC	Hydrogen Fuel Cell
HPLC	High-Performance Liquid Chromatography
IEM	Ion-Exchange Membrane
MFC	Microbial Fuel Cell
NA	Not Available
NS	No Space
OCV	Open Circuit Voltage
ORR	Oxygen Reduction Reaction
PBS	Phosphate Buffer Solution
PD	Power Density
PEM	Proton Exchange Membrane

PES	Poly Ether Sulfone
PTFE	Poly Tetra Fluoro-Ethylene
RI	Refractive Index
RT	Residence Time
SEM	Scanning Electron Microscopy
SPEEK	Sulfonate Poly Ether Ether Ketone
SQP	Sequential Quadratic Programming
TOC	Total Organic Carbon
UFM	Ultrafiltration Membrane
wt.%	Weight Percent

Acknowledgements

I extend my deepest gratitude to my supervisors, Prof. Madjid Mohseni and Dr. Khalid Fatih, for their mentorship and expertise. Working with them over the past five years has strengthened my ability to critically analyze and tackle complex problems; a skill valuable not only in scientific research, but also in many aspects of my life. Their patience, advice, and trust have been invaluable.

My appreciation goes out to my committee members, Prof. Colin Oloman, Prof. Loretta Li, and Dr. Haijiang Wang, for their critical thoughts. I am especially thankful to Prof. Colin Oloman, whose guidance with the model has strengthened the foundation of my project.

My appreciation also goes out to

Ms. Melissa Barazandegan, Ms. Parisa Mirjafari, Dr. Alfred Lam, and Dr. Arman Bonakdarpour, for their kind assistance at different stages of my PhD.

Mr. Derrick Horne, the research associate of UBC bio-imaging facility, Mr. Richard Ryoo, the store manager of CHBE, Ms. Helsa Leong, the graduate secretary of CHBE, and Mr. Ivan Leversage, the safety officer of CHBE, for their support and patience during my PhD.

Prof. David Wilkinson, Prof. Sue Baldwin, and Prof. Elod Gyenge, for allowing me to use their laboratories and facilities.

Ms. Vanesa Alzate, Mr. Tom Vanderhoek, and Mr. Andrew Mattie from NRC, for their guidance and support during my PhD.

I am especially thankful to my peers and friends, Clara, Gustavo, Bradley, Mohammad Mehdi, Ran, Ramin, Sonia, Rob, Fahimeh, Asefeh, Saman, and the Najafy family for their friendship and support.

Last but not the least; I am deeply grateful to my best friends:

My loving parents, Homa and Mostafa, who continue to grow and inspire me each and every day.

My cool, intelligent, and loving brothers and sister, Shahin, Kaveh, and Solmaz, who have always been there for me.

My beautiful and lively nieces and nephew, Baran, Ana, and Barish, who have taught me to live life fully.

My loving partner, Amin, who has been with me on this long journey always believing in me and providing balance in my life.

Thank you for your endless love and support.

To my loving family

Chapter 1: Introduction

1.1 Microbial fuel cell technology

There is a substantial amount of organic matter in wastewater[1] [1], which is removed utilizing a considerable amount of energy. The high energy consumption of the traditional biological treatment technologies such as the activated sludge (AS) process is one of the issues coupled with the current treatment systems. Aeration has the principal contribution to the total energy consumption of the treatment plants using the AS process (ca. 0.5 kWh/m^3 [2]). In addition, handling of the solids produced during the aerobic processes such as the AS can be costly. A potential solution to address the high energy consumption of the current biological treatment systems can potentially be through replacing the traditional AS process with anaerobic microbial fuel cells (MFC).

A microbial fuel cell is a device in which, electrical energy can be produced through a series of the electrochemical reactions using biochemical pathways. In an MFC, *exoelectrogenic*[2] bacteria break down the organic matter, usually under anaerobic conditions, and pass on the recovered electrons to an external electron acceptor (i.e., the anode). While electrons flow through an external circuit, protons (pumped out of the bacterial cells) travel through the electrolyte and a separator towards the cathode, where a final electron acceptor (e.g., oxygen in the air) receives these electrons and protons and is reduced (Figure 1-1). To guarantee

[1] A typical municipal wastewater going through a biological treatment process has been shown to contain ca. 14.7 MJ per kg of COD.

[2] Bacteria that are able to transfer electrons outside the cell membrane to an external electron acceptor.

electron transfer to the anode, one should make sure that there is no other electron acceptor with a higher redox potential available in the anode chamber [3].

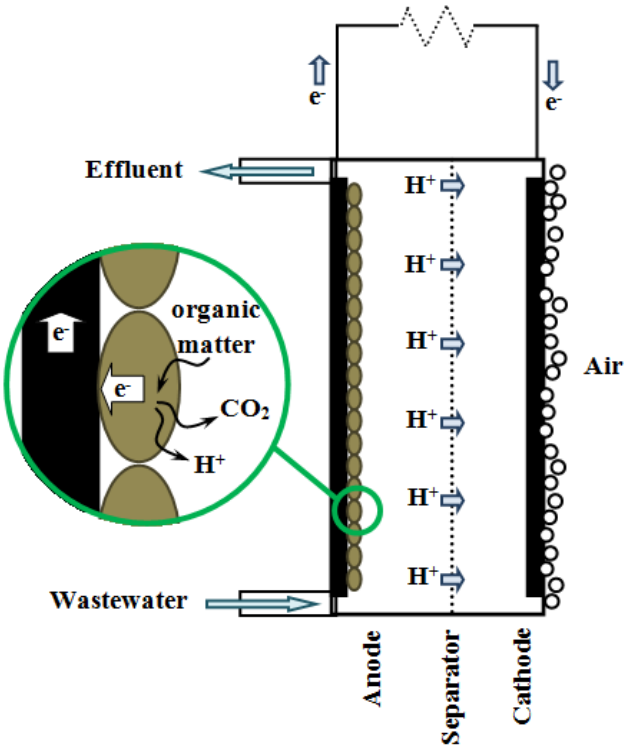

Figure 1-1 Schematic sketch of a passive air-breathing MFC

Incorporating the MFC technology into the current biological wastewater treatment systems not only can potentially yield organics recovery in the form of energy, but also can save energy through the elimination of the current aeration and solids handling units [3], yielding wastewater treatment at a lower expense. Microbial fuel cells could also be considered superior to their current alternate, anaerobic digestion (AD) that converts biomass to methane, in many aspects such as their ability to function on dilute wastewaters at ambient temperatures and direct conversion of the organics to the final product [4]. These two technologies, however, are

usually considered to be complimentary to each other rather than competitive, and could be used together to provide a more efficient treatment system [5].

In addition, the application of the bio-catalysis on bio-fuels at moderate operational conditions in MFCs can be considered an advantage over the chemical fuel cells which usually operate under extreme conditions utilizing reformed fossil fuels and expensive catalysts. Using the whole microorganisms for bio-catalysis in MFCs guarantees the complete breakdown of the organic matter which is considered an advantage over the enzymatic fuel cells (EFCs). Unlike EFCs that are usually specific to a certain substrate, MFCs can operate on diverse substrates due to the engagement of the whole microorganism in bio-catalysis and hence, are more suitable for complex substrate sources such as wastewater. Moreover, despite their relatively higher power output, EFCs suffer from a short lifetime in the order of days [6, 7], whereas MFCs have shown to produce stable power for years [8–10] due to their ability to naturally regenerate their enzymes [11].

In addition to the biological wastewater treatment systems [4, 12–16], a variety of systems can implement the MFC technology, to produce electrical energy and/or to remove unwanted compounds. Therefore, MFCs could be applied to remove nitrates and sulfates from the waste streams in the bio-remediation devices [17], power underwater generators using marine sediments in the bentic underwater generators (BUGs) [18], measure the biochemical oxygen demand (BOD) of water in biosensors [8, 19, 20], and power self-sufficient outdoor machines (gastrobots) [21–23]. The growing pressure on our environment and the call for renewable energy sources are further motivation for the development of the MFC technology targeting

large-scale applications, even though the power output is still reported to be lower than that of their alternative electrochemical systems (Figure 1-2).

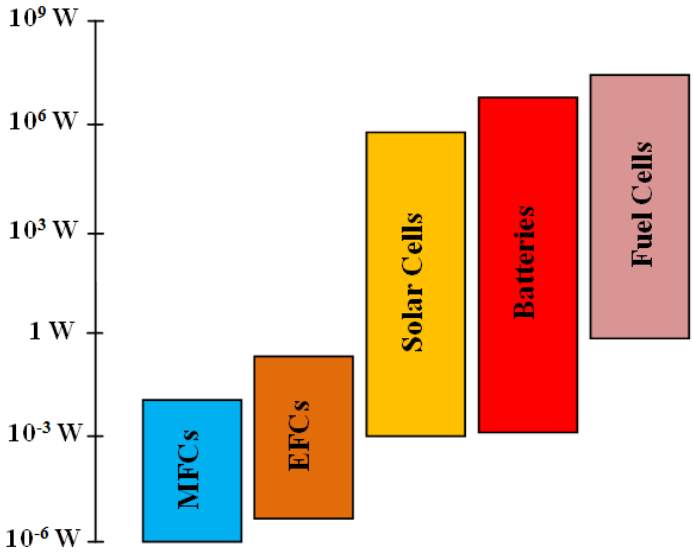

Figure 1-2 Power output in MFCs compared to their current alternatives [24]

1.2 Basic principles of the MFCs

Like chemical fuel cells, MFCs operate based on a series of oxidation reactions taking place at the anode and reduction reactions taking place at the cathode, if the overall reaction is thermodynamically favorable. A complete oxidation of organic matter at the anode produces electrons, protons, and carbon dioxide[3]:

$$\text{Organic matter} + H_2O \Longrightarrow ne^- + nH^+ + CO_2 \qquad \text{Eq.1- 1}$$

[3] Other gases such as methane may also be generated in the anode chamber, depending on the microbial culture.

The oxidant consumes the produced electrons and protons at the cathode and is reduced to a final product (e.g., water, ferrous iron, ferrocyanide) that usually needs to be removed:

$$\text{Oxidant} + \ ne^- + nH^+ \Longrightarrow \text{Final product} \qquad \text{Eq.1- 2}$$

Similar to chemical fuel cells, MFCs can work as a power source with an internal resistance. The cell voltage, thus, drops as soon as the current is drawn from the MFC due to the different overpotentials. Therefore, the voltage balance can be written as:

$$E_{cell} = \ E_c - E_a - jR_\Omega = E_{c_e} - E_{a_e} + \eta_c - \eta_a - jR_\Omega \qquad \text{Eq.1- 3}$$

where E_{cell} is the overall cell voltage (V), E_c is the cathode working potential (V vs. SHE), E_{c_e} is the equilibrium potential of the cathodic (reduction) reaction (V vs. SHE), E_a is the anode working potential (V vs. SHE), E_{a_e} is the equilibrium potential of the anodic (oxidation) reaction (V vs. SHE), η_c is the cathode overpotential (V), η_a is the anode overpotential (V), j is the local Faradic current density (A/m^2), and R_Ω is the Ohmic resistance of the cell ($\Omega.m^2$). The equilibrium potential for each of the anodic and cathodic reactions is related to their standard half-cell potentials and the operating conditions, and can be calculated using:

$$E_e = \ E_e^\circ - \frac{RT}{nF}\ln\left(\frac{C_O}{C_R}\right) \qquad \text{Eq.1- 4}$$

where E_e° is the standard half-cell potential of the reaction (V vs. SHE), R is the universal gas constant (J/K/mol), T is the operating temperature (K), n is the number of electrons, F is the Faraday constant (C/mol), C_O is the concentration of the oxidizing species (M), and C_R is the concentration of the reducing species (M).

The jR_Ω term refers to the **Ohmic overpotential** of the system, which are results of the energy lost to overcome the resistance towards transfer of ions within the electrolyte and transfer of electrons within the electrical connections. The Ohmic overpotential can be reduced by optimizing the MFC architecture such as placing the electrodes closer to each other (decreasing the electrode spacing) and increasing the ionic conductivity of the electrolyte. The overpotentials at the electrodes (η_a and η_c), on the other hand, are thought to result from the two main sources; the activation and the concentration. **The activation overpotential**, a.k.a. the kinetic overpotential, happens as some energy is lost to initiate the redox reactions. At low current densities, activation overpotential is dominant, and could be reduced through improving the catalysis (e.g., using mixed cultures at the anode) and the kinetics of the redox reactions (e.g., increasing the temperature). **The concentration overpotential**, a.k.a. the mass transfer overpotential, happens when the consumption rate of the redox compounds is higher than the transfer rate of the fresh redox compounds to and the transfer of the produced products away from the (bio)catalyst surface. Therefore, a lower mass transfer rate limits the reaction rate. The concentration overpotential is more evident at high current densities and can be reduced by improving the mass transfer of the reactants towards and products away from the electrodes (e.g., by stirring).

In addition to activation and concentration overpotentials, the anode compartment of the MFCs also suffers from another source of energy loss, known as the bacterial metabolic overpotential. **The bacterial metabolic overpotential** is the energy lost to the maintenance and the reproduction of the organisms and can potentially be reduced by engineering the microbial community [3]. In the anode, accumulation of the bacterial metabolism products

around the bio-catalyst can lead to an increased concentration overpotential by limiting the transfer of nutrients to the active sites of the bio-catalyst and the transfer of the produced protons from within the biofilm to the cathode [3].

The overall performance of an MFC is characterized by measuring the voltage difference between the anode and the cathode when the external circuit is disconnected (known as the open circuit voltage, OCV) and obtaining the polarization and power density curves. To obtain the polarization and power density curves, different voltages (E) within the range of the OCV and 0.1 V are applied to the electrodes using a Potentiostat and the produced electrical current (I) is measured. The power output can then be calculated by multiplying the applied voltage by the measured current:

$$P = EI \qquad \text{Eq.1- 5}$$

To be able to compare the performance data generated by different MFC configurations, the power and current are usually normalized based on either the surface area of the anode (or the separator) or the volume of the anode compartment (or the whole MFC). The power and current normalized based on the surface area are called the superficial (apparent) power and current densities. The power and current normalized based on the volume are called the volumetric power and current densities. The polarization and power density curves can then be developed by plotting the voltage and power density versus the current density.

In addition to the power density and polarization curves, the performance of an MFC can be evaluated by measuring the number of the electrons recovered as the electrical current

versus the total number of the electrons recovered during the degradation of the organic matter. This recovery is referred to as the Coulombic efficiency (CE) and is calculated as [3]:

$$CE = \frac{M_s I}{F n_{es} f \Delta C} \qquad \text{Eq.1- 6}$$

where M_s is the molecular weight of the substrate (kg/mol), I is the produced current (A), F is the Faraday constant (C/mol), n_{es} is the moles of electrons released per mole of the fuel, f is the wastewater flow-rate (m^3/s), and ΔC is the change in substrate concentration (kg/m^3).

1.3 Technological barriers of the MFCs

Although significant progress has been made in the MFC research, researchers are still facing many technological challenges such as the low electron recovery rate and high cost (e.g., Pt-based cathodes, polymeric membranes) [11, 25]. Currently, the capital cost of the MFCs constructed in a laboratory-scale is ca. $15/kg COD [26]. This requires a substantial reduction, before the MFCs can become economically viable.

Utilizing wastewater, with much lower ionic conductivity than the liquid or solid electrolytes used in the chemical fuel cells, limits the protons conduction from the anode towards the cathode and increases the Ohmic overpotential in the MFCs. This acidifies the anode chamber and alkalizes the cathode chamber, and causes a pH gradient within the MFC, a.k.a. the pH splitting [27]. Partial or full bio-catalyst deactivation [28, 29], salt precipitation on the cathode catalyst [30], and negative cathode potential shift [31] are drawbacks of the pH splitting, which can limit the power output, even in presence of a buffer solution [32].

Increasing the salinity of wastewater is the least preferred option as it increases the operating cost, on one hand, and can inhibit the bio-catalyst, on the other hand [33]. Practical ways of enhancing proton transfer from the anode towards the cathode are through improving the hydrodynamic of the system [34] and decreasing the travel distance of protons [13, 35–38]. A practical alternate to address the high Ohmic overpotential issue is to decrease the distance between the electrodes while constantly buffering the electrolyte. In fact, the distance between the electrodes is critical as the Ohmic overpotential within the municipal wastewater (with the ionic conductivity in the order of 0.1 S/m) utilized by a typical full-scale bio-electrochemical system could cause a voltage loss as high as 100 V/m of the distance between the electrodes (at a current density of 10 A/m^2, Figure 1-3) [26].

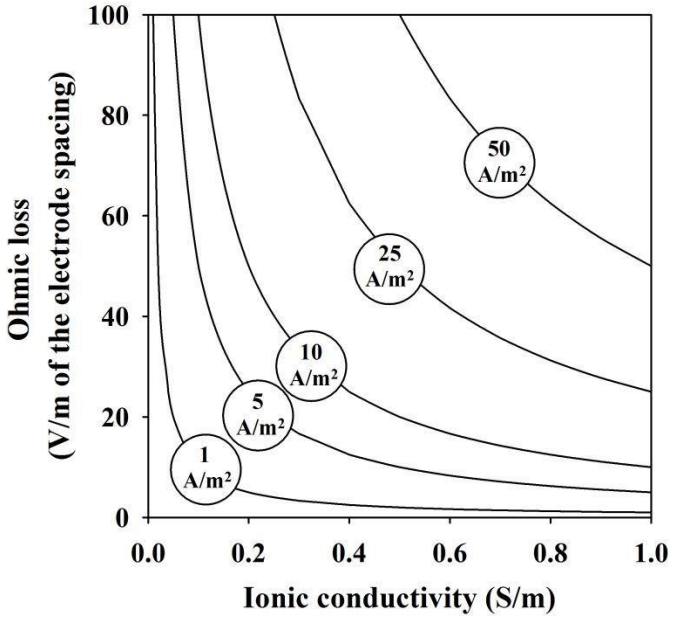

Figure 1-3 Ohmic overpotential within the electrolyte [26]

Aside from improving the MFC performance to target large-scale applications such as wastewater treatment, it is also critical to decrease the overall capital and operating costs of the MFCs. That is why the passive air-breathing design has become of interest. The application of a passive convection and diffusion in the fuel cell design and operation is well known for decreasing the parasitic load for running auxiliary pumps, fans, or compressors, and eliminating the utilization of expensive oxidants in direct methanol fuel cell (DMFCs) [39–42]. Application of a passive air-breathing cathode could therefore result in a decreased overall cost, complexity, and volume of the MFC setup [43]. However, the performance of passive air-breathing cathodes is usually limited by the uncontrolled operating conditions, limited mass transfer, and accumulation of the produced water [43].

The combination of the flat-plate MFC (FPMFC) design and the passive air-breathing cathodes seems appealing for the large-scale applications, however, no researchers have examined the power generation in this configuration. This is likely due to the relatively low power densities reported for the combination of the flat-plate design and an active air-breathing cathode, attributed to the excessive presence of oxygen at the anaerobic anode [13, 37]. Like DMFCs, oxygen crossover[4] to the anode is to be avoided in the FPMFCs, as it can cause anodic mixed potentials and anode depolarization, inhibit the bio-catalyst, and therefore reduce the efficiency. Fuel crossover to the cathode, on the other hand, can result in cathodic mixed potentials and cathode depolarization, and biofilm growth on the cathode. Therefore, a separator is necessary to decrease the oxygen and fuel crossover [27]. The application of a

[4] Crossover in fuel cells refers to the mass transfer of the reactants (fuel and/or oxidant) to the opposite chamber such as the fuel and the oxidant are mixed.

separator increases the internal resistance and the Ohmic overpotential as well as the cost of the bio-electrochemical system. In addition, a separator can also result in the anode acidification and cathode alkalization (pH splitting) as it adds to the resistivity of the system towards transferring protons. Furthermore, most separators are subject to (bio)fouling and degradation in the long-term [44–46]. Hence, in-depth investigation of the separator component, that is necessary to isolate the components of the anode and the cathode (i.e., electrodes, reactants, and electrolyte) in the passive air-breathing FPMFC configuration, is of great importance.

1.4 Thesis layout

Figure 1-4 presents the steps taken to meet the specific objectives of this research. A brief description for each chapter is presented as follow:

Chapter 2 is divided into three sections, presenting a review of the literature on i) the flat-plate configuration applied in the MFC studies, ii) a comparison of the FPMFC to other MFC configurations, and iii) different separators applied in the MFCs.

Chapter 3 presents the scope and objectives of the thesis.

Chapter 4 demonstrates the passive air-breathing FPMFC concept. In this chapter, a passive air-breathing FPMFC is engineered and operated with synthetic wastewater containing ethanol to identify the appropriate operating conditions. The preliminary results of the FPMFC engineering and operation are presented in terms of the wastewater treatment and power production efficiencies.

Chapter 5 studies the role of the 3D anode on the FPMFC performance. In this chapter, the surface of the anode is activated through acid treatment. The effect of the active surface area of the anode on the performance is also investigated for further application of this configuration in biological wastewater treatment. The electro-active thickness of the 3D anode is also estimated to investigate one of the major challenges of the 3D electrodes, i.e., the non-uniform voltage/current distribution.

Chapter 6 focuses on the separator component. In this chapter, 8 separators from the two categories of IEMs and diaphragms are selected and characterized in non-inoculated passive air-breathing and aqueous setups to investigate i) the crossover of oxygen and fuel, ii) the ionic resistivity, and iii) the proton transport number. These separators are further evaluated in three passive air-breathing FPMFCs with different electrode spacing to study the sensitivity of the FPMFC performance to the separator characteristics.

Chapter 7 presents a numerical model based on the mixed potential theory. The main goal in developing this model is to predict the peak power density of the passive air-breathing FPMFC using different separators. This is performed through estimation of the mixed potentials at the electrodes. In addition, the model is used to analyze the sensitivity of the peak power density to the characteristics of the separator.

Chapter 8 focuses on the economic considerations of the FPMFC construction using different separators. In this chapter, separators are ranked based on the energy produced by the FPMFC versus the capital cost of the FPMFC using those separators.

Chapter 9 includes the overall conclusions and outcomes, significance of the research, recommendations, and the future work.

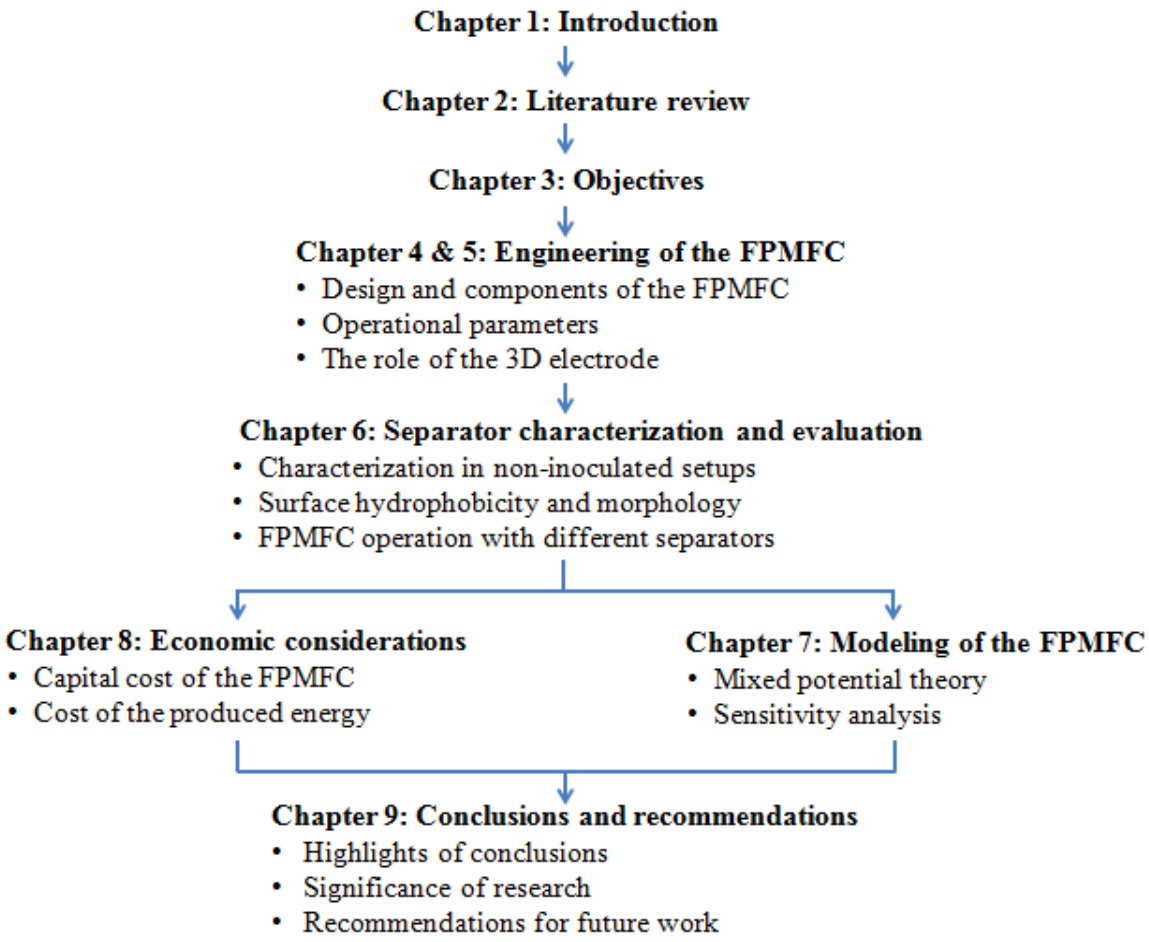

Figure 1-4 Thesis layout

Chapter 2: Literature review

2.1 Flat-plate (planar) MFC configurations

The performance of the flat-plate (planar) configuration in polymer electrolyte fuel cells [47–51] has been a motivation to investigate this configuration in the MFCs. The FPMFC configuration is a promising design for the large-scale applications such as wastewater treatment, as the closer spacing of the electrodes can reduce the Ohmic overpotential resulted from the low ionic conductivity of the wastewater. Improved peak power densities have been reported using the flat-plate configuration [13, 35], as a result of the reduced Ohmic overpotential, compared to that achieved in designs with electrodes placed further apart [12, 52]. Another potential advantage that has been ignored about this configuration is the potential for more efficient usage of space, which can improve the efficiency of wastewater treatment and the mass transfer. This is because the portion of the wastewater that can bypass the anode is smaller when no stirring is taking place.

While the passive air-breathing cathode concept is well known in the cubic or cylindrical MFCs (with large electrode spacing [53–55]), the FPMFC configuration has only been constructed in a two-chamber design either by machining flow fields within the chambers (Figure 2-1) [13, 36], or by simply bolting two hollow containers together [35, 37]. Implementing the flow fields into the flat-plate design is known to improve the mass transfer through a more controlled distribution of the fuel and oxidant [47–51]. However, it also limits the surface of the anode electrode for the bio-catalyst attachment in the MFCs. This can limit the performance of the MFCs, where the anode surface area plays a major role due to much

lower rate of the biological electron transfer. Studies implementing the flat-plate configuration in the MFCs have been conducted using different system parameters and are distinguished from one another via the differences in the electrode spacing, flow field, and the oxidants utilized. The electrode spacing in the FPMFC studies has varied from few micrometers (where the separator was sandwiched between the electrodes [13]) up to 0.024 m [36]. Despite the large electrode spacing of 0.024 m, the applied configuration was still referred to as a FPMFC, as it provided the opportunity to stack several MFCs using bipolar plates.

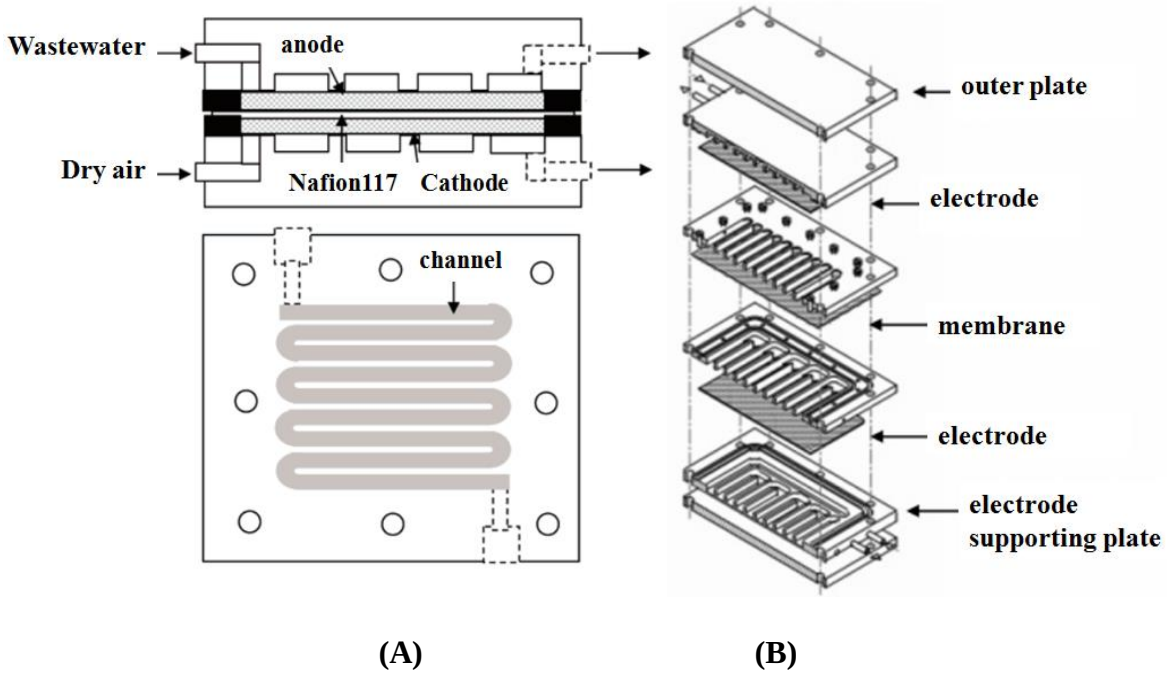

Figure 2-1 FPMFC configurations used by A) Min and Logan [13] and B) Heijne et al. [36]

Oxygen (air), ferric iron, and ferricyanide have been used as oxidants in the FPMFCs. Oxygen, the most popular oxidant in the MFC studies, has been utilized in the aqueous [37] and gaseous [13] forms, where it was actively being supplied to the cathode. Unlike air-breathing MFCs [12, 53], increasing the dry air flow-rate has been reported to decrease the

peak power density and the OCV in the FPMFC design with the separator sandwiched between the anode and the cathode [13]. This indicates that the crossover of oxygen can play a critical role on the generation of current in an FPMFC. Increasing the concentration of the soluble oxygen (through purging the catholyte with pure oxygen instead of air), on the other hand, has been reported to increase the peak power in a FPMFC with the electrodes placed 0.01 m apart [37]. The close spacing of the electrodes therefore can be detrimental to the current generation of the FPMFCs when using oxygen as the oxidant. Peak power densities of 0.22 W/m^2 [13] and 0.72 W/m^2 [37] (based on the geometric anode surface area) have been produced in a single FPMFC and a bipolar stack of 4 FPMFCs, utilizing gaseous and dissolved oxygen as the oxidant, respectively. The reported peak power densities are generally lower than those reported for the passive air-breathing MFCs with large electrode spacing (0.02 m and larger) [55–57].

High oxygen concentration at the anode of the FPMFCs is considered a major issue in current generation. Thus, a simple strategy to eliminate this is to replace oxygen with other oxidants. Ferric iron [36] and ferricyanide [35] have been used as replacement for oxygen at the cathode of the FPMFCs. Utilizing ferric iron seems to be advantageous to the current generation in the FPMFC design, as opposed to oxygen. Despite the applied large electrode spacing (0.024 m), high peak power density of 0.86 W/m^2 has been reported for an FPMFC using a ferric iron cathode and a bipolar membrane (Fumasep®FBM). The bipolar membrane (BPM) was shown to reduce the extent of the pH splitting, whereas using a cation-exchange membrane (CEM) was indicated to yield ferric iron hydroxide precipitation in the membrane as a result of the elevated cathode pH [36]. Application of the BPMs, however, is always

accompanied by a voltage drop across the membrane as a result of water dissociation happening at high current densities. The reduction of ferricyanide at the cathode, on the other hand, is less damaging to the separating media in the long-term compared to the ferric iron. Similar to the ferric iron, the ferricyanide cathodes have shown a better overall performance, as opposed to the oxygen cathodes [58–61]. Utilizing ferricyanide at the cathode of a plant FPMFC has produced a peak power density of 0.44 W/m^2 [35].

Overall, the utilization of the active air and oxygen flow, ferric iron, and ferricyanide at the cathode of the MFCs is an unsustainable approach in terms of the operating cost when it comes to the large-scale applications. The relatively low power output of the FPMFC configuration is likely not able to compensate the energy requirements of the auxiliary equipment required to actively supplement the oxidant to the cathode nor to cover the cost of the oxidant periodic regeneration. Ferrous iron, the product of the ferric iron reduction, can be regenerated back to ferric iron through oxidation by *ferrooxidans* [32], but the oxidation process requires the presence of oxygen [62]. The required continuous catholyte aeration can create additional issues in terms of the mixed potentials and the sustainability of the operation. Therefore, passive air-breathing cathodes seem to be one of the ultimate choices for the practical application of the FPMFCs. Table 2-1 lists the characteristics and performance data reported for the FPMFCs in the literature.

Table 2-1 The Flat-plate MFC characteristics and performance data available in the literature

Configuration	Electrode spacing (m)	Fuel	Oxidant	Separator	Internal resistance[5]		Power density[6]		OCV (V)	Ref.
					($\Omega.m^2$)	($\Omega.m^3$)	(W/m^2)	(W/m^3)		
Two-chamber FPMFC	NS[7]	Glucose	Air	Nafion®117	0.2	0.001	0.22	55	0.4	[13]
Two-chamber FPMFC	0.024	Acetate	Ferric iron	Fumasep®	0.2	0.004	0.86	42	0.7	[32, 36]
A stack of 4 two-chamber FPMFCs	0.01	Acetate	Oxygen	Ralex®	1.0	0.005	0.72	144	4.1	[37]
Two-chamber FPMFC	NA[8]	Plant roots	Ferricyanide	Fumatec®	7.3	0.554	0.44	5.8	0.6	[35, 63]

[5] Based on the anode geometric surface area and chamber volume

[6] Based on the anode geometric surface area and chamber volume

[7] No space, the separator was sandwiched between the electrodes

[8] No available

2.2 Non-planar MFC configurations

The passive air-breathing (a.k.a. the single-chamber) design is generally considered more economically viable for large-scale applications as the operating and capital costs are both reduced compared to the configurations constructed in a two-chamber style (using oxidants other than passive air). The single-chamber MFC has mainly been constructed in non-planar styles such as cubic [44, 64, 65], cylindrical [55, 56, 66, 67], or tubular [68–70] forms. In these configurations, the electrodes were either placed on each side of one chamber with few centimeters of distance or placed both on one side (with the separator sandwiched between the anode and the cathode).

Despite their advantages, lower power densities have been reported for the single-chamber MFCs compared to the two-chamber MFCs. The highest peak power densities reported for the single-chamber MFC design has varied from 1.8 W/m^2 [55] to 2.8 W/m^2 [56] depending on the cell configuration, bacterial culture, and electrolyte strength. The highest power densities, on the other hand, have been reported in two-chamber configurations (3.0 W/m^2 [61], 4.3 W/m^2 [59], and 7.2 W/m^2 [60]), likely due to the improved cathode performance with ferricyanide as the oxidant.

The main goal in development of the non-planar single-chamber configuration, despite their relatively high ohmic resistance, has been the cost reduction not only by eliminating the cathode chamber and an expensive oxidant, but also by removing the separator. The separator-free configuration, however, faces issues such as biofilm growth on the cathode. In addition, due to the large space commonly applied for the anode chamber, the single-chamber MFCs require special operating conditions (e.g., advective flow [34]) or continuous mixing, to

achieve efficient wastewater treatment. Table 2-2 presents a summary of the configurations and performance data available (based on the anode cross-sectional surface are) in the literature.

Table 2-2 – Summary of the configurations and performance data of the MFC research

Configuration		Substrate	Oxidant	Separator	Power density (W/m^2)	Ref.
Single-chamber	Flat-plate	Acetate	Active air-flow	Nafion117	0.29	[13]
		Glucose			0.21	
		Wastewater			0.07	
	Cylindrical	Ethanol	Passive air-flow	Separator-free	0.49	[66]
		Wastewater	Passive air-flow	Separator-free	0.26	[67]
		Acetate	Passive air-flow	J-cloth	2.77	[56]
		Acetate	Passive air-flow	J-cloth	1.80	[55]
	Cubic	Acetate	Passive air-flow	Nafion117	0.51	[25]
				Ultrex AMI	0.61	
				Ultrex CMI	0.48	
		Wastewater	Passive air-flow	Microfiltration	0.22	[71]
				Separator-free	0.2	
		Acetate	Passive air-flow	Separator-free	0.90	[44]
				Glass fiber	0.79	
				J-cloth	0.79	
		Acetate	Passive air-flow	Ultrex AMI	0.72	[64]
		Acetate	Air/ferricyanide	Hyflon	0.04	[65]
	Tubular	Glucose	Passive air-flow	Ultrafiltration	0.40	[70]
		Acetate	Passive air-flow	Ultrex CMI	0.05	[69]
				Ultrex AMI	0.04	
		Acetate	Air/ferricyanide	Ultrex CMI	0.03	[68]
Two-chamber	Flat-plate	Acetate	Ferric iron	Fumasep-FBM	0.86	[36]
		Acetate	Active air-flow	RALEX CEM	0.72	[37]
		Plant roots	Ferricyanide	Fumatec-CEM	0.44	[35]
	Cubical	Glucose	Ferricyanide	Ultrex CMI	4.31	[59]
		Glucose	Ferricyanide	Nafion117	7.20	[60]
		Glucose	Active air-flow	Nafion117	0.16	[72]
		Acetate			0.06	
	Miniature	Acetate	Air/ferricyanide	Polycarbonate	0.1	[73]
				Nylon	0.08	
				Nafion117	0.06	
		Lactate	Ferricyanide	Nafion117	3.00	[61]

2.3 Separators applied in the MFCs

It has been widely recognized that the efficient and sustainable operation of the MFCs is dependent on the presence of a separator [28]. The role of the separator becomes more significant when it comes to designs with small electrode spacing (e.g., the flat-plate design), as the absence of a separator can cause numerous issues to the sustainable operation of the MFC. Recent work on the MFCs shows that researchers have begun to address the separator role in power generation of the MFCs. A major step has been taken by Rozendal et al. [74], who reported that the competitive transfer of cations (e.g., Na^+, K^+, $NH4^+$, Ca^{2+}, Mg^{2+})[9] versus the protons can limit the performance of the MFCs using CEMs. Application of the CEMs, that are not selective to protons, can result in pH splitting, which may inhibit the bio-catalyst [28, 29], form salts on the cathode, and hinder the reduction reaction [30, 31].

The unique properties of the CEMs, a.k.a. the proton exchange membranes (PEM), widely used in chemical fuel cells, seem to get depressed in the mild MFC environment (neutral pH, low ionic conductivity, and abundant presence of cations) [73]. In this regard, researchers have tried to address the issues related to the separator by exploring a variety of separators adopted form the chemical fuel cells. A wide variety of separators have been used in the MFCs, with differences in their structure, material, pore size, thickness etc. The applied separators are mainly distinguished based on the mechanism of transferring species and therefore are categorized into two major groups, the ion-exchange membranes (IEMs) and the diaphragms.

[9] Available in the MFC environment in concentrations $\times 10^5$ higher than protons

Table 2-3 lists the separators tested in the MFCs along with their independently investigated characteristics. The investigated characteristics consist mainly of the diffusion coefficients of oxygen and acetate (D_O and D_A) and the ionic resistivity (R) in the separator. The reported ionic resistivity values have been measured in a phosphate buffer solution (PBS, ca. 0.1 M), commonly used as the electrolyte in the MFCs.

Table 2-3 Summary of the evaluated separators and their characteristics in the MFC studies

Separator		Thickness ($\times 10^{-6}$ m)	D_O ($\times 10^{-10}$ m^2/s)	D_A ($\times 10^{-13}$ m^2/s)	R ($\times 10^{-4}$ $\Omega.m^2$)	Cost (USD/m^2)	Ref.
Ion-exchange membranes	Nafion®117	178	2.4	0.82	9.2	500	[25, 73, 75]
	Hyflon®	300	-	-	-	-	[76]
	Ultrex®CMI	460	4.3	0.66	45.1	80-200	[25, 68, 75]
	Ultrex®AMI	460	4.3	2.7	-	80	[25, 77]
	Fumatec®	-	-	-	-	-	[35]
	RALEX®	450	-	-	-	-	[37]
	Fumasep®FAD	80-100	-	-	12.4	-	[75, 78]
	Fumasep®FBM	180	-	-	-	-	[36, 75]
	PES/SPEEK 5%	150	19.4	-	584.2	-	[79]
	PES/SPEEK 3%	110	2.3	-	1140.5	-	[79]
Diaphragms	Zirfon®	500	95	-	136	60	[78]
	Glass fiber	1000	5	-	-	0.32	[31, 44, 80]
	Glass wool	-	-	-	-	-	[14, 81]
	J-cloth	300	87	-	-	-	[44, 55]
	Canvas cloth	600	-	-	-	3.5	[82]
	MF	-	-	-	-	-	[71]
	UF-0.5K	265	0.5	0.24	-	350	[25]
	UF-1K	265	1.1	4.2	-	350	[25]
	UF-3K	265	1.1	7.2	-	350	[25]
	UF-B0125	-	-	-	-	-	[83]
	Nylon mesh	200	-	-	-	-	[31, 73]
	Reg. cellulose	200	-	-	-	-	[73]
	Cellulose nitrate	125	-	-	-	-	[73]
	Polycarbonate	20	-	-	-	<200	[73]

2.3.1 Ion-exchange membranes

Ion-exchange membranes (IEMs) are usually made of a hydrophobic polymeric backbone to which hydrophilic positively or negatively charged functional groups are connected. Two major mechanisms of "hopping" and "diffusion" are usually used by IEMs to transfer ions [51, 84, 85]. Those IEMs with negatively charged functional groups (e.g., sulfonate) are called cation-exchange membranes (CEM), a.k.a. the PEMs, and mainly transfer cations. Those IEMs with positively charged functional groups (e.g., quaternary ammonium) are called anion-exchange membranes (AEM), and mainly transfer anions. A combination of a CEM and an AEM, on the other hand, is known as a bipolar membrane (BPM) and can be used to transfer both cations and anions.

A wide variety of the CEMs have been used in the MFC studies. The most commonly used CEM is Nafion®117 (DuPont, USA) [60, 86–89], as a result of its excellent proton conductivity in hydrogen fuel cells (HFC). The high cost of Nafion® membrane, however, limits its application in the MFCs as they yield a much lower power output than the HFCs. That is why several other inexpensive CEMs have been tested in the MFCs. Ultrex®CMI7000 (Membranes International Inc., USA) is one of the most frequently tested CEMs that is well-known for its high ionic resistivity and low permeability to oxygen [25, 44, 68, 75, 90]. Hylon® (Solvay-Solexis, Italy) [76], Ralex®CEM (Mega a.s., Czech Republic) [37], and Fumatec® (Fumatec, Germany) [35] are other CEMs that have been tested in the MFCs and have indicated relatively similar ionic conductivity to Nafion®117. Improved ionic conductivities have been reported for the poly ether sulfone (PES) membranes customized by a low percentage of sulfonate poly ether ether ketone (SPEEK), compared to the Nafion® membranes [79], indicating that the

separator characteristics can be customized to match the requirements for the more efficient operation of the MFCs.

Despite the differences in the materials and structure, CEMS suffer from several common issues. Poor proton conductivity is one of the main disadvantages of the CEMs [44], which is attributed to the low ionic conductivity and neutral pH of the electrolyte. Also, due to competitive transport of all cations, the MFCs applying CEMs usually suffer from pH splitting. That is why the AEMs have become of interest. Ultrex®AMI7001 (Membranes International Inc., USA) [25, 69, 77, 83, 91], Fumasep®FAD (Fumatech GmbH, Germany) [75, 78], and DF-120 (Tianwei Membranes, China) [92] are the AEMs that have been used in the MFCs, to address the issues raised by the CEMs. A more balanced cathodic pH in the presence of a buffer solution due to the transfer of the phosphate or carbonate is an advantage coupled with the application of AEMs over the CEMs [25]. Higher peak power densities have been reported using the AEMs, most likely due to the smaller extent of the pH splitting [25, 77, 83]. The higher fuel permeability, however, is considered as a disadvantage of using the AEMs compared to the CEMs [25]. Also, since the AEMs are known to perform in presence of a buffer solution, their large-scale application for wastewater treatment may not be practical as it will require a periodic dosage of a buffering compound.

Due to the migration of either anions or cations, both AEMs and CEMs are subject to deformation. While the CEMs usually bend towards the cathode, the AEMs usually bend away from the cathode, creating a gap between the separator and the cathode [77]. This can create issues, especially when the IEM is pressed against an air-breathing cathode, where no catholyte is used. Since the IEMs are usually not permeable to the electrolyte, formation of a gaseous

void between the membrane and the cathode can result in an increased Ohmic overpotential. Hence, the membrane deformation needs to be addressed before the IEMs can be used efficiently. Hot-pressing the membrane to the cathode to form a membrane-electrode assembly (MEA) [38, 53, 93, 94], application of structural supports [77] and hydro-gels [69], and also application of the membrane as the substrate of the air-breathing cathode [95] are useful strategies that can be used to tackle this problem. Despite all the negative effects coupled with the application of both CEMs and AEMs, they are known to be less permeable to the neutral species (e.g., oxygen and fuel) compared to diaphragms, thus are still considered effective alternatives.

To take advantage of the characteristics of both AEMs and CEMs, BPMs can be used. Fumasep®FBM (Fumatech GmbH, Germany) is a BPM that has been tested in MFCs [36, 75] and has been shown to prevent pH splitting at low current densities (<3 A/m^2). At higher current densities (>10 A/m^2), like CEMs, the BPM has been reported to imbalance the pH [75]. The application of the BPMs is not recommended in general, especially at high current densities, due to their high polarization potential [36, 96] and the potential inability to prevent pH splitting [75]. Overall, the BPMs seem to be more suitable for the MFCs using aqueous cathodes, where the cathode is exposed to the catholyte, as opposed to the air-breathing MFCs where the cathode is exposed to a solid electrolyte membrane.

2.3.2 Diaphragms

In opposed to the IEMs that mainly transfer ions, there are diaphragms that are porous separators. Diaphragms are not ion-selective and allow both ions and neutral species with diameters smaller than their pores to go through while holding back larger species. As a result,

diaphragms show higher protons and neutral species permeability than the IEMs. Based on the differences in their pore diameter, diaphragms could either be categorized as the micro-porous (e.g., micro-filtration and ultra-filtration diaphragms with pore diameters in the order from 10^{-8} m to 10^{-5} m [97]) or the coarse-pore (e.g., fabrics, fibers, and meshes with pore diameters larger than 10^{-5} m) diaphragms. The main goal of replacing the IEMs with diaphragms in the MFCs is to address the poor proton conductivity and the pH splitting issues while reducing the cost imposed by the polymeric membranes.

Various micro-porous diaphragms have been applied in the MFCs [25, 70, 71]. Due to their relatively small pore size, some micro-porous diaphragms can retain the anodic and cathodic electrolytes in their chambers, while this is not possible using most micro-porous and all coarse-pore diaphragms. Therefore, high oxygen and fuel crossover is one of the main issues related to the application of diaphragms in the MFCs. Ultrafiltration membranes (UFM) [25, 70], Nylon and polycarbonate diaphragms [31, 73], glass fiber filters [31, 44, 80], glass wool [14, 81], and Zirfon® (Agfa, Belgium) [78] are the diaphragms that have been tested in the MFCs and have shown comparable peak power densities to the CEMs in the configurations with electrode spacing of 0.02 m and larger.

Despite their advantages, several barriers limit the application of the micro-porous diaphragms. Among those is the high crossover of fuel and oxidant which results in mixed potentials at the electrodes. Micro-porous diaphragms have been mainly used in the MFCs with the electrodes placed apart (0.02 m and larger) and have indicated a significant effect on the cathode potential. In fact, it has been shown that the cathode potential could decrease when the separator pore size is decreased, shifting from a separator-free to a CEM setup (with an

electrode spacing of 0.02 m) [31, 44]. The decreased cathode potential is likely due to elevated cathode pH as a result of the pH splitting. Anode potential, on the other hand, has been shown to remain unchanged using diaphragms with different pore sizes, indicating no significant variation in the anodic mixed potentials and anode depolarization in those configurations. This is also consistent with other studies using diaphragms in the MFCs with large electrode spacing [44, 53].

In the coarse-pore diaphragms, the pore size can vary from 10^{-5} m in the Nylon mesh filters [28] up to hundreds of microns in the J-cloth and canvas [44, 55]. The larger pore size of the coarse-pore diaphragms usually leads to a higher flux of the fuel and oxidant as well as the protons compared to the micro-porous diaphragms and IEMs. This usually lowers the efficiency especially when a biofilm is not fully developed on the separator matrix to consume the crossing oxygen and fuel [44]. The biofilm growth on the diaphragm can also lower the performance by limiting the protons transfer, hence, there is a compromise in transferring the protons and other species when using coarse-pore diaphragms. Furthermore, the much lower cost of the diaphragms increases their feasibility for the large-scale applications such as wastewater treatment. However, the durability of both micro-porous and coarse-pore diaphragms in the MFC environment in the long-term is an issue that needs to be addressed in the first place.

2.4 Knowledge gaps

Separators applied so far in the MFCs have been selected based on their popularity and the available performance data. The reported MFCs performance, however, are affected by many factors other than the separator characteristics such as the configuration of the MFC. In fact,

the interplay between the MFC configuration and the separator characteristics plays a key role on the MFC performance. While the presence of a separator can be necessary for the efficient operation of one MFC configuration (e.g., flat-plate), addition of a separator to another MFC configuration (e.g., a passive air-breathing MFC with much larger electrode spacing) can lower the power output. There are no reports available on the correlation between the characteristics of the separator and one of the most important FPMFC design characteristics, the electrode spacing, on the MFC performance.

To select appropriate separators for the application in the passive air-breathing FPMFCs, having more information on the important characteristics of the separator can be of great assistance. Characterization of the separators in the MFC studies has mainly been done in inoculated MFCs, where the performance of the MFC (i.e., power output, CE) was considered as an indication of the separator performance. Very few studies have focused on the characterization of separators independently in non-inoculated setups, all applying two-chamber aqueous-cathode configuration. The final destination of the characterized separators, however, was an air-breathing MFC.

While the ionic conductivity, the proton transport number, and the permeability of the separator to the fuel and oxidant can be considered the most important characteristics affecting the MFC performance, the extent to which each of these parameters alters the performance is unknown. Configuration of the MFC has a major effect on the role that each of those characteristics plays on the MFC performance. Therefore, prior to selection of appropriate separators, it is of great importance to identify the separator characteristics that play the most significant roles on the performance of a specific MFC configuration.

The separator is one of the most important components of operation in the passive air-breathing FPMFCs. Hence, understanding the interactions amongst the positive and negative effects imposed by the separator is important. Performing a systematic study on the characteristics of the separator as well as the role they play on the performance of the other FPMFC components, can provide useful insight into the design of proper separators, specifically for the application in the FPMFCs.

Chapter 3: Objectives

The focus of this work was to design and engineer a passive air-breathing flat-plate (planar) MFC, investigate the role of the 3D anode electrode and the separator characteristics on the performance of this configuration, and model the flat-plate MFC configuration numerically based on the mixed potential theory. The specific objectives of this research were to:

1. Demonstrate the passive air-breathing FPMFC concept and engineer it through:

    - The design and development of a passive air-breathing FPMFC
    - Investigation of the effect of the operational modes
    - Investigation of the effect of the 3D electrode surface activation
    - Investigation of the effect of the active surface area of the 3D electrode
    - Investigation of the electro-active thickness of the 3D electrode

    Chapters 4 and 5 focused on targeting this objective.

2. Evaluate 8 separators in non-inoculated passive air-breathing and aqueous setups through investigation of:

    - The mass transfer and diffusion coefficients of oxygen, ethanol, and acetate
    - The proton transport number
    - The ionic resistivity
    - The surface hydrophobicity
    - The surface morphology

Chapters 6 focused on targeting this objective.

3. Examine the selected separators in three FPMFCs with different electrode spacing through investigation of:

    - The polarization and power density curves
    - The wastewater treatment efficiency
    - The Coulombic efficiency
    - The energy production cost

    Chapters 6 and 8 focused on targeting this objective.

4. Develop a numerical model based on the mixed potential theory to:

    - Estimate the kinetic parameters of the bio-electrochemical system
    - Estimate the electrode potentials using different separators
    - Analyze the sensitivity of the power output to the separator characteristics
    - Analyze the sensitivity of the power output to the electrode spacing

    Chapters 7 focused on targeting this objective.

The main focus of this research was on the electrochemical study of the MFC system, therefore the biological aspects of the electrochemical system were not investigated.

Chapter 4: Passive air-breathing FPMFC concept demonstration and operation

4.1 Introduction

One of the main challenges in the operation of the MFCs is the low ionic conductivity of the wastewater which can result in a high Ohmic overpotential [26]. Since increasing the ionic conductivity of the wastewater is not a viable solution, the electrode spacing can be decreased. This has been demonstrated in some passive air-breathing MFC designs (Figure 4-1, far left). The anode chamber space in an MFC, however, can be utilized more efficiently through reducing its depth. Improved mass transfer as well as enhanced wastewater treatment efficiency in the continuous operation with parallel (and not advective [34]) flow of the wastewater are the advantages that can potentially be offered by the FPMFCs implementing 3D anodes.

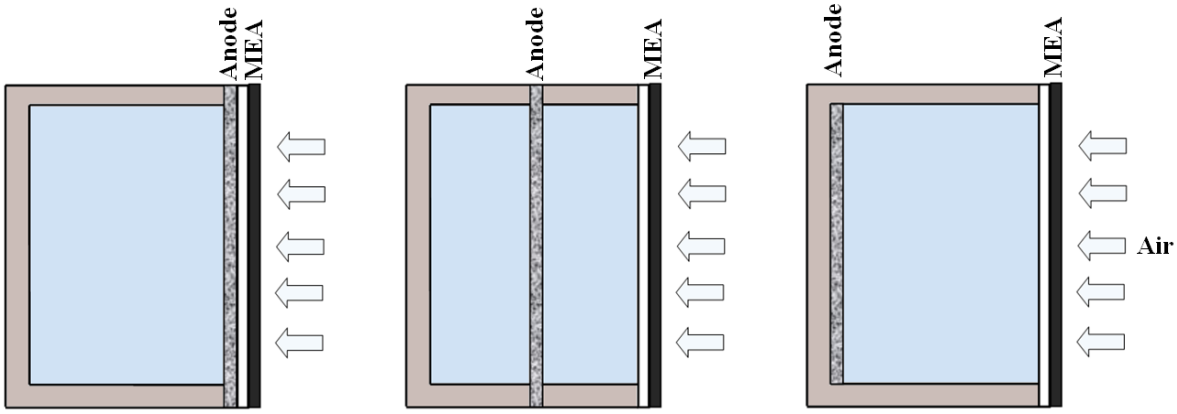

Figure 4-1 Schematic of the passive air-breathing MFC configurations used in the literature

In this chapter, the passive air-breathing FPMFC concept was demonstrated and engineered. A study was conducted to investigate the suitable operational conditions for the sustainable operation of the passive air-breathing FPMFC. This was performed through the FPMFC performance characterization by studying the polarization and power density curves and the wastewater treatment efficiency during the operation in batch and continuous modes, and in presence and absence of a proton exchange membrane (PEM).

4.2 Experimental

4.2.1 FPMFC design and components

The passive air-breathing FPMFC consisted of a graphite plate with a pocket used as the anode chamber (dimensions: 0.05 m × 0.10 m × 2×10^{-3} m) and a graphite frame used as the membrane-electrode assembly (MEA) holder. The MEA holder was used to sandwich the PEM and the air-breathing cathode against the pocket (Figure 4-2). Using biocompatible electronically conductive graphite plates to fabricate the compartments of the FPMFC guaranteed the electrical connection between each electrode and its designated compartment, and served as a current collector. This eliminated the complexity of inserting an external current collector. Two groves were constructed alongside the inlet and the outlet to provide uniform electrolyte distribution within the anode compartment. Neoprene gaskets (0.5×10^{-3} m in thickness) were installed to provide insulation between the electro-conductive components of the FPMFCs.

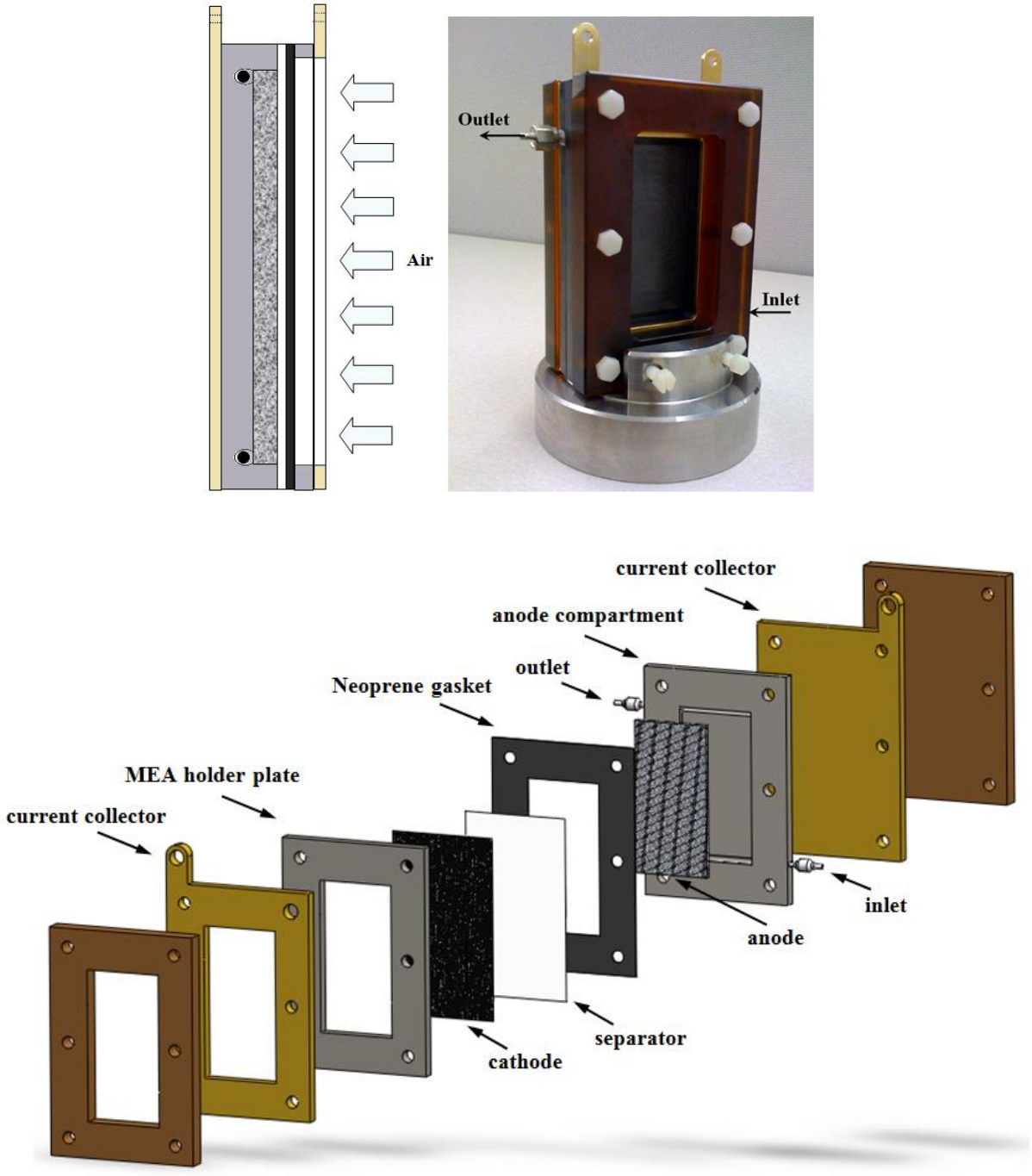

Figure 4-2 Passive air-breathing FPMFC configuration used in this work

A three-dimensional (3D) graphite felt anode (0.05 m × 0.095 m, 3×10^{-3} m thick, GF-S6-03, Electrolytica, USA) was fitted in the pocket of the graphite plate to form the anode

chamber. Nafion®117 membrane (DuPont, USA) was used as the PEM. The air-breathing cathode consisted of a carbon cloth substrate (0.05 m × 0.10 m; 50 wt.% wet-proofing, E-TEK, USA) coated on one side with a layer of a platinum catalyst on a carbon support (Pt loading of 0.01 kg/m^2 (1 mg/cm^2)) facing the membrane and on the other side, with four layers of a polytetrafluoroethylene (PTFE) suspension [98]. A high loading of Pt was adopted to assure that the cathode was not limiting the performance. The preparation of the air-breathing cathodes and Nafion®117 were done according to the procedures reported in Appendix A.

To prepare the MEA, the Pt-coated side of the cathode and the PEM were hot-pressed together, using a pressure and a temperature of 80 bar and 413 K for 4 minutes. The MEA was then sandwiched between the graphite frame and the anode chamber with the membrane facing the anode and PTFE-coated side facing the air. In the PEM-free tests, 2 layers of J-cloth was used as the separator between the graphite felt anode and the carbon cloth cathode.

4.2.2 Operation and performance characterization

Activated sludge from a pulp mill effluent treatment plant (Howe Sound Pulp and Paper, British Columbia, Canada) was used as the source of the microbial culture. The sludge was enriched with ethanol (0.085 M) to promote the growth of the "ethanol-consuming" communities prior to being introduced to the anode. To acclimate and obtain sufficient biofilm on the anode, the graphite felt anode was placed in the culture/sludge fed with ethanol, minerals, and vitamins in a shaking incubator (SI-600, Rose Scientific Ltd, Canada) at 303 K, 4 weeks prior to being transferred to the FPMFC.

A nutrient medium containing mineral and vitamin solutions in a phosphate buffer solution (PBS) was prepared as the synthetic wastewater (pH~7), as described in Appendix A. Ethanol was added as the fuel (0.085 M). It was then fed to the FPMFC using a peristaltic pump. The conditions of the synthetic wastewater, i.e., the pH, dissolved oxygen (DO), and temperature were controlled/monitored in the feed tank equipped with a pH probe (BIOFLO 110 fermentor/bioreactor, New Brunswick Scientific Co., Inc., USA), a DO probe (InPro® 6800, New Brunswick Scientific Co., Inc., USA), and a thermometer, respectively. These allowed maintenance of the feed solution at a controlled pH (ca. 7) during the continuous operation, and constant DO (ca. 0%) and temperature (ca. 303 K) during both batch and continuous operations.

During the batch operation, 2×10^{-3} m^3 of the synthetic wastewater was circulated through the FPMFC at 1.7×10^{-8} m^3/s (1 mL/min). The pH and chemical oxygen demand (COD) of the feed tank were monitored daily. The synthetic wastewater batch in the feed tank was replaced with a fresh batch each time the COD decreased to less than half of its initial value. During the continuous operation, the synthetic wastewater was passed through the FPMFC in a single pass at 1.7×10^{-9} m^3/s (0.1 mL/min) and the outlet stream was analyzed daily, as the treated wastewater, by monitoring its pH and COD (Figure 4-3).

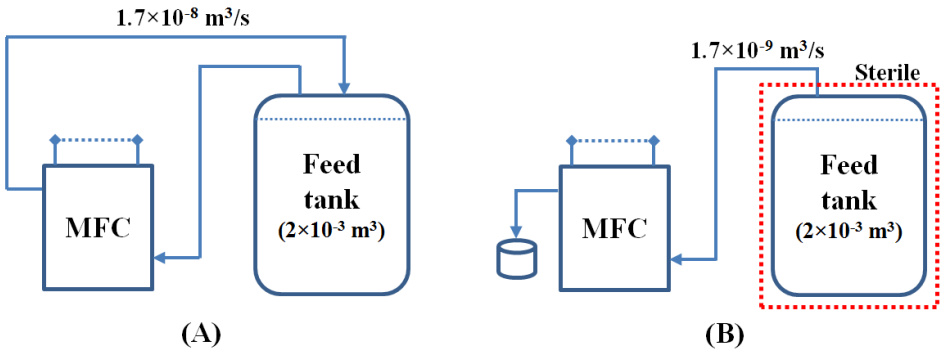

Figure 4-3 FPMFC setup in A) Batch, B) Continuous modes

The FPMFC operated by connecting the anode and cathode electrodes through an external load (500 Ω) until stable voltage was achieved. Then, the circuit was disconnected to monitor the OCV and obtain the polarization and the power density curves. Development of the polarization and power density curves, measurement of the internal resistance, and COD removal efficiency were performed according to the procedure reported in the Appendix A.

4.3 Results and discussion

4.3.1 The effect of the operating mode

The FPMFC was initially operated in batch mode with a previously acclimated graphite felt anode. The circuit was initially connected using an external load of 500 Ω. During each batch, the voltage increased within 3-4 days and then stabilized for 4-5 days (followed by a gradual decrease afterward, due to depletion of the organic content of the feed tank). The circuit was disconnected after the initial stabilization of the voltage (8 days after starting the operation at each batch), to measure the OCV and obtain the polarization and power density curves.

The OCV stabilized after ca. 12 hours of disconnecting the circuit. The polarization curves for each batch were obtained after the initial stabilization of OCV (9 days after starting each batch). The peak power density increased every time the synthetic wastewater was replaced with a fresh batch. The OCV for the batch operation was 0.72±0.01 V. The peak power density achieved with the FPMFC in the 3rd batch was 0.04 W/m^2 at 0.13 A/m^2. The Ohmic resistance of the FPMFC was measured to be $40\times10^{-4}\pm4\times10^{-4}$ Ω.m^2 ($8.4\times10^{-6}\pm0.8\times10^{-6}$ Ω.m^3). A rapid pH decrease from 7.8 to 6.8 was observed during the first 100 hours of the MFC operation. This was most likely due to the formation of acetic acid during ethanol degradation, also consistent with the observation reported by Tatton et al. [99]. They reported that the available *methanogens* within the mixed culture could degrade ethanol to methane, with acetic acid and hydrogen produced as intermediates of the degradation process [99]. After 120 hours of the operation, pH started to gradually increase and reached 7.4 in 800 hours. The gradual increase of pH was likely due to the adaption of the microbial culture to the produced acetate and the resulted microbial oxidation of acetate. In fact, Kim et al. [66] has reported that the metabolic pathway of the microbial communities available in an MFC utilizing ethanol has also the metabolic capability of acetate oxidation with the anode reduction. Monitoring the COD of the feed tank showed that it took 34 days to remove 55% of the COD of the feed tank (Figure 4-4).

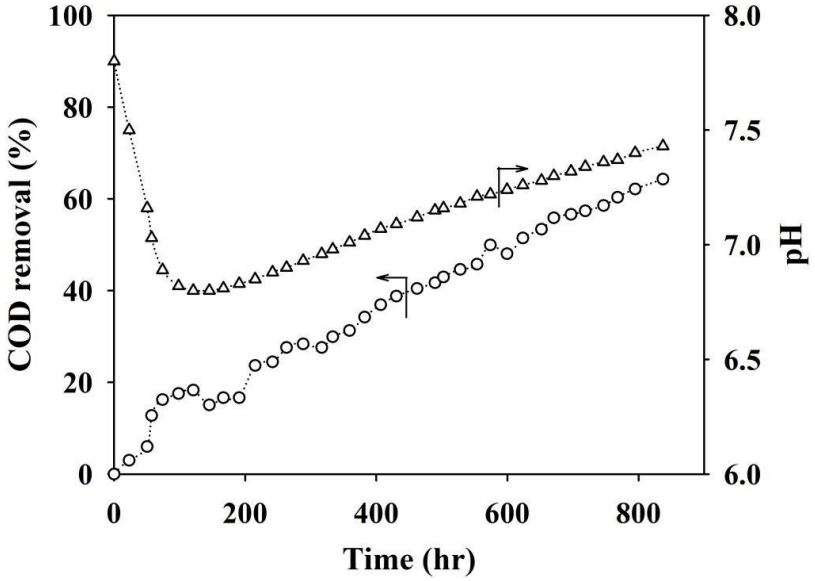

Figure 4-4 pH and COD of the feed tank monitored daily during the operation with the 3rd batch of the synthetic wastewater

Using the same MEA, the peak power density increased after each batch, likely as a result of further microbial growth. The highest peak power density and OCV were recorded in the 3rd batch, and dropped after that (Figure 4-5). (Bio)fouling of the membrane and the resulted decreased ionic conductivity [86] could be responsible for the power density drop. Also, reduction in the cathode active area due to the potential salt precipitation (caused by the elevated cathode pH [30]) may have negatively affected the power density as well as the OCV. To examine whether this was due to deactivation of the cathode catalyst and/or decrease in the ionic conductivity of the membrane, the MEA was replaced with a fresh MEA. It was expected that the power density would recover to the same level as the 3rd batch after replacing the MEA. The peak power density, however, did not improve after replacing the MEA which suggested that the MEA (bio)fouling was not the main issue hindering the performance.

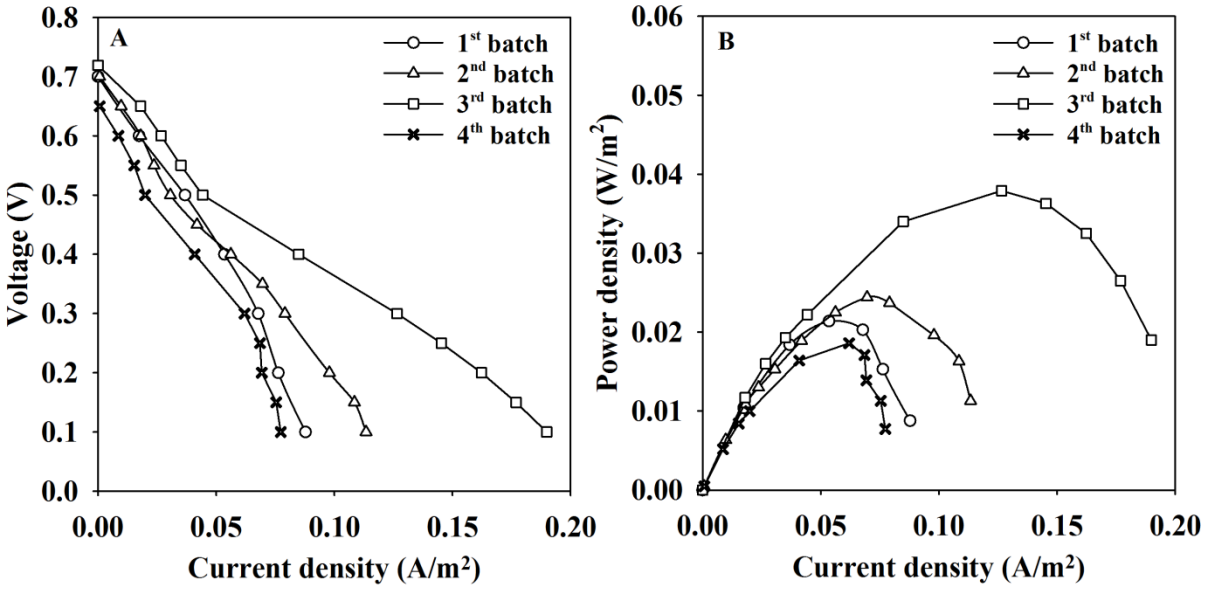

Figure 4-5 A) Polarization curves, B) Power density curves of the FPMFC, developed after replacing each batch of the used synthetic wastewater with a fresh batch

Biomass accumulation and clogging within the 3D anode during the FPMFC operation could also be responsible for the peak power drop by creating a barrier for substrate diffusion into and/or protons diffusion out of the biofilm [100]. In fact, a perceptible coverage of the anode with biomass was observed upon dismantling the FPMFC.

To eliminate the possible performance drop due to the batch operation, the FPMFC was allowed to operate in continuous mode. During the continuous operation, the pH of the outlet dropped from the inlet value of 7.0 to ca. 5.7 in the outlet after 24 hours of the operation, due to acetic acid generation. Consistent with the observation made during the batch process, the pH then increased gradually, and reached the value of 6.8 after 120 hours of operation after which it remained stable. At the retention time of 100 minutes in the FPMFC, the COD removal

efficiency reached 55% of the organics in the inlet stream in 9 days (Figure 4-6, compared to 34 days in the batch operation).

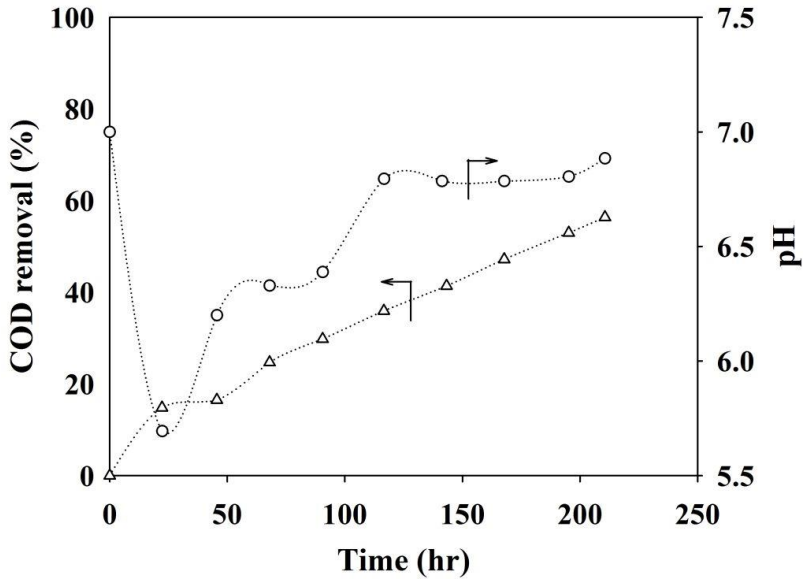

Figure 4-6 Outlet pH and COD removal monitored daily during the continuous operation

The OCV during the continuous operation was higher than that in the batch operation (0.77±0.01 V compared to 0.72±0.01 V, respectively). The relatively higher OCV during the continuous operation was likely a consequence of maintaining constant COD at the anode, while in the batch operation, the COD changed over time and diminished to ca. 80% of its initial value. The peak power density in the continuous operation was 2.5-fold higher than that in the batch operation (0.09 W/m^2 at 0.31 A/m^2 compared to 0.04W/m^2 at 0.13 A/m^2, respectively). The volumetric peak power density was 44 W/m^3 at 146 A/m^3 and 18 W/m^3 at 60 A/m^3 in the continuous and batch operation, respectively (Figure 4-7).

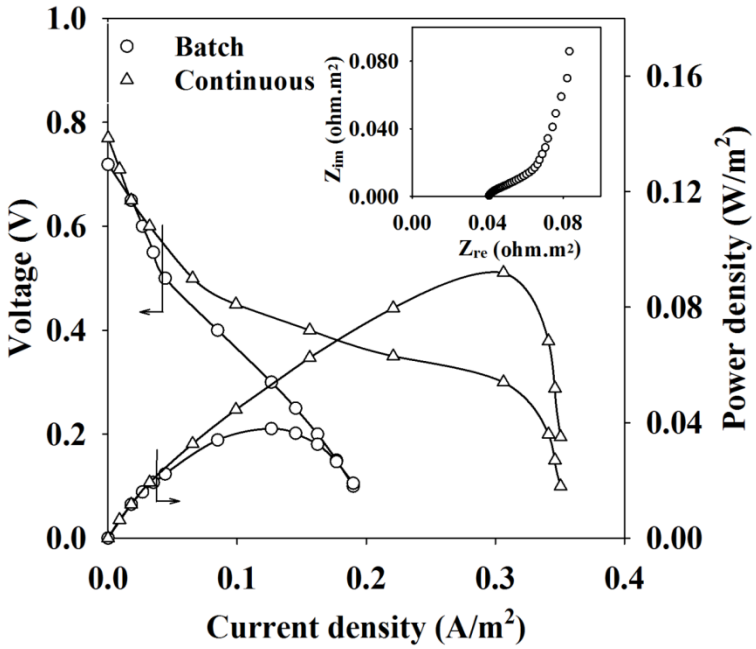

Figure 4-7 Power density and polarization curves of the FPMFC operating in batch and continuous modes (Inset: Nyquist plot of the FPMFC operating in continuous mode)

The continuous operation of the FPMFC provided a controlled feed with reduced effect of the inhibitory factors such as an accelerated biomass accumulation inside the FPMFC. The biomass accumulation was perceptible inside the anode chamber at the end of the batch operation, which likely created a resistance towards substrate diffusion to the active sites of the graphite felt anode as well as the protons diffusion out of it, whereas no noticeable biomass accumulation was observed inside the anode chamber at the end of the continuous operation. Mass transfer, however, seemed to be an issue during the continuous operation of the FPMFC as a result of the lower flow-rate used (Figure 4-7, high current density region).

4.3.2 The effect of the proton exchange membrane

To investigate the effect of the absence of a PEM, the FPMFC was also operated in batch mode with the MEA replaced with two layers of J-cloth and a carbon cloth cathode. The operation of the FPMFC using J-cloth (PEM-free) resulted in a lower OCV of 0.62±0.01 V compared to that achieved using an MEA (0.72±0.01 V). The stabilization of the OCV with J-cloth was achieved in 8 hours compared to the 12 hours achieved with the PEM. The peak power density was 0.04 W/m^2 (0.13 A/m^2) with the system using the MEA, more than 5-fold higher than that with a PEM-free configuration (7×10^{-3} W/m^2 at 0.02 A/m^2, Figure 4-8).

The higher OCV and peak power density achieved with the FPMFC using the MEA was because the PEM was less susceptible to oxygen and ethanol diffusion, as opposed to J-cloth (Diffusion coefficients of oxygen through Nafion®117 and J-cloth are 5.4×10^{-10} $m^2.s^{-1}$ [101] and 87×10^{-10} $m^2.s^{-1}$ [55], respectively). Oxygen diffusing through the air cathode into the anode chamber could negatively affect the performance by creating mixed potentials and inhibit the anaerobic communities. Further, the PEM could prevent mixed potentials at the cathode, happening due to the crossover of ethanol. This was contrary to the results reported by Liu et al. [53] who reported that removing the MEA (hot-pressed Nafion®117 to the carbon cloth cathode) increased the power density (from 0.3 W/m^2 to 0.5 W/m^2) in a passive air-breathing MFC. The MFC configuration used by Liu et al. had a larger electrode spacing (0.04 m) which is known to alleviate the effect of oxygen crossover in the passive air-breathing MFCs. Even though eliminating the PEM reduced the Ohmic overpotential of the FPMFC (diffusion coefficient of proton in J-cloth is ca. 91×10^{-10} $m^2.s^{-1}$ [55], which is likely higher than

Nafion®117), the negative effect of the oxygen crossover on the performance became more significant.

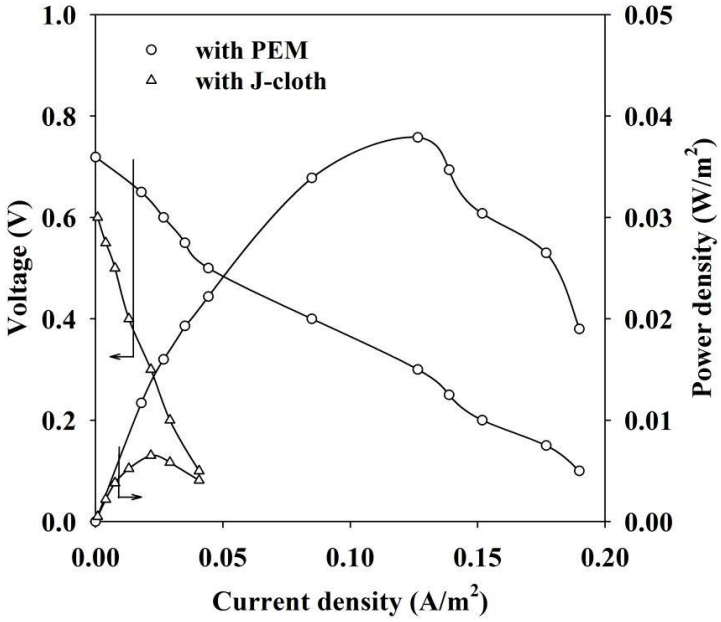

Figure 4-8 Power density and polarization curves of the FPMFC with and without a PEM

4.3.3 Comparison to FPMFCs in the literature

The FPMFC developed here produced 0.09 W/m^2 at 0.31 A/m^2 (44 W/m^3 at 146 A/m^3), operating at continuous mode. This was lower than those reported by Helder et al. [35], Heijne et al [36], Min and Logan [13], and Dekker et al [37] using two-chamber FPMFC configurations utilizing ferrcyanide, ferric iron, and active air, and oxygen flow cathodes, respectively (Table 2-1). Utilizing ferricyanide and ferric iron at the cathode has been generally indicated to yield higher peak power densities, compared to the oxygen (air) cathodes. This is due to the slower kinetics of oxygen reduction even on Pt. Also, using ferricyanide and ferric iron cathodes eliminates the issue of the oxygen crossover and possible bacterial inhibition.

However, it increases the operating cost as well, as those oxidants need to be regenerated. Active air and oxygen flow cathodes are also known to perform better than the passive air-breathing cathodes, mainly due to the improved mass transfer.

The high OCV value measured here (ca. 0.77 V) indicated that the mixed potentials could be less significant when using a passive air-breathing cathode, as opposed to an active air flow cathode [13]. The internal resistance of the FPMFC developed here was $40\times10^{-4}\pm4\times10^{-4}$ $\Omega.m^2$ ($8.4\times10^{-6}\pm0.8\times10^{-6}$ $\Omega.m^3$). This lower internal resistance compared to those reported for this configuration was mainly due to the MEA design (PEM hot-pressed to the carbon cloth cathode) as well as the small electrode spacing applied. The lower internal resistance measured in the FPMFC, however, did not result in a higher peak power density compared to the other FPMFCs, indicating that it was likely suffering from poor performance of one of its main components (i.e., anode and/or cathode).

The main hindrance for obtaining comparable power production here was the insufficient current generation. Application of the passive air-breathing cathodes has always been accompanied by a limited cathodic mass transfer. Engineering the cathode structure (e.g., through modification of the diffusion layer [102]) could be used to improve the three-phase interface for oxygen reduction over Pt [103] and therefore improve the mass transfer [98].

The current generation could also be limited by the poor performance of the bio-catalyst. The bio-catalyst *exoelectrogenic* activities could be improved by enhancing the bio-catalyst-electrode attachment through applying anodic surface modification techniques [104, 105].

4.4 Conclusions

The passive air-breathing FPMFC using a graphite felt anode and an MEA (Nafion®117 hot-pressed to the air-cathode) was shown to produce a peak power density of ca. 0.09 W/m^2, from synthetic wastewater containing ethanol during the continuous operation. The PEM-free FPMFC produced a much lower peak power density compared to the FPMFC using the MEA, due to the excessive crossover of oxygen and ethanol. The peak power density obtained with the FPMFC operating continuously was 0.09 W/m^2 at 0.31 A/m^2, higher than that achieved during the operation in batch mode (0.04 W/m^2 at 0.13 A/m^2), indicating that the continuous operation favors the bio-catalyst maintenance.

Chapter 5: Three-dimensional anode in the passive air-breathing FPMFC

5.1 Introduction

The FPMFC engineering and operation, in chapter 4, indicated that the operation in continuous mode and the presence of a polymeric membrane were in favor of the sustainable power generation by the FPMFC. Oxygen crossover seems to be an issue that both passive and active air-breathing FPMFCs are facing. It causes anodic mixed potentials and likely inhibits the anaerobic bio-catalyst. The oxygen crossover problem may not be fully addressed due to the permeability of most separators to oxygen, but improving the performance of other MFC components may alleviate this effect. Increasing the specific surface area of the anode has been generally shown to increase the peak power density [106–108] as the anode is usually a limiting factor in power production in the MFCs [105]. It is likely that an increase in the active surface area of the anode in the flat-plate configuration may also increase the power output, while still benefitting from the low Ohmic overpotential of this design.

Increasing the cross-sectional (geometric) surface area of the anode requires an increased size of the cathode and the separator, which may not be economically viable (due to application of expensive catalyst and membrane) for large-scale wastewater treatment systems. A 3D anode substrate, like graphite felt (GF), can offer a much greater actual surface area compared to a two-dimensional (2D, i.e., flat) substrate, per unit geometric surface area. Hence, the actual surface area of the anode can be increased through application of 3D GF substrates [61, 109–113]. The actual surface area of the anode can be further increased through increasing the thickness of the 3D anode. This could potentially increase the peak power density to a certain

limit, with no additional burden to increase the size of the separator, the cathode, and the cell in general. In addition, it may also result in a more efficient utilization of the anodic space compared to a 2D electrode, where wastewater can bypass the electrode matrix. A more complex voltage balance and non-uniform current generation, however, are common issues related to the application of 3D electrodes [114].

In this chapter, the passive air-breathing FPMFC engineering continued through conducting a study investigating the role of the 3D anode on power generation and wastewater treatment efficiency. The effect of the GF anode substrate surface treatment and surface area, and anode chamber depth on the performance was therefore investigated. Three FPMFCs with similar geometric surface area but different anode pocket depth (2 mm, 4mm, and 8 mm) were operated using 3D GF anodes and passive air-breathing carbon cloth cathodes. The GF substrate was treated by soaking in a boiling solution of HNO_3 prior to inoculation. The effect of the GF surface area was studied through application of 1, 2, and 3 packed layers of GF in the 2 mm, 4 mm, and 8 mm FPMFCs, respectively. The effect of the electrode spacing was investigated using only 1 layer of GF in the 2 mm, 4 mm, and 8 mm FPMFCs. The performance was characterized through examining the peak power density, Ohmic resistance, COD removal and Coulombic efficiencies, and electro-active thickness of the 3D anodes.

5.2 Experimental

5.2.1 FPMFC design and components

The passive air-breathing FPMFCs were constructed as previously reported in Chapter 4. The previously used MEA holder graphite frame was replaced with a perforated graphite plate

to provide structural support to the cathode and prevent deformation (Figure 5-1). The FPMFCs consisted of a graphite anode compartment with a pocket (geometrical dimensions: 0.05 m × 0.10 m) and a graphite perforated plate (to sandwich the PEM and the air-breathing cathode against the anode pocket). Three FPMFCs were constructed with identical geometrical surface area but different depths of the anode pocket (210^{-3} m, 410^{-3} m, and 810^{-3} m). Neoprene gaskets (0.5×10^{-3} m in thickness) were installed to provide insulation between the electro-conductive components of the FPMFCs.

Graphite felt was used as the 3D anode substrate (0.05 m × 0.095 m, 3×10^{-3} m thick, GF-S6-03, Electrolytica, USA). The surface of the GF substrate was treated by soaking in pure acetone, and then in a 1 M boiling solution of HNO_3 for 1 hour. The treated GF was then stored in DI water prior to use. Expanded stainless steel sheets (4SS(316L)10-125A, Dexmet, USA) were used to support the electronic connection between the anode electrode and the hosting compartment in all FPMFCs. This resulted in a 3D anode compression from 3×10^{-3} m to 2×10^{-3} m, in thickness. The first set of experiments was performed using 1, 2, and 3 packed layers of GF (2 mm, 4 mm, and 6 mm in thickness) placed inside the anode chamber in the 2 mm, 4 mm, and 8 mm FPMFCs, respectively. The second set of experiments was performed using only 1 packed layer of GF in the FPMFCs.

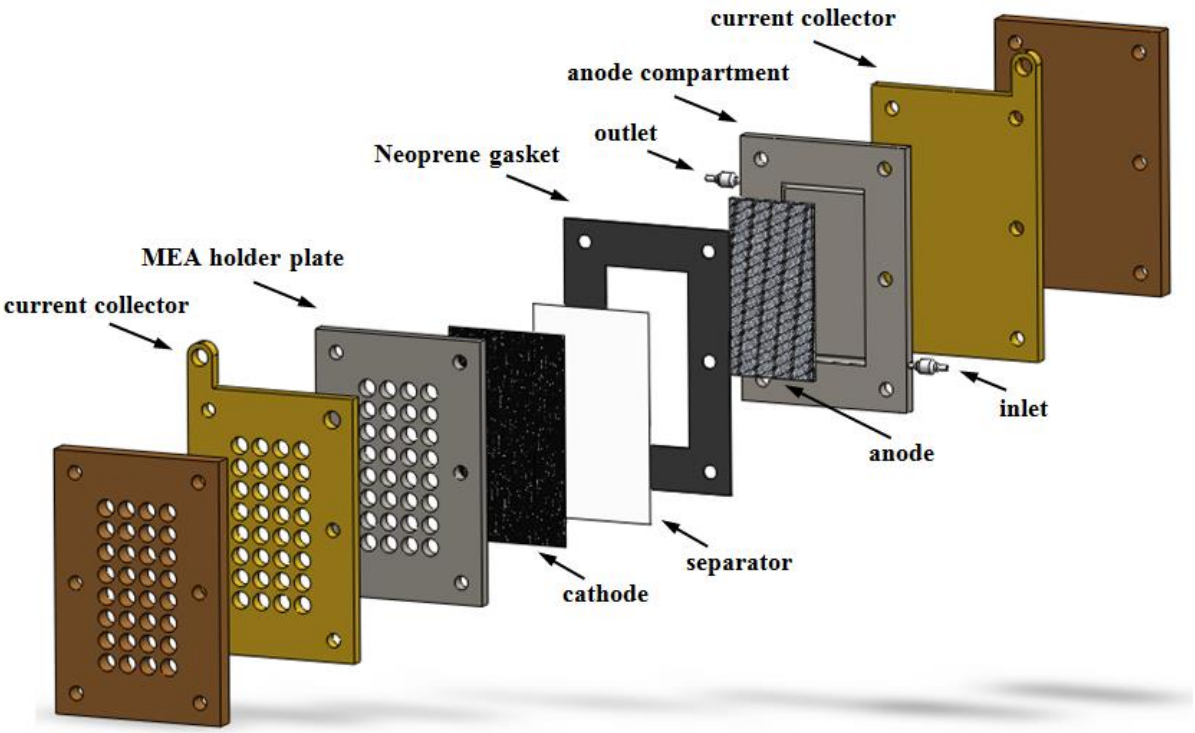

Figure 5-1 Passive air-breathing FPMFC configuration used in this work

The air-breathing cathode consisted of a carbon cloth substrate (projected surface area: 0.05 m × 0.10 m; 50 wt.% wet-proofing, E-TEK, USA) coated on one side with Pt catalyst (Pt loading of 0.01 kg/m^2) facing the membrane and on the other side, with three layers of a 60 wt.% PTFE suspension [98]. A high loading of Pt was adopted to assure that the cathode was not limiting the performance. Nafion®117 (DuPont, USA) was used as the PEM. The preparation of the air-breathing cathode and the treatment of Nafion®117 were done according to the procedures reported in Appendix A. Nafion®117 and carbon cloth cathode were sandwiched between the anode chamber and MEA holder plates, with the catalyst side of the cathode facing the PEM and PTFE side facing the air. The projected surface area of the PEM and the air-breathing cathode always remained constant during the tests at 5×10^{-3} m^2.

5.2.2 Operation and performance characterization

Primary treated wastewater (the University of British Columbia wastewater treatment pilot plant, BC, Canada) was used for the inoculation. The effluent was enriched with ethanol (0.085 M), minerals, and vitamins, and its conditions, i.e., DO and temperature were controlled in the feed tank equipped with a DO probe (InPro® 6800, New Brunswick Scientific Co., Inc., USA) and a thermometer, respectively. The temperature of the feed tank was controlled at 303±1 K and the feed container was maintained oxygen-free by continuous N_2 sparging. The nutrient-enriched wastewater was pumped continuously through the FPMFCs at 1.7×10^{-9} m^3/s (0.1 mL/min) for 2 months using a peristaltic pump. During the inoculation period, the FPMFCs were operated with the electrodes connected through a 500 Ω external load (Figure 5-2).

The FPMFCs were then continued to operate (with the electrodes connected through a 500 Ω external load) with simulated synthetic wastewater (prepared as described in Appendix A), containing ethanol and the necessary minerals, vitamins, and pH buffer with controlled temperature (303±1 K) and zero oxygen content for 2 months. A *methanogens* inhibitor (2-bromoethanesulfonate at concentration of 3×10^{-4} M [115]) was added to both actual and synthetic wastewaters to prevent *methanogenesis* from ethanol [99].

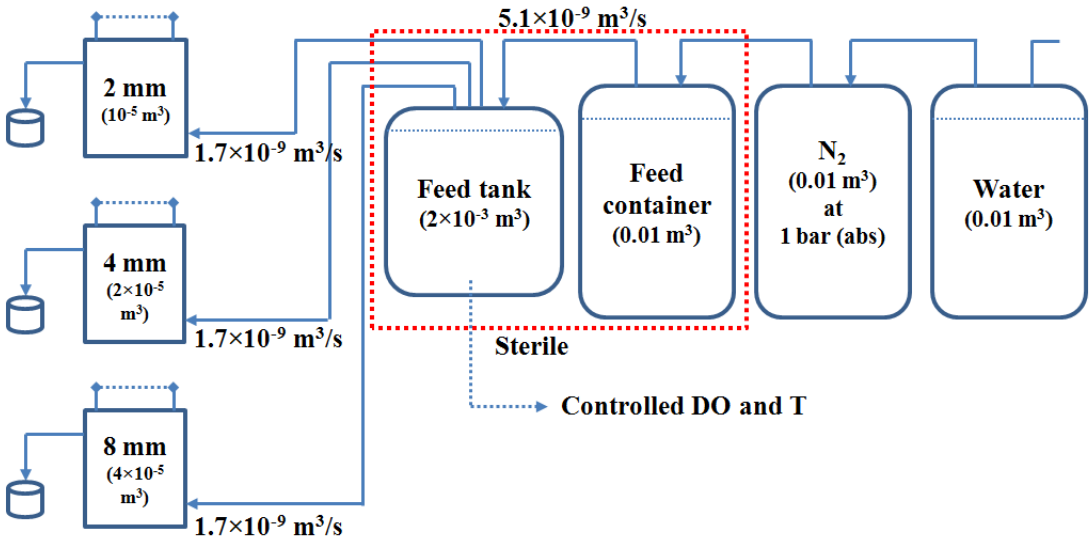

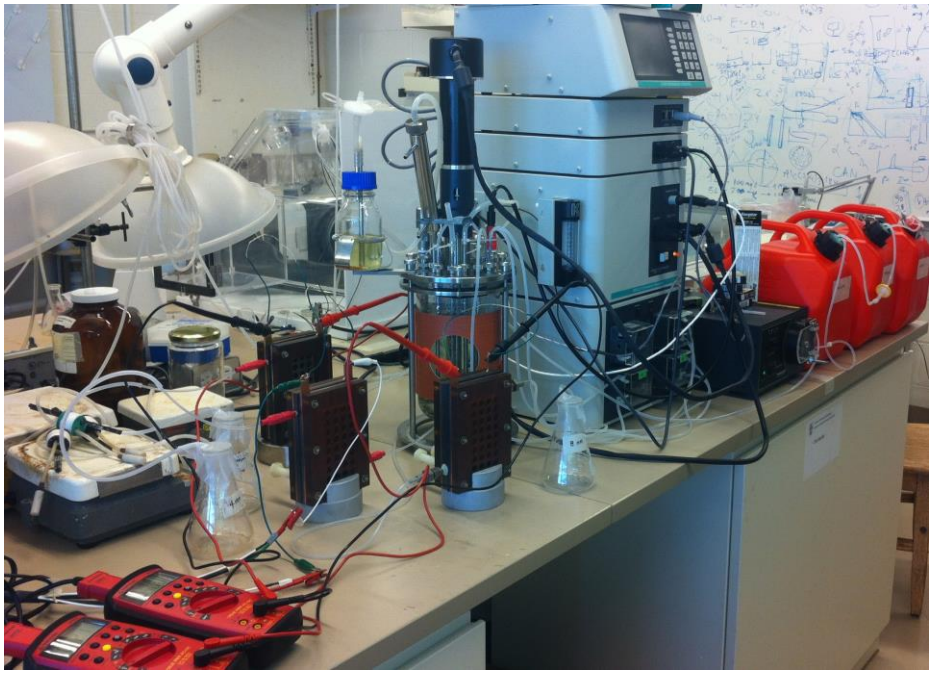

Figure 5-2 FPMFC setup, schematic and photograph

To examine the performance, a treated membrane and a fresh cathode were used prior to each test. The performance of the FPMFCs was then characterized by investigating the superficial and volumetric power densities and polarization curves, Ohmic resistance, CE, and

the COD removal efficiency. The FPMFC operated by connecting the anode and cathode electrodes through an external load (500 Ω) until stable voltage was achieved. Then, the circuit was disconnected to monitor the OCV and obtain the polarization and the power density curves. Development of the polarization and power density curves, measurement of the internal resistance, and COD removal efficiency were performed according to the procedure reported in the Appendix A.

5.2.3 Error calculations

The uncertainty of the current and voltage measurements done by the potentiostat was <0.2%. Hence, to calculate the actual error values associated with the polarization curves, all experiments were triplicated. For this purpose, the anode remained the same for all experiments while the membrane, the cathode, and the feed solution were replaced with a treated membrane, a new cathode, and a fresh feed solution, respectively, for each replication test. The standard deviation between the measurements of the replication tests was calculated according to:

$$\sigma = \sqrt{\frac{\sum_{i=1}^{N}(x_i - \bar{x})^2}{N}} \qquad \text{Eq.5- 1}$$

where x_i is the data value in measurement number i, $\bar{x}$ is the mean (or average) of a set of data values (sum of all of the data values divided by the number of data values), and N is the number of data points in the sample population (or number of the experiments, which in this chapter is equal to three). All reported error bars on the graphs and values within the text for the reported data are strictly meant for illustration as they represent the standard deviation for the results obtained over three runs.

5.3 Current distribution model

In designs with small electrode spacing (i.e., flat-plate, Figure 5-3) the passage of current through the electrolyte may not cause significant non-uniformity of potential (or current) distribution. However, the low ionic conductivity of the electrolyte along the inter-electrode gap can result in non-uniformity of potential and current. Hence, each component of the voltage balance may be time and position dependent. The non-uniformity due to the voltage drop through the electrode and electrolyte in the 3D electrodes should be given proper consideration. Potential distribution in a 3D electrode is given by [114]:

$$\frac{d^2E}{dx^2} = -aj\left(\frac{1}{\kappa} + \frac{1}{\sigma}\right) \qquad \text{Eq.5- 2}$$

where E is the operating electrode potential (V vs. SHE), x is the distance through the electrode (m), a is the specific surface area of the electrode (m^2/m^3), j is the local Faradic current density (A/m^2), κ and σ are the effective conductivities (S/m) of the solution phase and the electrode matrix, respectively. This differential equation can be solved to approximate the electro-active thickness of the 3D electrode. For many practical cases, solving the above equation can be very complicated and may be obtained by either a numerical method or analytically with proper boundary conditions.

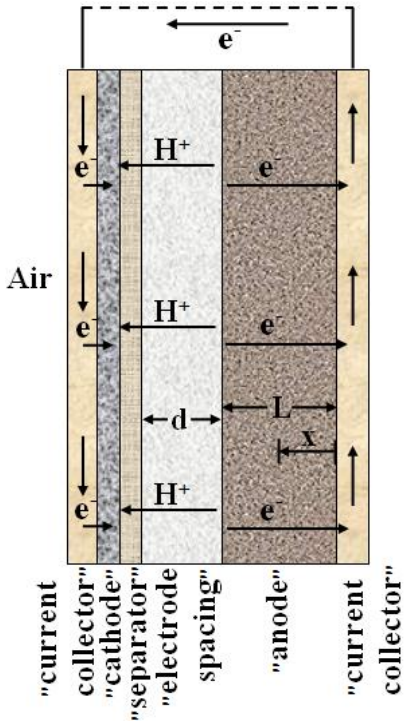

Figure 5-3 Schematic of the passive air-breathing FPMFC using 3D anode

A simple model for the current distribution and hence, the approximation of the electro-active thickness of the 3D electrode can be developed assuming that the Ohm's law applies to both electrode and electrolyte, and the current flows in the direction perpendicular to the feeder plate (x) [107]. The current density thus can be described as:

$$j = j_S + j_E = \left(-\kappa \frac{dE^0}{dx}\right) + \left(-\sigma \frac{dE}{dx}\right) \quad \text{Eq.5- 3}$$

$$\frac{dj_S}{dx} + \frac{dj_E}{dx} = 0 \quad \text{Eq.5- 4}$$

where j_S and j_E are the current densities (A/m^2) in the solution phase and the electrode matrix, respectively, and E^0 is the potential in the solution phase (V vs. SHE), with $x = 0$ at the feeder plate (current collector) and $x = L$ at the furthest spot of the electrode from the feeder plate (L

is the electrode actual thickness (m), Figure 5-3). The reaction rate varies depending on the specific kinetics of the oxidation reaction:

$$-\frac{dj_E}{dx} = \frac{dj_S}{dx} = a \times f[(E - E^0), C_F] \quad \text{Eq.5- 5}$$

where C_F is the concentration of the fuel (M). Assuming zero order reaction kinetic, constant fuel concentration, and low overpotentials within the electrode matrix [107], the rate of current change with the distance from the feeder plate can be written as:

$$-\frac{dj_E}{dx} = \frac{dj_S}{dx} = b \times (E - E^0) \quad \text{Eq.5- 6}$$

where b is a constant which can be estimated from the Erdey-Gruz-Volmer-Butler equation:

$$j = j^0[\exp(\frac{\alpha nF}{RT}(E - E^0)) + \exp(\frac{(1-\alpha)nF}{RT}(E - E^0))] \quad \text{Eq.5- 7}$$

where j^0 is the exchange current density (A/m^2), α is the electron transfer coefficient, n is the number of the electrons exchanged, R is the gas constant (J/mol/K), T is the temperature (K), and F is the Faraday constant (C/mol). Assuming low overpotentials for the FPMFC, a linear form of the Erdey-Gruz-Volmer-Butler equation can be assumed between the current density and the electrode potential and the constant b can be estimated as:

$$b = a \times j^0 \frac{nF}{RT} \quad \text{Eq.5- 8}$$

$$-\frac{dj_E}{dx} = \frac{dj_S}{dx} = a \times j^0 \frac{nF}{RT} \times (E - E^0) \quad \text{Eq.5- 9}$$

The change in the reaction rate can then be written as:

$$-\frac{d^2 j_E}{dx^2} = \frac{d^2 j_S}{dx^2} = a \times j^0 \frac{nF}{RT} \times \frac{d(E-E^0)}{dx} \quad \text{Eq.5- 10}$$

$$-\frac{d^2 j_E}{dx^2} = \frac{d^2 j_S}{dx^2} = a \times j^0 \frac{nF}{RT} \times \left(-\frac{i_E}{\sigma} + \frac{i_S}{\kappa}\right) = a \times j^0 \frac{nF}{RT} \times \left(-i_S\left(\frac{1}{\kappa} + \frac{1}{\sigma}\right) + \frac{i}{\kappa}\right) \quad \text{Eq.5- 11}$$

The solution to this differential equation is [107]:

$$\frac{j_S}{j} = \frac{\kappa}{\kappa+\sigma}\left[1 + \frac{\left(\frac{\sigma}{\kappa}\right)\sinh[\upsilon(1-x/L)] - \sinh[\upsilon x/L]}{\sinh[\upsilon]}\right] \quad \text{Eq.5- 12}$$

where:

$$\upsilon = L[a \times j^0 \frac{nF}{RT}\left(\frac{1}{\kappa} + \frac{1}{\sigma}\right)]^{0.5} \quad \text{Eq.5- 13}$$

Using wastewater as the electrolyte, $\sigma \gg \kappa$, so Eq.5-11 simplifies to:

$$\frac{j_S}{j} = \frac{\sinh[\upsilon(1-x/L)]}{\sinh[\upsilon]} \quad \text{Eq.5- 14}$$

$$\upsilon = L\left[\frac{a}{j^0 \frac{nF}{RT}\kappa}\right]^{0.5} \quad \text{Eq.5- 15}$$

The effective conductivity of the solution phase can then be calculated using the Bruggeman equation:

$$\kappa = \kappa_E \varepsilon^{1.5} \quad \text{Eq.5- 16}$$

where κ_E is the electrolyte conductivity (S/m), and ε is the porosity of the electrode. The effectiveness of the 3D electrode (defined as the ratio between the observed current and the theoretical current if the electrode potential was everywhere the same as the maximum observed at position L [116]) can then be calculated using the following simplified Equation:

$$\varphi = \frac{\tanh[\upsilon]}{\upsilon}$$ Eq.5- 17

The effectiveness values can be calculated to estimate the electro-active thickness of the 3D electrode using the system parameters of κ_E = 0.5 S/m, a = 4×10^4 m^2/m^3, ε = 0.4, j^0 = 0.4 A/m^2.

5.4 Results and discussion

5.4.1 Performance stabilization

During the inoculation period, the voltage (through the 500 Ω load) increased from 0.05 V to 0.75±0.05 V within 2 weeks and remained stable after. The FPMFCs were then operated with synthetic wastewater to examine the electricity generation resulting from the *exoelectrogenic* activity of the microorganisms present in the biofilm attached to the anode, as opposed to those present in the wastewater feed. Operation of the FPMFCs with synthetic wastewater did not affect the voltage indicating that the anode potential was controlled by the biofilm-ethanol redox potential. The FPMFCs operation with synthetic wastewater was continued for 2 months before carrying out the performance characterization.

Four months after the operation started, the cathode and the PEM of each FPMFC were replaced with a fresh cathode and a re-treated membrane. The voltage across a 500 Ω load was monitored prior to further electrochemical measurements. Voltage values of ca. 1.1 V were recorded immediately after the operation started. The voltage, however, dropped during the first 24 hours of the operation and stabilized at 0.76±0.01 V, which was most likely due to the gradual development of the anodic and cathodic mixed potential. The OCV was monitored once the stabilization of the voltage was achieved.

5.4.2 Performance improvement

The effect of the GF anode surface treatment prior to the biofilm growth was evaluated in an operating FPMFC. The surface of the GF anode was treated with a 1 M boiling solution of HNO_3 for 1 hour. Figure 5-4 shows the performance of the 2 mm FPMFC using the treated (activated) and the untreated (inactivated) GF electrodes. The activated GF electrode showed superior performance over the entire polarization curve, with a superficial peak power density of 0.24±0.02 W/m^2 whereas; previously the same configuration using an inactivated electrode had only generated 0.09 W/m^2.

The Ohmic resistance of the 2 mm FPMFC was $74\times10^{-4}\pm7\times10^{-4}$ $\Omega.m^2$ without hot-pressing the PEM to the cathode. Hot-pressing the PEM to the cathode previously in chapter 4 had resulted in a lower Ohmic resistance ($40\times10^{-4}\pm4\times10^{-4}$ $\Omega.m^2$). Due to the low current generated by the FPMFC using an inactivated GF substrate, a lower Ohmic resistance did not result in a higher peak power density. This was because the Ohmic resistance was not the main issue limiting the performance. It is clear from the polarization curve in Figure 5-4 that the improvement in the performance was mainly in the kinetic region. The activated electrode generated a maximum current density of 1.5 A/m^2, higher than that generated using the inactivated electrode (<0.4 A/m^2). This indicates that the GF-biofilm interface was a major factor in the generation of current. In fact, up to current densities as high as 1.5 A/m^2, the FPMFC using the activated anode did not show any mass transfer limitation.

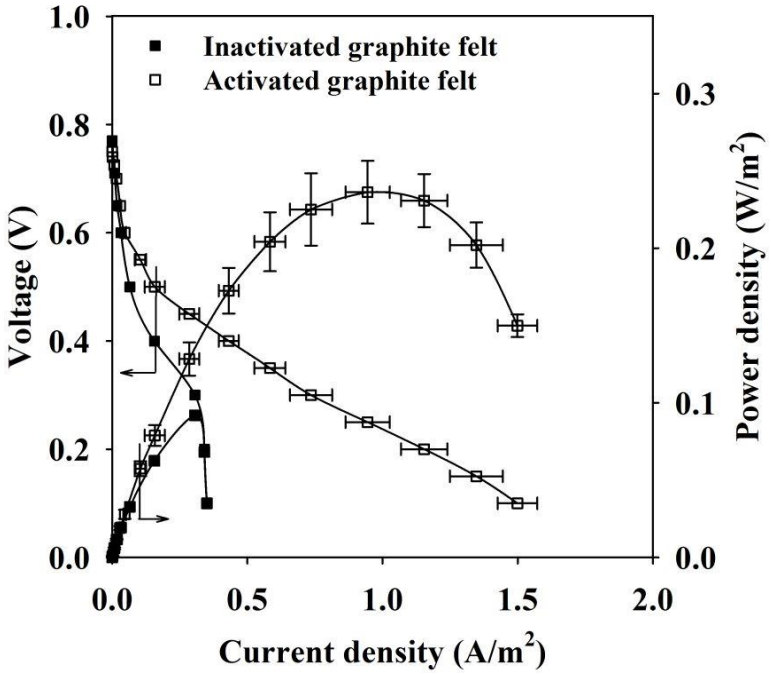

Figure 5-4 Polarization and power density curves of the 2 mm FPMFC using activated (using a 1 M boiling solution of HNO_3) and inactivated (as received) GF anodes. Error bars represent the standard deviation between three experiments.

As the objective of using 3D anodes is to increase the available surface area for the bio-catalyst attachment, the anode surface activation can be very important for the extent of the microbial colonization on this large surface. The surface activation of the carbon substrate can improve the performance significantly through improving the overall hydrophilicity of the graphite material [113, 117, 118], enhancing the biocompatibility of the carbon material as well as facilitating the immobilization of bacteria [119], and improving mass transfer within the porous electrode matrix [120].

5.4.3 Performance using additional layers of GF

5.4.3.1 Power generation

To investigate the electro-active thickness of the 3D GF substrate and study the effect of the active surface area, the 2 mm, 4 mm, and 8 mm FPMFCs were operated using 1, 2, and 3 packed layers of GF, respectively. The thickness of the GF electrode was 2 mm, 4 mm, and 6 mm. Performance of the FPMFCs was characterized after 4 months of stable power production using an external load of 500 Ω. The OCV values stabilized in less than 10 hours, and gave 0.75±0.01 V, 0.75±0.01 V, and 0.76±0.01 V for the 2 mm, 4 mm, and 6 mm thick GF, respectively. Similar OCV values were likely due to similar mixed potentials in all three FPMFCs with similar electrode spacing. Even though thicker anode electrode may lead to less oxygen diffusing into the deeper layers of GF, a major contribution to the mixed potentials comes from the crossover of the fuel (ethanol and produced acetate as the ethanol degradation byproduct). The effect of the crossover on the development of the mixed potentials (possibly along with the effect of the pH increase at the cathode) has been shown to be more visible on the cathode performance compared to the anode performance [31, 80]. The cathode in all three FPMFCs was separated from the synthetic wastewater by Nafion®117, resulting in similar fuel crossover patterns. Therefore, this resulted in no significant variation in the OCV values as the anode compartment depth increased within the applied range.

All three FPMFCs gave similar Ohmic resistance values due to their similar electrode spacing. The superficial peak power density, however, increased as the thickness and consequently the actual surface area of the anode increased (while the surface area of the PEM and the cathode remained the same). Using 4 mm and 6 mm thick GFs, the peak power density

was 0.35±0.03 W/m^2 and 0.52±0.03 W/m^2, respectively (Figure 5-5). These values were higher than that reported for the 2 mm thick GF (0.24±0.02 W/m^2). They corresponded to an increase in the peak power density of 48% and 118% using the 4 mm and 6 mm GFs, respectively, compared to that using the 2 mm GF. This did not indicate a directly proportional behaviour with respect to the actual surface area of the anode (ca. 100% and 200% increase in the actual surface area). The peak power density of 0.52 W/m^2 measured for the FPMFC with three packed layers of GF was higher than those reported for the same configuration using active air and oxygen flow cathodes in the literature (0.22 W/m^2 in a single FPMFC with an air flow cathode [13] and 0.72 W/m^2 in a stack of 4 FPMFCs with an oxygen flow cathode [37]).

The effectiveness values were calculated using Eq.5-17 and gave 1, 0.99, and 0.98 for the 2 mm, 4 mm, and 6 mm thick GFs, respectively. These values suggested that the 3D GF electrode was almost fully electro-active within the applied range of thickness and the anode potential was possibly set by the bio-catalyst [3]. This also showed that 3 and 2 packed layers of GF should, under identical conditions, produce a current ca. 2.9 (i.e., 3×0.98/1) and ca. 2.0 (i.e., 2×0.99/1) times higher than that produced by only 1 packed layer of GF, respectively. The measured peak current densities increased by a factor of 2.7 and 1.8 moving from the 2 mm GF to the 6 mm and the 4 mm thick GFs, respectively, which were in reasonable agreement with the theoretical values. The effectiveness values were also in close agreement with those reported by Lorenzo et al. [107] who reported an electro-active thickness to actual thickness ratio of 0.92 for a 0.01 m thick bed of graphite granules (with an average granule diameter of 0.004 m) in a passive-air breathing MFC. Since small overpotentials were assumed for the FPMFCs and therefore, a linear form of the Erdey-Gruz-Volmer-Butler equation was used to

estimate the electro-active thickness, it is likely that the effectiveness of the GF anode was slightly overestimated. For a more accurate estimation, the non-linear form of this equation should be used.

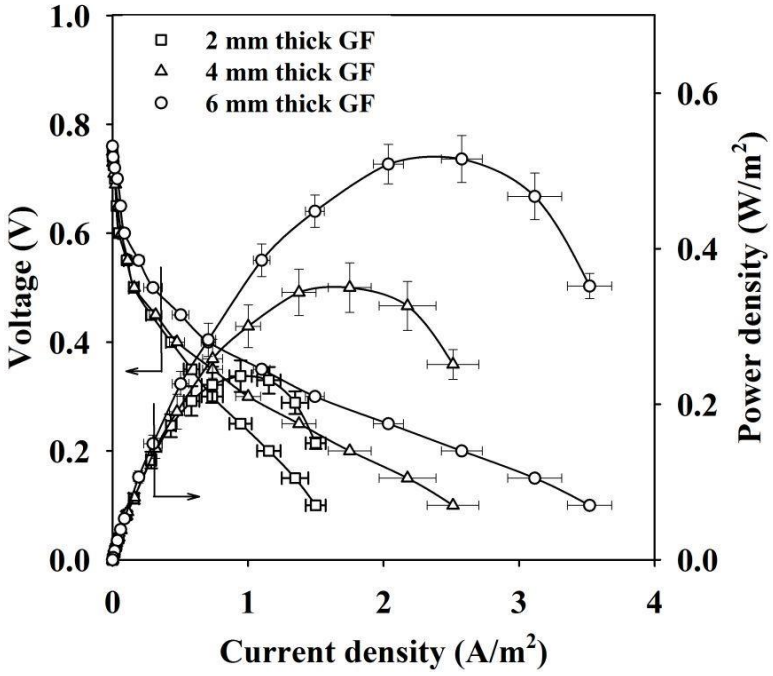

Figure 5-5 Polarization and power density curves of the FPMFCs using 2 mm, 4 mm, and 6 mm thick graphite felt anodes. Error bars represent the standard deviation between three experiments.

5.4.3.2 Wastewater treatment efficiency

As the residence time (RT) increased from 1.7 hours in the 2 mm FPMFC, to 3.3 hours in the 4 mm FPMFC, and 6.7 hours in the 8 mm FPMFC, the COD removal efficiencies also increased from 65±2% to 82±2% and 91±3%, respectively. When considering the rate of the COD removal, it gave values of 2.7±0.1, 1.7±0.1, and 1.0±0.1 kg/m^3/hr of RT in the 2 mm, 4 mm, and 8 mm FPMFCs, respectively. This indicated that to achieve similar COD removal

efficiencies as the 2 mm FPMFC, the 4mm and 8 mm FPMFCs could be operated with a higher flow-rate which could potentially enhance the convective mass transfer within the 3D electrode.

The CE values were 10.7±0.5%, 14±1%, and 17.4±0.8% for the 2 mm, 4 mm, and 8 mm FPMFCs, respectively. This slight increase in the CE resulted mainly from the increased current generation. A possible contribution to the CE could also come from the microbes growing closer to the PEM which could scavenge the oxygen diffusing through the air-breathing cathode and the PEM. This oxygen consumption was also accompanied by the ethanol degradation which did not yield electrical current. However, it likely resulted in reduced oxygen concentration in deeper layers of the anode, thereby yielding enhanced anaerobic bio-catalytic activities.

5.4.4 Performance using a single layer of GF

5.4.4.1 Power generation

To investigate the effect of the electrode spacing in the flat-plate configuration, the FPMFCs were also operated with a single layer of GF placed at the very end of the anode chamber. The electrode spacing using 1 layer of GF was ca. 0.5×10^{-3} m, 2.5×10^{-3} m, and 6.5×10^{-3} m for the 2 mm, 4 mm, and 8 mm FPMFCs, respectively. The OCV readings stabilized in less than 10 hours of the operation at open circuit, and gave 0.76±0.01 V and 0.77±0.01V for the 4 mm and 8 mm FPMFCs, respectively. In addition, the Ohmic resistance increased significantly from $74\times10^{-4}\pm7\times10^{-4}$ $\Omega.m^2$ in the 2 mm FPMFC to $109\times10^{-4}\pm4\times10^{-4}$ $\Omega.m^2$ in the 4 mm FPMFC and $157\times10^{-4}\pm7\times10^{-4}$ $\Omega.m^2$ in the 8 mm FPMFC (Figure 5-6), which approximately corresponded

to Ohmic overpotentials caused by gaps of ca. 2×10^{-3} m and ca. 6×10^{-3} m filled with the synthetic wastewater.

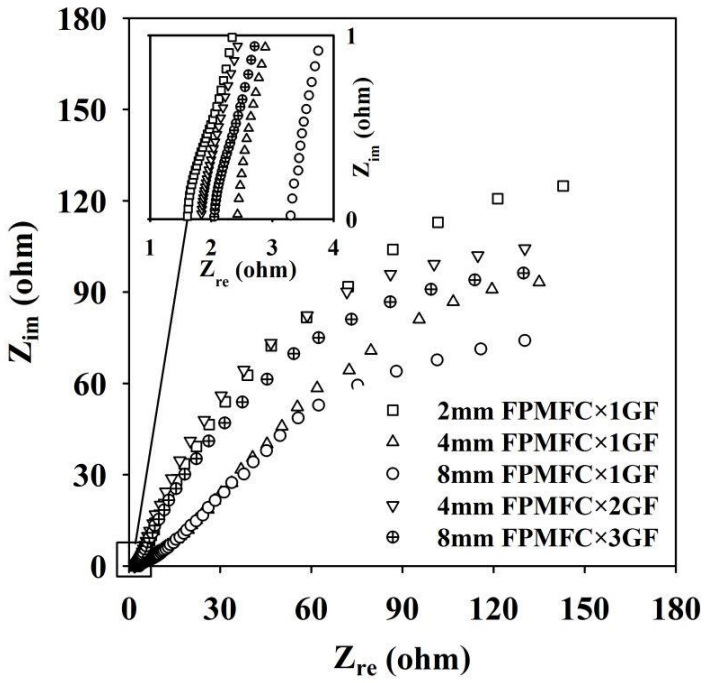

Figure 5-6 Nyquist plots of different FPMFC configurations

No significant trend in the peak power density was observed as the electrode spacing decreased within few millimeters. The 2 mm, 4 mm, and 8 mm FPMFCs produced peak power densities of 0.24±0.02 W/m^2, 0.24±0.02 W/m^2, and 0.25±0.02 W/m^2, respectively (Figure 5-7). This was likely because the increased Ohmic overpotential due to the increased electrode spacing alleviated the inhibitory effect of the diffused oxygen on the bio-catalyst. The slightly higher peak current density achieved in the 4 mm and 8 mm FPMFC compared to the 2 mm FPMFCs is likely due to the decreased oxygen concentration at the anode of the 4 mm and 8 mm FPMFCs, which likely resulted in improved *exoelectrogenic* activities of the bio-catalyst.

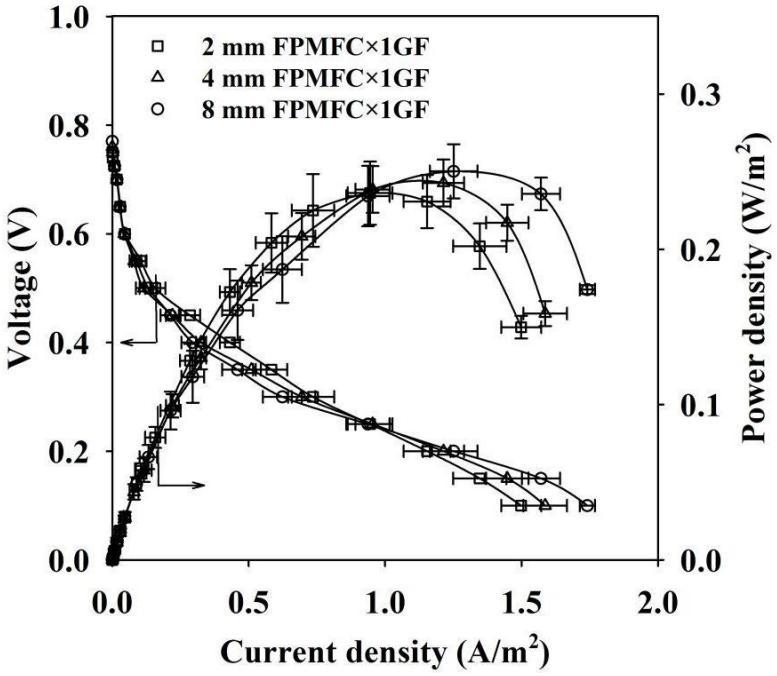

Figure 5-7 Polarization and power density curves of the FPMFCs with different depth of the anode chamber and using a single layer of the GF anode. Error bars represent the standard deviation between three experiments.

5.4.4.2 Wastewater treatment efficiency

The COD removal rates were 1.3±0.1 and 0.6±0.1 kg/m^3/hr of the RT in the 4 mm and 8 mm FPMFCs, respectively. This decrease, compared to the 4 mm and 8 mm configurations applying 2 and 3 layers of GF, respectively, was due to less effective utilization of the anode chamber space. Application of a single layer of GF increased the portion of the wastewater bypassing the 3D GF electrode. Similar conclusion was presented by Dekker et al. [37], who reported that the deformation of the Ralex® CEM towards the cathode in a two-chamber FPMFC yielded an increased anodic and a decreased cathodic chamber volume, and therefore, resulted in the wastewater bypassing the anode. Hence, it is critical to utilize the anode chamber

more effectively to achieve high removal efficiencies as well as to address the potential mass transfer issues within the 3D anode electrode. The CE values did not vary significantly with the electrode spacing (10.7±0.5 %, 11.7±0.6 %, and 13.0±0.2 % for the 2 mm, 4 mm, and 8 mm FPMFCs, respectively), but they were lower than those reported for the configurations using 2 and 3 layers of GF. A summary of the FPMFC characteristics and performance data are presented in Table 5-1.

Table 5-1 Comparison of the performances of different FPMFC configurations (i.e., variation in the depth of the anode chamber and the thickness of the GF anode). Error values represent the standard deviation between three experiments.

FPMFC	Anode	Cathode	Separator /Electrolyte	Internal resistance[10]		Power density[11]		OCV (V)	Effectiveness (η)	COD removal efficiency (%)	Ref.
				$\times 10^{-4}$ ($\Omega.m^2$)	$\times 10^{-6}$ ($\Omega.m^3$)	(W/m^2)	(W/m^3)				
2 mm	1×GF	Passive air-breathing Pt/C	Nafion®117 0.05 M PBS	40±4	8.4±0.8	0.09	44	0.77±0.01	-	55[12]	Chapter 4[13]
2 mm	1×GF	Passive air-breathing Pt/C	Nafion®117 0.05 M PBS	74±7	16±1	0.24±0.02	113±10	0.75±0.01	1	65±2	This chapter[14]
4 mm	2×GF			79±7	33±3	0.35±0.03	83±8	0.75±0.01	0.99	82±2	
8 mm	3×GF			82±6	69±5	0.52±0.03	61±4	0.76±0.01	0.98	91±3	
4 mm	1×GF			109±4	46±2	0.24±0.02	58±4	0.76±0.01	1	62±2	
8 mm	1×GF			157±7	115±6	0.25±0.02	30±2	0.77±0.01	1	58±2	

[10] Based on the anode electrode geometric surface area and the anode compartment volume
[11] Based on the anode electrode geometric surface area and the anode compartment volume
[12] The FPMFC was not at a steady state yet.
[13] Using as received (inactivated) graphite felt anode electrode
[14] Using HNO_3 treated (activated) graphite felt anode electrodes

5.5 Conclusions

The effect of the GF substrate surface treatment, GF active surface area, and anode chamber depth (electrode spacing) on the performance of the passive air-breathing FPMFC was investigated. The treatment of the surface of the GF substrate with a 1 M boiling solution of HNO_3 before inoculation had a significant positive effect on the anode performance, attributed mainly to the increased hydrophilicity of the graphite structure and improved mass transfer, which likely enhanced the microbial colonization. The performance of the passive air-breathing FPMFCs improved through addition of extra layers of GF as the GF electrodes were indicated to be almost fully electro-active. The superficial peak power density increased as the thickness of the GF substrate increased, resulting in 48% (to 0.35±0.03 W/m^2) and 118% (to 0.52±0.03 W/m^2) increase in the superficial peak power with an increase of ca. 100% and 200% in the thickness and the actual surface area of the anode, respectively. Interestingly, with otherwise similar conditions, increasing the electrode spacing in the FPMFC did not affect the superficial peak power density. The decreased concentration of oxygen at the anode as the electrode spacing increased within the range of ca. 0.5×10^{-3} m- 6.5×10^{-3} m explained the imperceptible effect of the increased Ohmic overpotential on the peak power.

Chapter 6: Separator characterization in the non-inoculated and inoculated setups

6.1 Introduction

The engineering and operation of the passive air-breathing FPMFC, presented in chapters 4 and 5, indicated the critical effect of the separator component in sustainable power generation in this configuration. Therefore, a systematic approach was adopted to study the separator characteristics and its effect on the performance of the passive air-breathing FPMFC in this chapter. For this purpose, 8 separators were selected and their ionic resistivity, proton transport number, and oxygen crossover were studies in a non-inoculated passive air-breathing setup, and the fuel (ethanol and acetate) crossover was studied in a non-inoculated aqueous setup. The surface hydrophobicity and morphology of the separators were also investigated, to spot the possible links between the separator characteristics and the FPMFC performance. The selected separators were then examined in three passive air-breathing FPMFCs with different electrode spacing (ca. 0.5×10^{-3}, 2.5×10^{-3} m, and 6.5×10^{-3} m), to investigate the interplay between the electrode spacing and the separator characteristics.

6.2 Experimental

6.2.1 Separator characterization in the non-inoculated setups

6.2.1.1 Selected separators and characteristics

Aquivion®FPSA E79-03S (Solvay Solexis, Italy), SciMat®700/20 (SciMat Ltd., UK), Celgard®5511 (Celanese, USA), Zirfon® (AGFA, Belgium), Glass fiber filter (Millipore,

USA), Nylon mesh filter (Millipore, USA), and J-cloth (Associated Brands Inc., Canada) were selected for the characterization. Nafion®117 (DuPont, USA) was used as the baseline. Table 6-21 and Table 6-2 provide available information on the selected separators.

Table 6-1 Information on the material and structure of the selected separators

Separator	Information
Nafion®117	Sulfonate groups attached to a hydrophobic fluorocarbon backbone
Aquivion®	Sulfonate groups attached to a short-side-chain perfluoropolymer
Celgard®	Micro-porous polypropylene
Zirfon®	Micro-porous polymer mesh coated with a mixture of ZrO_2 and polysulfone
SciMat®	UV-treated micro-porous polypropylene
Nylon mesh	Woven Nylon strands
Glass fiber filter	Web of glass fibers
J-cloth	Woven cellulose fibers

Table 6-2 Thickness and pore size of the selected separators

Separator	Nafion117	Aquivion	Celgard	Zirfon	Nylon mesh	Glass fiber	SciMat	J-cloth
Thickness ($\times 10^{-6}$ m)	178	30	200	500	55	380	144	300
Pore size ($\times 10^{-6}$ m)	-	-	0.04	0.15	20	0.7	30	500

The selected separators were evaluated by studying oxygen crossover, indicated as the mass transfer and diffusion coefficients of oxygen (k_O and D_O), ethanol crossover, indicated as the mass transfer and diffusion coefficients of ethanol (k_E and D_E), acetate crossover (as a product of ethanol degradation), indicated as the mass transfer and diffusion coefficients of acetate (k_A and D_A), the ionic resistivity and conductivity (R_S and κ_S), the proton transport number (n_{H^+}), and the surface hydrophobicity and morphology.

6.2.1.2 Characterization techniques and setups

The tests were performed in a glass cell (Figure 6-1), consisting of two compartments (8×10^{-5} m^3 volume of each) isolated by a separator holder. The open surface area of the separator using this setup was 2×10^{-4} m^2 (2 cm^2). During the characterization, the separators were sandwiched between the two compartments using the holder. Two O-rings were used to ensure proper sealing. Neoprene stoppers were used to seal the compartments from the lab environment when required.

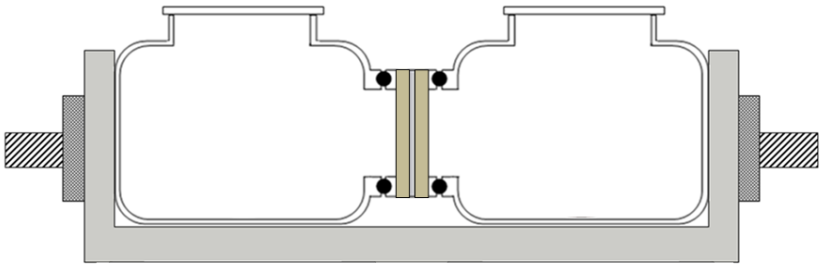

Figure 6-1 Separator characterization setup

Oxygen and fuel crossover

The concentration of DO in the anode chamber was used for the evaluation of the oxygen crossover. The DO measurement was carried out using a DO probe inserted into the anode (aqueous) chamber of the glass cell. The mass transfer coefficient of oxygen for each separator was measured using a 0.05 M PBS in the aqueous chamber and air in the other (Figure 6-2).

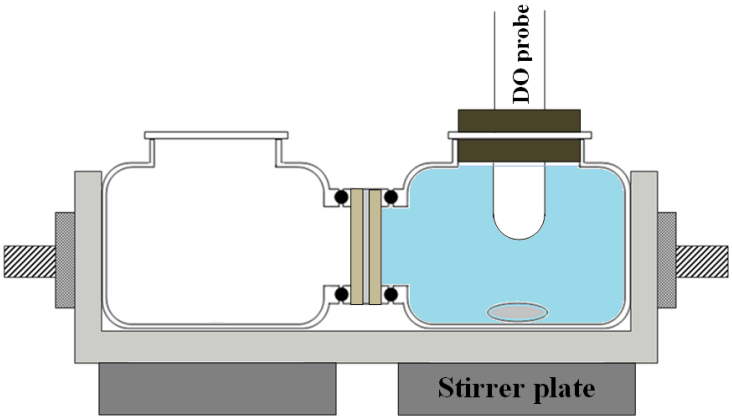

Figure 6-2 Oxygen crossover setup

In this test, both chambers were filled with the PBS initially. A bubbler was inserted into the anode chamber through the rubber stopper to assure an ambient pressure inside (no pressurization). The aqueous chamber was then sealed and sparged with N_2. The other chamber was then evacuated using a syringe, to create the air-breathing configuration. The DO concentration in the aqueous chamber was then monitored with time. The mass transfer (k_O, m/s) and diffusion (D_O, m^2/s) coefficients were calculated using the mass balance [25]:

$$k_O = \frac{V}{At} \ln\left[\frac{c_1}{c_1 - c_2}\right],\ D_O = k_O Y \qquad \text{Eq.6- 1}$$

where c_1 is the saturated oxygen concentration (M) on the air side of the separator, c_2 is the DO concentration (M) in the aqueous side at time t (s), V is the volume of water in the aqueous-chamber (m^3), A is the surface area (m^2), and Y is the thickness of separator (m).

A Refractive index (RI) detector (Waters 2414 refractive index detector, Waters, UK) along with a Shimadzu high-performance liquid chromatography (HPLC) pump were used for assessing the fuel (ethanol and acetate) crossover. The mass transfer coefficients in each separator were measured using the glass cell filled with DI water in both chambers and adding either ethanol or acetate to one chamber only (donor compartment). Ethanol or acetate was then injected into the donor compartment and allowed to diffuse over time. The contents of the fuel-free chamber were cycled through the RI detector at a flow rate of 8.3×10^{-8} m^3/s by the HPLC pump (Figure 6-3), where the increasing concentration of the fuel (ethanol or acetate) was monitored with time.

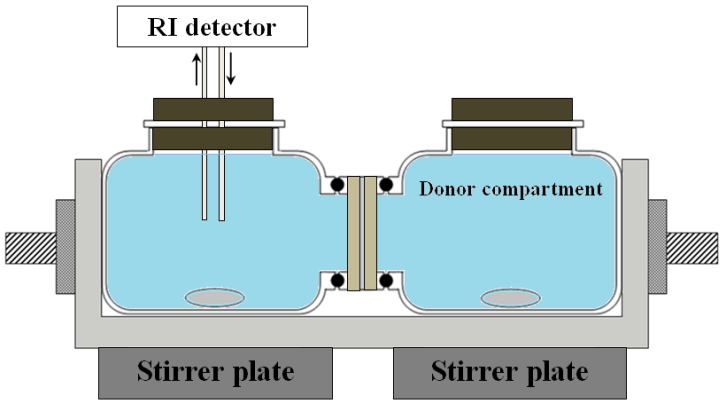

Figure 6-3 Fuel crossover setup

The mass transfer ($k_{E/A}$, m/s) and diffusion ($D_{E/A}$, m^2/s) coefficients of ethanol or acetate were calculated using the mass balance [25]:

$$k_{E/A} = \frac{V}{2At} \ln\left[\frac{c_1}{c_1 - 2c_2}\right],\ D_{E/A} = k_{E/A} Y \qquad \text{Eq.6- 2}$$

where c_1 is ethanol or acetate concentration (M) in the anode (donor compartment) at $t = 0$, c_2 is ethanol or acetate concentration (M) in the cathode at time t (s), V is the volume of the water in either one of the chambers (m^3), A is the open surface area (m^2), and Y is the thickness of the separator (m).

Ionic resistivity

A Potentiostat (VERSASTATE 3, Princeton Applied Research, USA) was used for the electrochemical measurements. The EIS technique was used to investigate the ionic resistivity and conductivity. The aqueous chamber was filled with 0.05 M PBS. Pt-coated carbon paper electrodes were used as the working and the counter electrodes. Two platinum current collectors were used to connect the electrodes to the potentiostat. The ionic resistivity was investigated by sandwiching the separator between the carbon paper electrodes and the current collectors (Figure 6-4 and Figure 6-5). The impedance measurements were performed according to the procedure reported in Appendix A. The Ohmic resistance was determined using the Nyquist plot and was normalized based on the surface area of the separator (2×10^{-4} m^2) to give the ionic resistivity. The ionic conductivity was calculated by normalizing the ionic resistivity based on the thickness of the separator:

$$\kappa_S = Y/R_S \qquad \text{Eq.6- 3}$$

where κ_S is the ionic conductivity (S/m), R_S is the ionic resistivity ($\Omega.m^2$), and Y is the thickness of the separator (m).

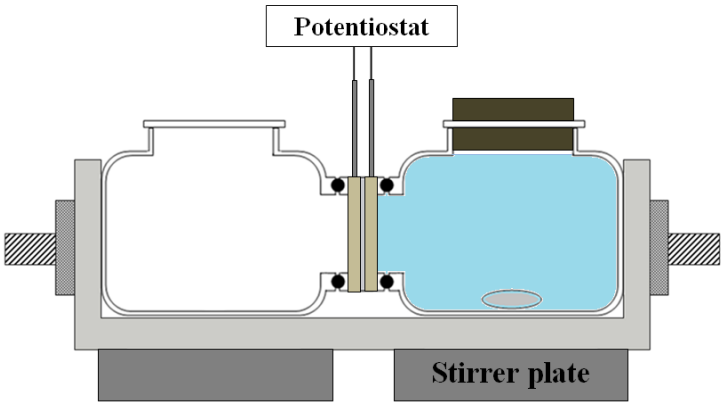

Figure 6-4 Ionic resistivity setup

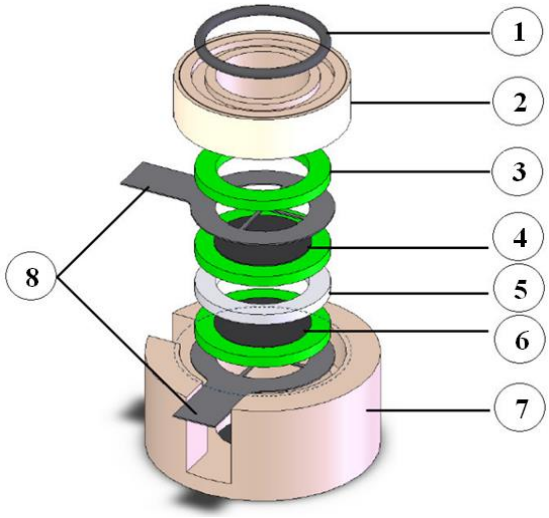

Figure 6-5 Electrode assembly holder: 1) O-ring, 2) holder top, 3) gasket, 4) counter electrode, 5) separator, 6) working electrode, 7) holder base, 8) current collectors [121]

Proton transport number (pH splitting extent)

Chronoamperometry was used to investigate the pH splitting extent. A pH probe was used to monitor the pH. The extent of pH splitting was investigated by measuring the portion of the protons produced in the anode chamber, that were delivered to the cathode chamber by the separator (referred to as the proton transport number [36]). This was measured by monitoring the pH change in the aqueous chamber in relation to the overall electric charge transferred during the Chronoamperometry test. The working electrode was a platinized titanium mesh (placed in the aqueous chamber) and the counter electrode was a Pt-coated carbon paper connected to a platinum current collector. The aqueous chamber was filled with 0.05 M KNO_3 (Figure 6-6). A fixed electric charge of 10 C was transferred at different rates (1-50 A/m^2) and the pH change in the aqueous chamber was monitored.

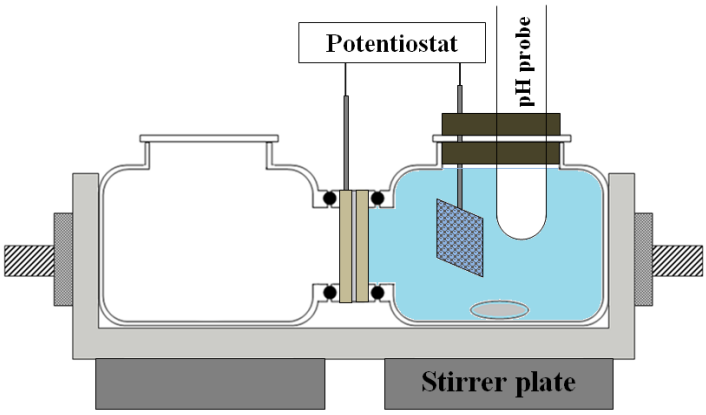

Figure 6-6 pH splitting setup

The proton transport number was then obtained by calculating the electrical current equivalent to the transferred protons [75]:

$$n_{H^+} = (1 - \frac{VF\Delta c_{H^+}^{anode}}{q}) \quad \text{Eq.6- 4}$$

where V is the volume of the electrolyte solution (m^3), F is the Faraday constant (C/mol), $\Delta C_{H^+}^{anode}$ is the change in the protons concentration in the aqueous chamber (mol/m^3), and q is the electric charge (C).

Surface hydrophobicity

The surface hydrophobicity of the separators was investigated by measuring the contact angle of a 10^{-10} m^3 (0.1 µL) water droplet on the surface using a surface Tensiometer (Sigma700, KSV Instruments Ltd.).

Surface morphology

Scanning electron microscopy (SEM) imaging was used to study the morphology of the surface of the selected separators before and after testing in the FPMFC. After 4 weeks of the FPMFC operation, the separators were taken out and prepared for the SEM imaging. The standard preparation of the (bio)fouled (used) and the virgin (unused) samples is presented in the following steps:

Fixation The samples were fixed by immersing in a warm solution of 2.5 wt.% glutaraldehyde in 0.1 M sodium cocadylate buffer (pH=7.4) in a warm water bath at 310 K, for 30-60 minutes. They were then washed with 0.1 M sodium cocadylate buffer solution, three times each for 10 min.

Post-fixation The samples were then immersed in solution of 1 wt.% osmium tetroxide in 0.1 M sodium cocadylate buffer (pH=7.4), at room temperature for 2-4 hours. They were then washed with DI water, three times each for 10 min.

Dehydration The samples were then dehydrated in graded ethanol solutions in water- 30, 50, 70, 80, 90, 96, 100 wt.% for 5-15 minutes, and twice in 100 wt.% ethanol for 15-30 minutes.

Critical point drying, mounting, and sputter coating The samples were then dried in a Tousimis AutoSamDri 815B (Tousimis, USA) critical point dryer, were mounted on the specimen setup with a carbon/silver paste, and coated with a Au/Pd alloy in a Cressington 208HR spotter coater (Cressington, UK).

6.2.2 Separator evaluation in the FPMFCs

6.2.2.1 FPMFC design and components

The passive air-breathing FPMFCs were constructed as previously reported in Chapters 4 and 5. Three FPMFCs were constructed with similar projected surface area (0.05 m × 0.10 m) and three different depths of the anode chamber (2×10^{-3} m, 4×10^{-3} m, and 8×10^{-3} m). Neoprene gaskets (0.5×10^{-3} m in thickness) were installed to provide insulation between the electro-conductive components of the FPMFCs.

Graphite felt was used as the 3D anode material (0.05 m × 0.095 m, 3×10^{-3} m thick, GF-S6-03, Electrolytica, USA). Graphite felt anodes were treated by soaking in pure acetone, and then a 1 M boiling solution of HNO_3 for 1 hour. They were then stored in DI water. Expanded stainless steel sheets were used to support the electronic connection between the anode and the

hosting compartment. This resulted in a 3D anode compression from 3×10^{-3} m to 2×10^{-3} m. The experiments were performed using a single layer of GF placed at the bottom of the anode chamber.

The air cathode consisted of a carbon cloth (projected surface area: 0.05 m × 0.10 m; 50 wt.% wet-proofing, E-TEK, USA) coated on one side with a Pt catalyst layer (Pt loading of 0.01 kg/m^2) facing the membrane and on the other side, with three layers of the 60 wt.% PTFE suspension [98]. A high loading of Pt was adopted to assure that the cathode was not limiting the performance.

All separators (except for the glass fiber filter) were stored in DI water for 24 hours prior to use. The separator and carbon cloth cathode were sandwiched between the anode chamber and the perforated plates, with the catalyst side of the cathode facing the separators and PTFE side facing the air. A new cathode was used for the evaluation of each separator in the FPMFCs.

6.2.2.2 Operation and performance characterization

The previously inoculated passive air-breathing FPMFCs were operated with the synthetic wastewater (prepared as reported in Appendix A). The conditions of the synthetic wastewater, i.e., DO and temperature were controlled at 0% of DO and 303±1 K in the feed tank, respectively. The feed container was maintained oxygen-free by continuous N_2 sparging. A *methanogens* inhibitor (2-bromoethanesulfonate at a concentration of 0.3×10^{-3} M [115]) was added to both the primary treated and the synthetic wastewaters to prevent *methanogenesis* from ethanol [99]. The cathode was replaced with a new cathode prior to the characterization of each separator. The FPMFCs were operated using each separator for two weeks, with the

electrodes connected through a 500 Ω external load to ensure stable performance before characterizing the performance.

The performance of the FPMFCs was characterized by investigating the superficial and volumetric power density and polarization curves, Ohmic resistance, Coulombic and COD removal efficiencies. Development of the polarization and power density curves, measurement of the internal resistance, and COD removal efficiency were performed according to the procedure reported in the Appendix A.

6.2.3 Error calculations

The uncertainty of the current and voltage measurements done by the potentiostat was <0.2%. Hence, to calculate the actual error values associated with the polarization curves, all experiments were triplicated. For this purpose, the anode remained the same for all experiments while the separator, the cathode, and the feed solution were replaced with a new separator, a new cathode, and a fresh feed solution, respectively, for each replication test.

To calculate the error values associated with the investigation of the separator characteristics, all characterization tests were triplicated. For this purpose, the separator, the electrodes, and the electrolyte solution were replaced with a new separator, new electrodes, and a fresh electrolyte solution, respectively, for each replication test.

The standard deviation between the measurements of the replication tests was calculated according to:

$$\sigma = \sqrt{\frac{\sum_{i=1}^{N}(x_i - \bar{x})^2}{N}} \qquad \text{Eq.6- 5}$$

where x_i is the data value in measurement number i, $\bar{x}$ is the mean (or average) of a set of data values (sum of all of the data values divided by the number of data values), and N is the number of data points in the sample population (or number of the experiments, which in this chapter is equal to three). All reported error bars on the graphs and values within the text for the reported data are strictly meant for illustration as they represent the standard deviation for the results obtained over three runs.

6.3 Results and discussion

6.3.1 Separator characteristics

The characteristics of the separators were related to their material, structure, thickness, and pore size. Except for the Nylon material, all other diaphragms and IEMs showed hydrophilic behaviour in contact with water.

Figure 6-7 presents the SEM images from the surface of the virgin (unused) separators. The average pore size of SciMat® and J-cloth were estimated to be 3×10^{-5} m and 5×10^{-4} m using the SEM images.

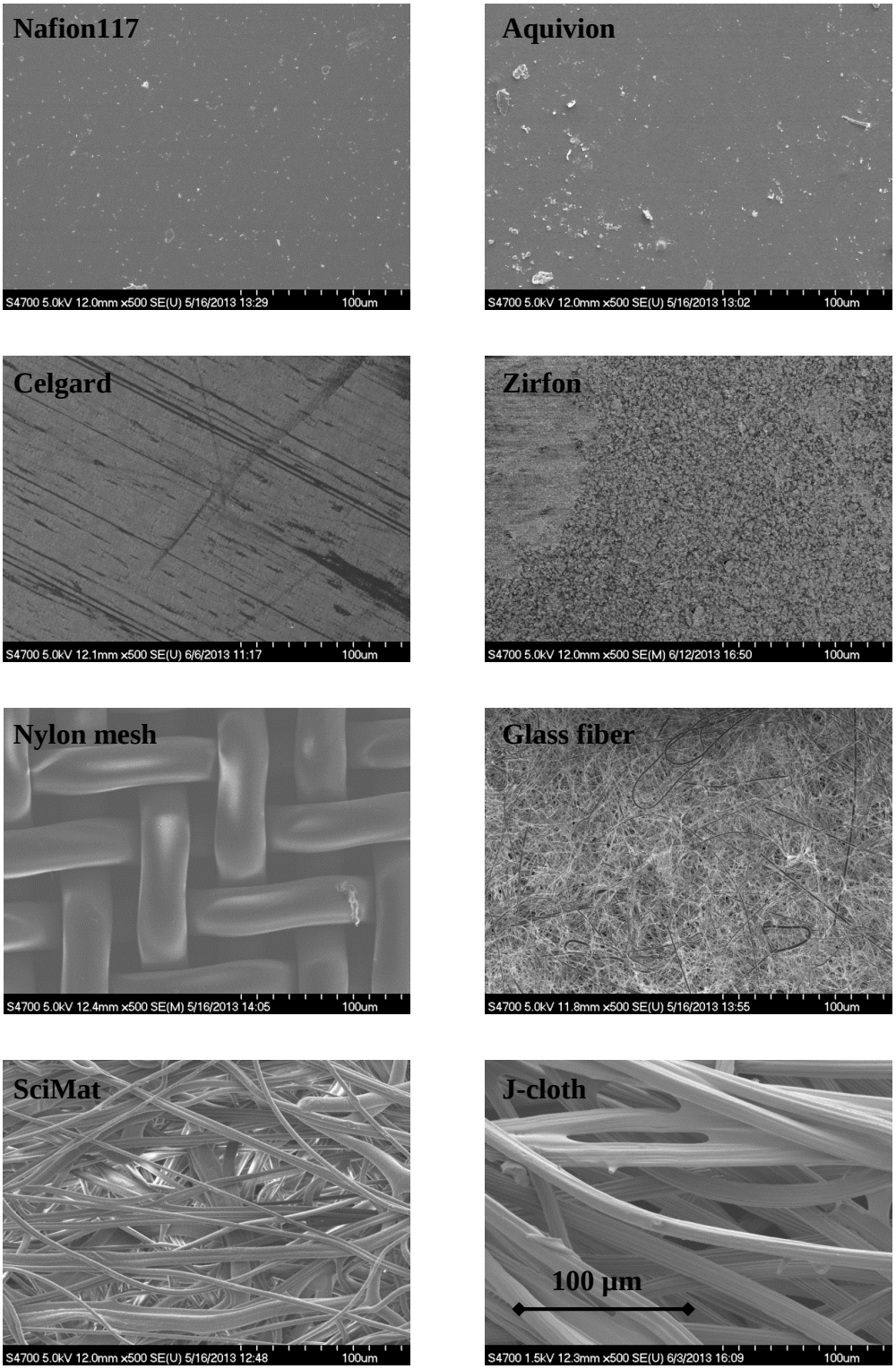

Figure 6-7 SEM images from the surface of the virgin (unused) separators

Nafion®117 was in general less susceptible to oxygen and ethanol diffusion compared to the other separators (Figure 6-8 A). The mass transfer coefficient of oxygen in Nafion®117 was ca. 0.3×10^{-6} m/s, one order of magnitude lower than those previously reported in the literature (ca. 3×10^{-6} m/s [101]). The mass transfer coefficient of oxygen measured for Zirfon® was also lower than that measured by Pant et al. (ca. 19×10^{-6} m/s [78]) in an aqueous non-inoculated MFC that was being actively aerated at the cathode. The lower mass transfer coefficients of oxygen obtained here was attributed to the passive air-breathing setup used, which decreased the flux of oxygen through the separator, as opposed to the active aeration used in the aqueous setups in the literature. Also, the characterization of the separators independently in a non-inoculated setup eliminated the possibility of oxygen consumption by the biological processes, which could likely affect the mass transfer coefficient of oxygen through the separator.

Aquivion® and glass fiber filter showed the lowest crossover of oxygen, after Nafion®117. The glass fiber filter has in fact been reported to perform excellently compared to the CEMs in the passive air-breathing MFCs with electrode spacing of 0.02 m [31, 80], which is likely due to the low mass transfer coefficient of oxygen and the relatively good ionic conductivity of the glass fiber filter. J-cloth showed the highest crossover of oxygen, as a result of the high flux of oxygen through its large pores.

The ethanol and acetate crossover followed a similar trend as the oxygen crossover, and increased as separators with larger pores were tested. Nafion®117 indicated the smallest and J-cloth indicated the greatest mass transfer coefficients of ethanol and acetate. In general, the

mass transfer coefficients of ethanol and acetate were higher than the oxygen, as a result of the aqueous configuration that was used.

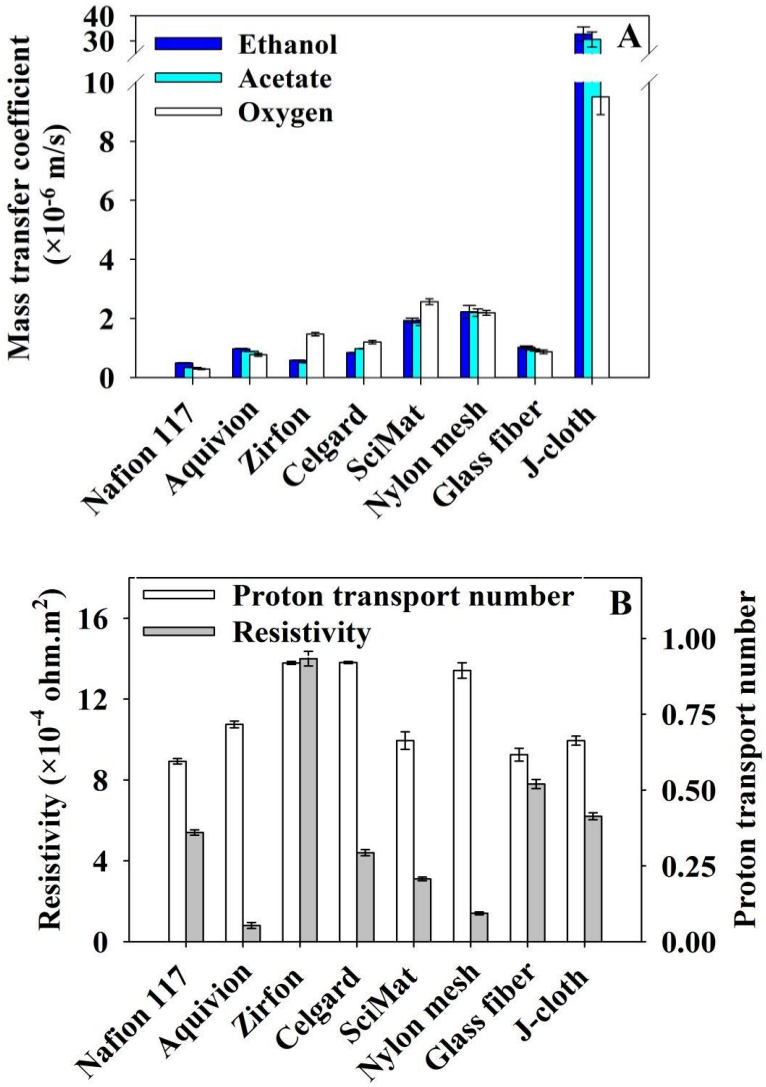

Figure 6-8 A) Oxygen, ethanol, and acetate mass transfer coefficients, B) Proton transport number and ionic resistivity of the selected separators, measured in non-inoculated setups. Error bars represent the standard deviation between three experiments.

The thickness of the separators played a key role in their ionic resistivity. The resistivity, hence, increased as thicker separators were tested. When testing separators with similar thickness, the resistivity decreased as the pore size of the separator increased. The 5×10^{-4} m thick Zirfon® demonstrated the highest resistivity (Figure 6-8 B). Despite its slightly thinner structure compared to Zirfon®, Glass fiber filter showed a much lower resistivity value, due to its larger pores and the super-hydrophilic structure. Aquivion® and Nylon mesh, on the other hand, showed the smallest resistivity towards cations, as a result of their thin structure. The separator resistivity varied from ca. 0.8 $\Omega.m^2$ in Aquivion® up to ca. 14 $\Omega.m^2$ in Zirfon®.

During the pH splitting tests, gas accumulation was observed between the separator and the counter electrode, which was more significant at high current densities. Hence, the carbon paper counter electrode was replaced with a perforated carbon paper electrode, to release the accumulated gases. Since the pH splitting results indicated no significant variation in the proton transport number within the applied range of current density, the mean value of the proton transport number was reported.

The pH splitting results showed that, despite using different mechanisms of transfer, the IEMs and diaphragms were, to a similar extent, permeable to protons. The variation in the proton transport number of the separator did not follow a significant trend with neither the thickness nor the pore size of the separators. The pH of the anode varied from 2.9 using Nafion®117 (pH of 11 at the cathode) to 3.3 using Celgard® and Zirfon® (pH of 10.2 at the cathode), which corresponded to proton transport numbers of 0.59 in Nafion®117 and 0.92 in Celgard® and Zirfon®. This indicated that even a high proton transport number of 0.92 was insufficient to balance the pH. Despite the excellent properties of Nafion®117, it gave the

lowest proton transport number, which could be attributed to the competitive transfer of K^+ ions versus the protons in the diaphragms and the blockage of the functional groups by K^+ ions in the CEMs.

The cathode potential has been shown to suffer the most from the low proton transport number of the separator, as a buffer solution is usually used at the anode. The lower cathode potentials (0.1- 0.2 V) reported by Zhang et al. [31, 80] using Nylon mesh and glass fiber filters compared to a separator-free passive air-breathing MFC with an electrode spacing of 0.02 m, indicates that the elevated cathode pH due to the pH splitting can affect the cathode performance negatively. In fact, they reported the highest cathode potential when the separator was removed [31].

The increase in the proton transport number from 0.59 to 0.92, in fact, can result in an increase in the equilibrium potential of oxygen reduction reaction (ORR) of ca. 0.04 V (Figure 6-9, at P_{o2}=0.21 bar and T=303 K). Removing the separator (hypothetically), on the other hand, can result in a further increase of ca. 0.14 V in the equilibrium potential of ORR (at the FPMFC inlet pH of ca. 8.5). The permeability of the diaphragms to the PBS in the MFC environment may result in higher proton transport numbers, however, the pH splitting may still be an issue at high current densities [32].

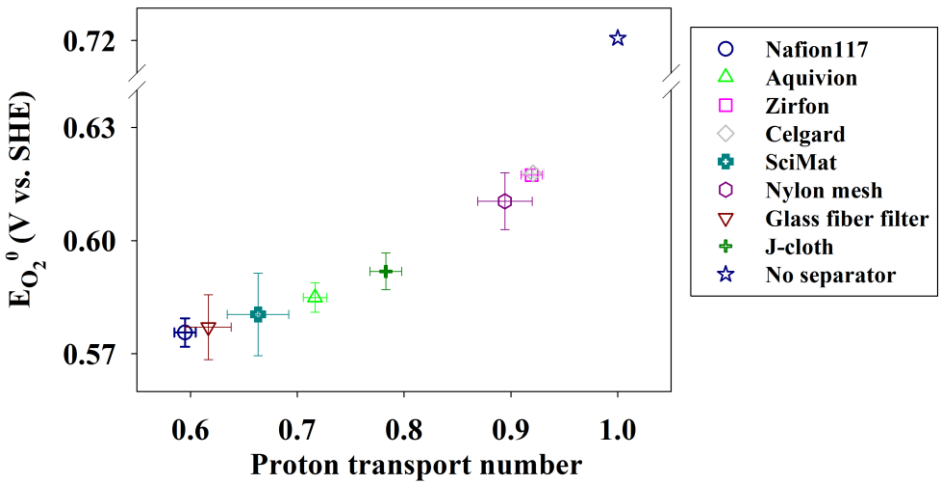

Figure 6-9 Variation in the equilibrium potential of oxygen reduction with the proton transport number of the separator, at P_{o2}=0.21 bar (abs) and T=303 K. Error bars represent the standard deviation between three experiments.

6.3.2 Separators evaluation in the FPMFCs

6.3.2.1 Performance versus the separator characteristics

The superficial peak power density, OCV, and CE were significantly affected by the oxygen, ethanol, and acetate crossover (Figure 6-10). Using the separators with high oxygen and fuel crossover, the peak power density and CE increased more significantly as the electrode spacing increased. In other words, the peak power density and CE indicated a higher sensitivity to the crossover in the 2 mm FPMFC. This sensitivity decreased as the electrode spacing increased. The OCV, on the other hand, showed relatively similar sensitivity to the crossover in all three FPMFCs, and decreased as the crossover increased.

Power generation using the biofilm is likely dependent on the population of the microbial cells (as previously discussed in Chapter 5) contributing to the current generation as well as the rate of the fuel uptake and the electron transfer to the anode [122]. Since the random repeating of the MFC tests resulted in fairly replicable performance data, it was concluded that the morphology of the microbial communities (and their characteristics) in the FPMFCs likely did not change within the period of operation. Therefore, the presence of oxygen in the anode chamber likely reduced the number of the cells contributing to the current generation. As the electrode spacing increased, the concentration of oxygen decreased within the biofilm resulting in a less significant effect of the oxygen crossover in the 4 mm and 8 mm FPMFCs, and more cells contributing to the current generation. That is why a larger variation in the peak power density and CE was observed as the electrode spacing decreased.

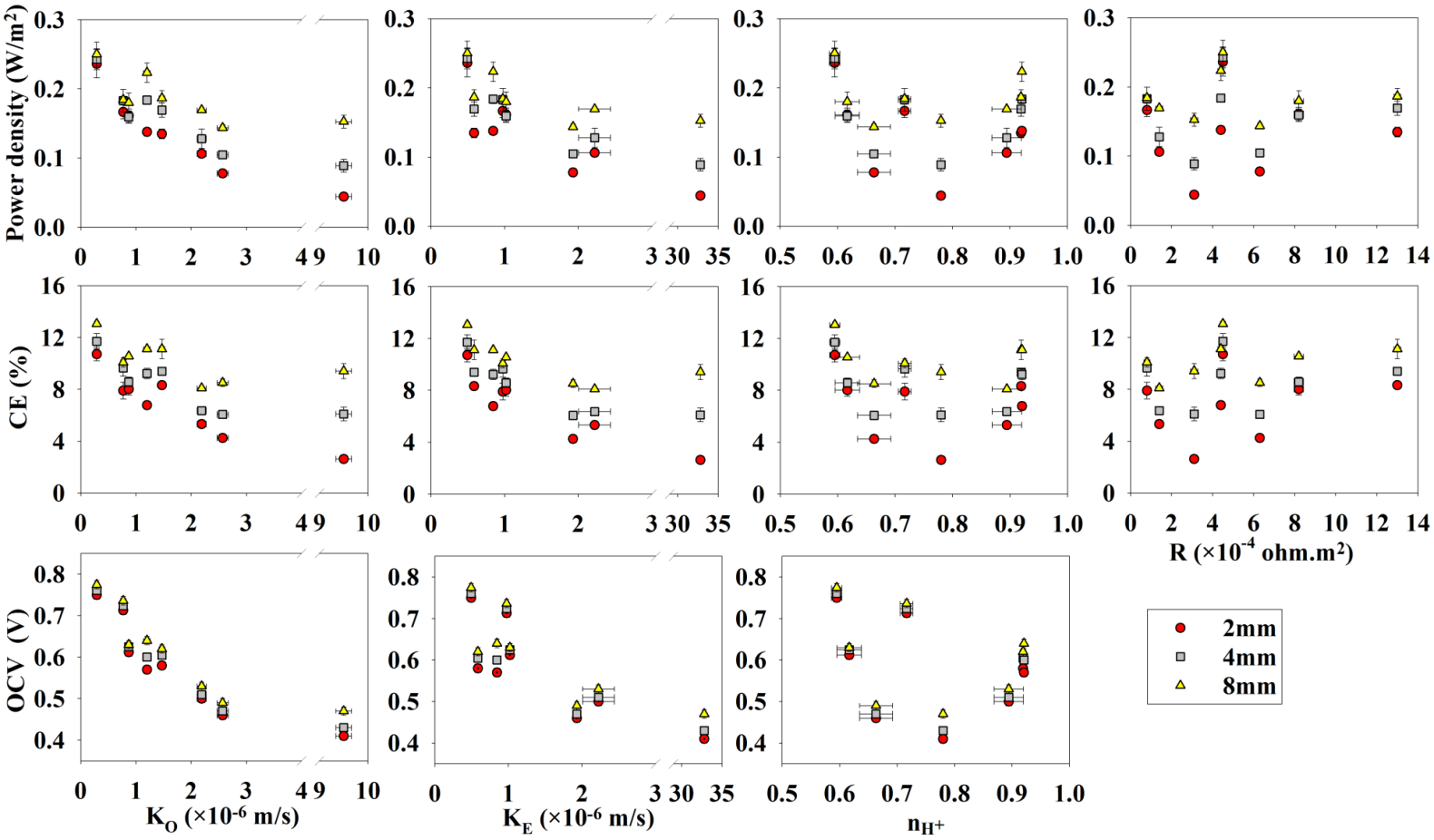

Figure 6-10 Performance of the 2 mm, 4 mm, and 8 mm FPMFCs versus the separator characteristics. Error bars represent the standard deviation between three experiments.

Table 6-3 presents the OCV, the superficial and volumetric peak power densities, and the CE of the 2 mm, 4 mm, and 8 mm FPMFCs using the selected separators. Figure 6-11 shows the polarization and power density curves. The highest peak power density in the 2 mm FPMFC was produced using Nafion®117 (0.24±0.02 W/m^2) which gave the lowest mass transfer coefficient of oxygen, ethanol, and acetate. Aquivion® and glass fiber filter produced similar peak power densities after Nafion®117, likely due to the similar crossover of oxygen and fuel, and proton transport number. The generated peak power density further decreased using Nylon mesh, SciMat®, and Celgard®, followed by a dramatic decrease when J-cloth was used, due to the high crossover in J-cloth.

Due to the slightly larger electrode spacing in the 4 mm FPMFC and the developed concentration profile, the concentration of oxygen at the anode and hence, the contribution of the oxygen crossover to the performance decreased. That is likely why diaphragms performed better in the 4 mm compared to the 2 mm FPMFC. The peak power density did not vary significantly using Nafion®117, Aquivion®, and Glass fiber filter while it increased using diaphragms with higher permeability to oxygen and ethanol. Zirfon® and Celgard® showed a greater extent of increase in the peak power density, while the increase was less significant using the Nylon mesh, SciMat®, and J-cloth. Further increase of the electrode spacing in the 8 mm FPMFC resulted in an increased Ohmic overpotential, however, the 8 mm FPMFC showed a better performance than the 4 mm and the 2 mm FPMFCs. Celgard® produced a peak power density of ca. 0.22 W/m^2 in the 8 mm FPMFC, close to that produced using Nafion®117, which was due to a decreased oxygen concentration at the anode and an improved cathode performance.

Table 6-3 Performance characteristics of the 2 mm, 4 mm, and 8 mm FPMFCs with the selected separators. Error values represent the standard deviation between three experiments.

Separator	OCV (V) ± 0.01			Superficial peak power density (W/m^2)			Volumetric peak power density (W/m^3)			Coulombic efficiency (%)		
	2mm	4mm	8mm	2mm	4mm	8mm	2mm	4mm	8mm	2mm	4mm	8mm
Nafion®117	0.75	0.76	0.77	0.24±0.02	0.24±0.02	0.25±0.02	110±8	58±4	30±2	10.7±0.5	11.7±0.6	13.1±0.2
Aquivion®E79-03	0.71	0.72	0.73	0.17±0.01	0.18±0.02	0.18±0.01	79±5	43±4	22±1	7.9±0.6	9.6±0.6	10.1±0.3
Celgard®5511	0.57	0.60	0.64	0.14±0.01	0.18±0.01	0.22±0.01	65±3	44±1	27±1	6.8±0.3	9.2±0.4	11.1±0.2
Zirfon®Perl	0.58	0.60	0.62	0.14±0.01	0.17±0.01	0.19±0.01	64±3	40±2	22±1	8.3±0.2	9.4±0.3	11.1±0.8
Nylon mesh	0.50	0.51	0.53	0.11±0.01	0.13±0.01	0.17±0.01	50±2	30±3	20±1	5.3±0.2	6.4±0.1	8.1±0.2
Glass fiber filter	0.61	0.62	0.63	0.16±0.01	0.16±0.01	0.18±0.01	77±4	38±2	21±2	8.0±0.5	8.6±0.4	10.5±0.1
SciMat®700/20	0.46	0.47	0.49	0.08±0.01	0.10±0.01	0.14±0.01	37±1	25±1	17±1	4.3±0.1	6.1±0.1	8.5±0.3
J-cloth	0.41	0.43	0.47	0.04±0.0	0.09±0.01	0.15±0.01	18±2	21±2	18±1	2.6±0.1	6.1±0.5	9.4±0.6

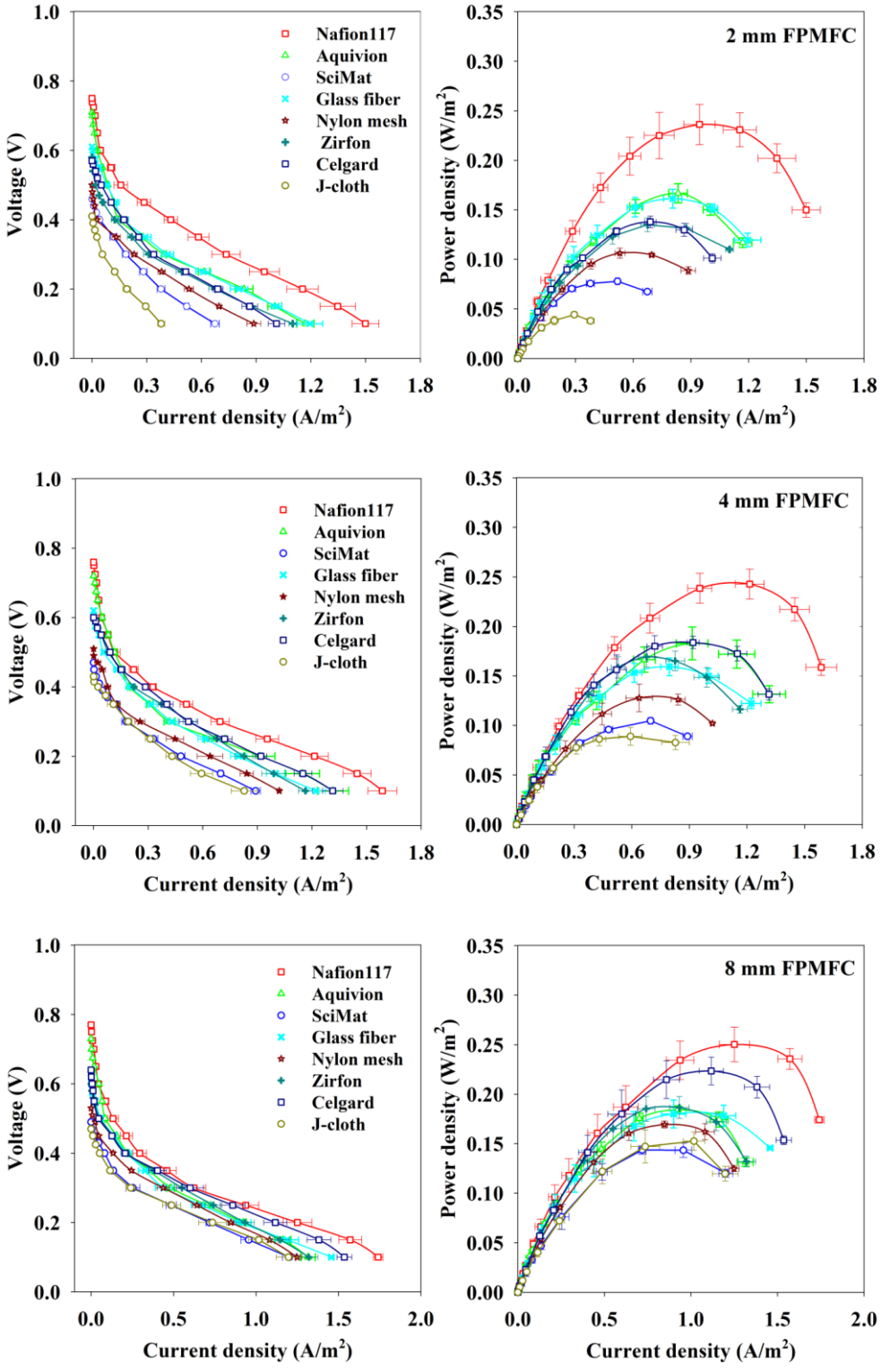

Figure 6-11 Polarization and power density curves of the 2 mm, 4 mm, and 8 mm FPMFCs with different separators. Error bars represent the standard deviation between three experiments.

The wastewater treatment efficiency, on the other hand, slightly decreased as the electrode spacing increased. This was because a larger portion of the wastewater bypassed the 3D anode at larger electrode spacing. Also, the treatment efficiency increased as separators with larger pores were used. The high crossover of oxygen could be contributing to the degradation of ethanol by the communities using oxygen as the final electron acceptor. The high crossover of ethanol, on the other hand, could result in direct ethanol oxidation at the cathode, and hence improve the overall treatment efficiency.

When the separators were examined in terms of the peak power density and CE, it was observed that those two parameters were linearly related (Figure 6-12), showing that the power output was mainly affected by the oxygen and fuel crossover. This was in contrast with the trend reported by Zhang et al. [31]. They observed a decrease in the CE (from 70% to 40%) as the power density increased (from 0.5 W/m^2 to 1 W/m^2) in a passive air-breathing MFC with the cathode placed 0.02 m apart from the anode. They indicated that the power output increased as separators with larger pores were used, which was due to the decreased Ohmic overpotential and the improved cathode performance. The CE, on the other hand, decreased as separators with larger pores were used due to the increased crossover.

The peak power density of the FPMFCs here decreased as separators with larger pores were used, which showed that the effect of the pH splitting was less significant than the crossover. The much smaller electrode spacing applied here, increased the concentration of oxygen at the anode, resulting in a significant decrease in the peak power density and the CE. The extent of the fuel crossover likely did not vary significantly with the electrode spacing in the FPMFCs while the CE and the peak power density increased as the electrode spacing increased.

Therefore, it could be concluded that the oxygen crossover was playing a more important role on the FPMFC performance than the fuel crossover and the proton transport number of the separator.

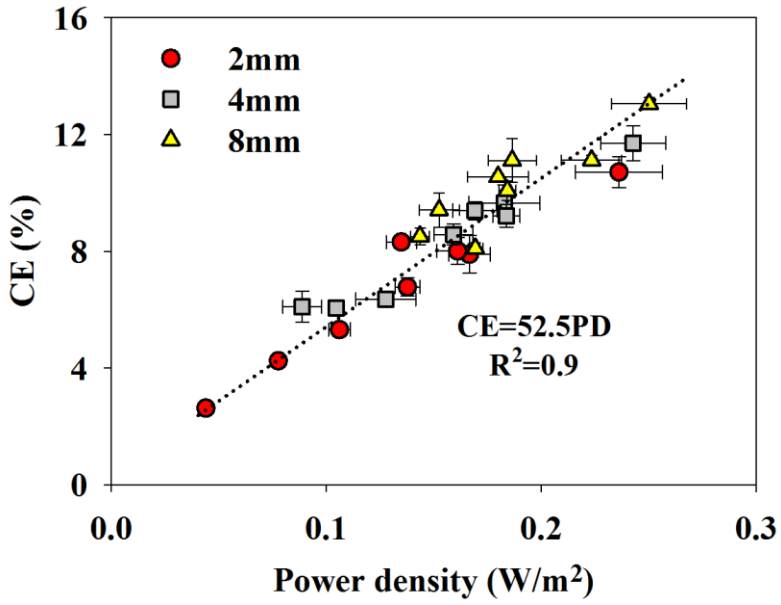

Figure 6-12 Coulombic efficiency (CE) versus peak power density (PD) with different separators in the 2 mm, 4 mm, and 8 mm FPMFCs. Error bars represent the standard deviation between three experiments.

6.3.2.2 (bio)fouling of the separators

Scanning electron microscopy images from the anode-facing side of the separators from all three FPMFCs indicated significant biofilm growth on the surface of the separators, after 4 weeks of operation, except for the Nylon mesh filter. In the diaphragms with pore sizes smaller than 10^{-6} m (1 µm), the pores seemed to be clogged, while in the coarse-pore diaphragms, more

open areas were observed. The biofilm growth was also observed on the cathode surface, when using diaphragms.

Nylon mesh, on the other hand, showed significant biofilm growth on the cathode, developing through the filter pores. This indicated that the hydrophobicity of the Nylon material was not in favor of the bacterial growth on the surface of the separator. Figure 6-13 shows the SEM images from the surface of the (bio)fouled (used) separators.

The FPMFCs were operated for 4 weeks, with no significant variation in the power output, indicating that the biofilm on the separator was not thick enough to affect the performance. The biofilm development on the separator matrix in the long-term, however, can act as a barrier and decrease the ion transfer which could result in a performance degradation. Nonetheless, the biofilm can also act as a barrier to oxygen transfer towards the anaerobic anode which could result in an increased CE [44, 109, 123].

Overall, the biofilm growth on the separator matrix could likely be in favor of the performance of the passive air-breathing FPMFC, especially when using micro-porous hydrophilic diaphragms. The biofilm development on the separator matrix can likely cover the open areas short after the operation starts, and block the oxygen diffusing through the air cathode. The separator material should therefore be non-biodegradable.

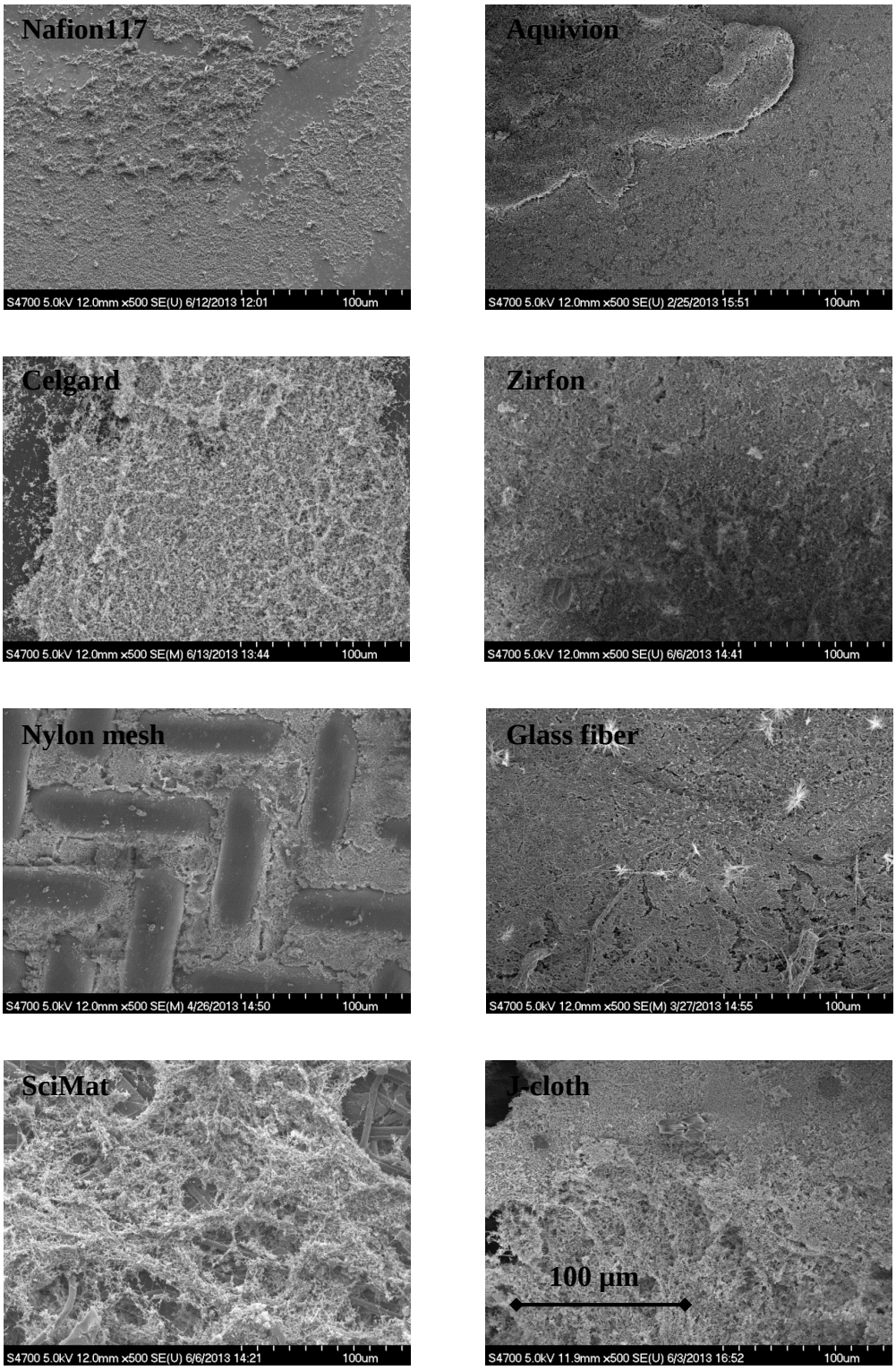

Figure 6-13 SEM images from the surface of the (bio)fouled (used) separators

6.4 Conclusions

The ionic resistivity, oxygen mass transfer and diffusion coefficients, and proton transport number were investigated in a non-inoculated passive air-breathing setup while the mass transfer and diffusion coefficients of ethanol and acetate were investigated in a non-inoculated aqueous setup, as the critical characteristics affecting the performance of the passive air-breathing FPMFCs. The separators were then evaluated in three inoculated passive air-breathing FPMFCs with different electrode spacing (ca. 0.5×10^{-3} m, 2.5×10^{-3} m, 6.5×10^{-3} m).

The pore size and thickness of the separators played key roles on the oxygen and fuel crossover, and the resistivity of the separators. The crossover increased as separators with larger pores were tested. The resistivity, on the other hand, increased as the thickness increased and/or the pore sized decreased, resulting in a poor ionic conductivity. The proton transport number of the separators was in the range of 0.59-0.92, corresponding to a maximum cathodic pH elevation to ca. 11 in absence of a PBS.

The oxygen and fuel crossover played critical roles on current generation in the FPMFCs with small electrode spacing. The peak power density and CE decreased when separators with higher crossover were used at the smallest electrode spacing applied. As the electrode spacing increased, the sensitivity of the peak power to the crossover decreased, and the peak power density and CE both increased. Nafion®117 produced the highest peak power density in all three FPMFCs. Celgard® produced a peak power density of ca. 0.22 W/m^2 in the 8 mm FPMFC, close to that produced using Nafion®117 (ca. 0.25 W/m^2).

Chapter 7: Modeling and simulation of the FPMFC

7.1 Introduction

Similar to chemical fuel cells, MFC research has become interested in numerical modeling to facilitate the process design and optimization. The MFC models developed so far have mainly focused on describing the anodic biofilm and its role on the performance of the MFCs [124–126]. The numerical modeling of the MFC can also be a valuable tool to elucidate the role that the separator is playing on the overall performance as well as to optimize the MFC configuration (i.e., the electrode spacing). This is also beneficial because investigating the MFC performance experimentally with different separators can be time consuming and expensive.

Overall, numerical modeling of the MFC targeting the role of the separator can provide useful insight into the design of appropriate separators applicable to a specific MFC configuration. Numerical modeling can be further used to optimize the power output and the cost of the MFC based on the interactions between the electrode spacing and the separator characteristics (or type). In this chapter, a numerical model is developed based on the mixed potential theory. The numerical model is developed applying the FPMFC engineering and operation performance data as well as the investigated separator characteristics to estimate the kinetic parameters of the bio-electrochemical system, the anodic and cathodic electrode potentials/mixed potentials. In addition, the developed numerical model is used to investigate the sensitivity of the power output to the separator characteristics and the electrode spacing.

7.2 Methods

7.2.1 Model development based on the mixed potential theory

The proposed model focuses on the mixed potential theory using voltage and the charge balance, and mass and charge transfer limitations on the current generation. A schematic of the charge transfer as well as the crossover paths is presented in Figure 7-1. The mixed potentials at the anode are shown as the anode depolarization happening mainly due to the oxygen crossing from the cathode, the separator, the electrolyte (wastewater), and the biofilm. The mixed potentials at the cathode are shown as the cathode depolarization happening mainly due to the ethanol crossing from the separator.

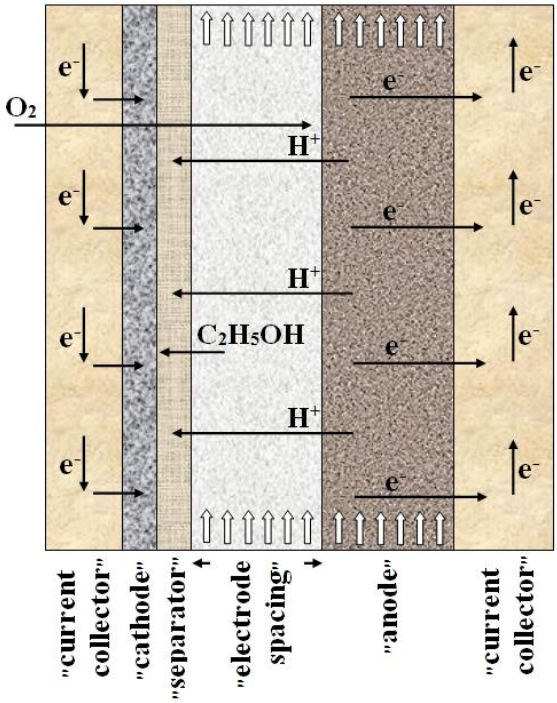

Figure 7-1 Schematic of a passive air-breathing FPMFC utilizing ethanol at the anode and oxygen at the cathode

The following assumptions were made in the FPMFC modeling:

- To simplify the model, the MFC system was assumed to be similar to a chemical fuel cell, hence no terms were added to represent the growth and death rate of the microbial communities, the biomass generation, and the biofilm growth on the cathode, and the separator.

- The anode electrode was assumed to be fully covered by the bacteria. Hence, the ethanol oxidation (the principle) and oxygen reduction (the side) reactions were catalyzed by the biofilm, and did not take place on the naked electrode.

- Flow of ions through the biofilm was assumed not to be limiting the electro-neutrality of the system, and the Ohmic overpotential was assumed to be due to the resistance towards the ion transfer between the surface of the anode and the cathode.

- Although acetate was detected as a by-product of ethanol degradation, for further simplification of the model, complete ethanol oxidation to protons and CO_2 and the oxygen reduction were assumed to be the sole anodic and cathodic reactions occurring in the MFC.

- Ethanol oxidation and oxygen reduction within the biofilm were assumed to contribute to anode polarization/depolarization. Hence, these reactions within the biofilm were assumed to be fully electrochemical.

- The temperature and pressure variations within the anode and the cathode chambers were assumed to be negligible, hence the reactions were considered isothermal and isobaric (303 K and 1 bar [abs]).

- The electrolyte was assumed to be stagnant[15], thus no effect of the electrolyte flow on the concentration profile was considered.

- The fuel (ethanol) was assumed to be well-distributed within the 3D electrode, thus the concentration profile was neglected.

- The anode was assumed to be well-buffered, hence no local pH drop within the biofilm was considered.

- Due to the electro-activity of the 99% of the thickness of the 3D electrode, calculated in Chapter 5, a uniform current and voltage distribution within the 3D electrode was assumed.

Complete ethanol (EtOH) oxidation at the anode yields a 12-electron transfer reaction:

$$C_2H_5OH + 3H_2O \rightarrow 12e^- + 12H^+ + 2CO_2 \qquad \text{Eq.7- 1}$$

The equilibrium potential for this reaction at the anode and the cathode can be calculated as follows[16]:

[15] This is due to the low flow-rate of the synthetic wastewater which results in a small upwards velocity.

[16] The superscripts of a and c refer to the anodic and cathodic parameters, respectively.

$$E^{a}_{EtOH} = E^{0}_{EtOH} - \frac{R.T}{n_{EtOH}.F}\ln\left(\frac{C^{a}_{EtOH}}{P^{a}_{CO_2}[H^{+}]_a{}^{n_{EtOH}}}\right) \quad \text{Eq.7- 2}$$

$$E^{c}_{EtOH} = E^{0}_{EtOH} - \frac{R.T}{n_{EtOH}.F}\ln\left(\frac{C^{c}_{EtOH}}{P^{c}_{CO_2}[H^{+}]_c{}^{n_{EtOH}}}\right) \quad \text{Eq.7- 3}$$

where E^{0}_{EtOH} is the standard half-cell potential (V vs. SHE) of the ethanol oxidation reaction at 298 K and 1 bar (abs), R is the universal gas constant (J/mol/K), T is the temperature (K), n_{EtOH} is the number of electrons transferred during the complete ethanol oxidation, F is the Faraday constant (C/mol), C^{a}_{EtOH} and C^{c}_{EtOH} are the concentration of ethanol (M) at the anode and the cathode, respectively, $P^{a}_{CO_2}$ and $P^{c}_{CO_2}$ are the partial pressure of carbon dioxide (bar) at the anode and the cathode (assumed to be 1 bar), respectively, and $[H^{+}]_a$ and $[H^{+}]_c$ are the concentration of protons (M) at the anode and the cathode, respectively. The oxygen reduction reaction is a 4-electron transfer reaction and in neutral and alkaline solutions is represented by:

$$O_2 + 4e^{-} + 2H_2O \rightarrow 4OH^{-} \quad \text{Eq.7- 4}$$

The equilibrium potential for this reaction at the anode and the cathode can be calculated as follows:

$$E^{a}_{O_2} = E^{0}_{O_2} - \frac{R.T}{n_{O_2}.F}\ln\left(\frac{[OH^{-}]_a{}^{n_{O_2}}}{C^{a}_{O_2}}\right) \quad \text{Eq.7- 5}$$

$$E^{c}_{O_2} = E^{0}_{O_2} - \frac{R.T}{n_{O_2}.F}\ln\left(\frac{[OH^{-}]_c{}^{n_{O_2}}}{P_{O_2}}\right) \quad \text{Eq.7- 6}$$

where $E^{0}_{O_2}$ is the standard half-cell potential (V vs. SHE) of the oxygen reduction reaction at 298 K and 1 bar (abs), n_{O_2} is the number of the electrons transferred during the oxygen

reduction, $C^{a}_{O_2}$ and P_{O_2} are the concentration (M) and partial pressure (atm) of oxygen at the anode and the cathode, respectively, and $[OH^-]_a$ and $[OH^-]_c$ are the concentration of hydroxyls (M) at the anode and the cathode, respectively. The overall FPMFC voltage balance can be written as:

$$E_{cell} = E_c - E_a - E_{Ohm} \quad \text{Eq.7- 7}$$

where E_c and E_a are the cathode and the anode operating potentials, respectively, and E_{Ohm} is the Ohmic overpotential. The anodic and the cathodic overpotentials due to each reaction and the Ohmic overpotential can be calculated using the following equations:

$$\eta^{a}_{EtOH} = E_a - E^{a}_{EtOH} \quad \text{Eq.7- 8}$$

$$\eta^{a}_{O_2} = E_a - E^{a}_{O_2} \quad \text{Eq.7- 9}$$

$$\eta^{c}_{EtOH} = E_c - E^{c}_{EtOH} \quad \text{Eq.7- 10}$$

$$\eta^{c}_{O_2} = E_c - E^{c}_{O_2} \quad \text{Eq.7- 11}$$

$$E_{ohm} = J(R_S + \frac{d}{\kappa_E}) \quad \text{Eq.7- 12}$$

where η^{a}_{EtOH} and η^{c}_{EtOH} are the anodic and the cathode overpotentials (V) of the ethanol oxidation reaction, $\eta^{a}_{O_2}$ and $\eta^{a}_{O_2}$ are the anodic and the cathodic overpotentials (V) of the oxygen reduction reaction, R_S is the ionic resistivity of the separator ($\Omega.m^2$), d is the electrode spacing of the FPMFC (m), κ_E is the ionic conductivity of the electrolyte (S/m), and J is the current density (A/m^2) which can be calculated as follows:

$$J = J^{a}_{EtOH} - J^{a}_{O_2} = J^{c}_{O_2} - J^{c}_{EtOH} \quad \text{Eq.7- 13}$$

$$\frac{1}{J^{a}_{EtOH}} = \frac{1}{J^{amt}_{EtOH}} + \frac{1}{J^{act}_{EtOH}} \quad \text{Eq.7- 14}$$

$$\frac{1}{J^{a}_{O_2}} = \frac{1}{J^{amt}_{O_2}} + \frac{1}{J^{act}_{O_2}} \quad \text{Eq.7- 15}$$

$$\frac{1}{J^{c}_{O_2}} = \frac{1}{J^{cmt}_{O_2}} + \frac{1}{J^{cct}_{O_2}} \quad \text{Eq.7- 16}$$

$$\frac{1}{J^{c}_{EtOH}} = \frac{1}{J^{cmt}_{EtOH}} + \frac{1}{J^{cct}_{EtOH}} \quad \text{Eq.7- 17}$$

where amt and cmt refer to the anodic and cathodic mass transfer controlled (limiting) current densities, and act and cct refer to the anodic and cathodic charge transfer (kinetic) controlled current densities, respectively, and J^{a}_{EtOH}, $J^{a}_{O_2}$, J^{c}_{EtOH}, and $J^{c}_{O_2}$ are the current densities (A/m^2) of ethanol oxidation and oxygen reduction at the anode and the cathode, respectively. Eq. 7- 13 indicates that anodic and the cathodic current densities must be equal. The mass transfer controlled current densities for ethanol oxidation and oxygen reduction at the anode and the cathode can be calculated using Eq.7-18 through Eq.7-21:

$$J^{amt}_{EtOH} = n_{EtOH} F K^{a}_{EtOH} C_{EtOH} \quad \text{Eq.7- 18}$$

$$J^{cmt}_{EtOH} = n_{EtOH} F K^{c}_{EtOH} C_{EtOH} \quad \text{Eq.7- 19}$$

$$J^{amt}_{O_2} = n_{O_2} F K^{a}_{O_2} C_{O_2} \quad \text{Eq.7- 20}$$

$$J^{cmt}_{O_2} = n_{O_2} F K^{c}_{O_2} C_{O_2} \quad \text{Eq.7- 21}$$

where K^{a}_{EtOH}, $K^{a}_{O_2}$, K^{c}_{EtOH}, and $K^{c}_{O_2}$ are the effective mass transfer coefficients (m/s) at the anode side and at the cathode side of ethanol and oxygen, respectively, and can be calculated using Eq.7-22 through Eq.7-25:

$$\frac{1}{K^{a}_{EtOH}} = \frac{1}{K^{B}_{EtOH}} \quad \text{Eq.7- 22}$$

$$\frac{1}{K^{a}_{O_2}} = \frac{1}{K^{B}_{O_2}} + \frac{d}{D^{E}_{O_2}} + \frac{Y}{D_{O_2}} + \frac{1}{K^{C}_{O_2}} \quad \text{Eq.7- 23}$$

$$\frac{1}{K^{c}_{EtOH}} = \frac{Y}{D_{EtOH}} \quad \text{Eq.7- 24}$$

$$\frac{1}{K^{c}_{O_2}} = \frac{1}{K^{C}_{O_2}} \quad \text{Eq.7- 25}$$

where K^{B}_{EtOH} and $K^{B}_{O_2}$ the mass transfer coefficients (m/s) of are ethanol and oxygen in the biofilm, $D^{E}_{O_2}$ is the diffusion coefficient (m^2/s) of oxygen in the electrolyte, D_{O_2} and D_{EtOH} are the diffusion coefficients (m^2/s) of oxygen and ethanol in the separator, $K^{C}_{O_2}$ is the mass transfer coefficient (m/s) of oxygen in the cathode, d is the electrode spacing (m), and Y is the separator thickness (m). The charge transfer (kinetic) controlled current densities for the ethanol oxidation and oxygen reduction reactions at the anode and the cathode are calculated using the Erdey-Gruz-Volmer-Butler equation:

$$J^{act}_{EtOH} = j^{0}_{B_{EtOH}} \left[\exp\left[\frac{\alpha_{A^{A}_{EtOH}} n_{EtOH} F (E_a - E^{a}_{EtOH})}{RT} \right] - \exp\left[\frac{-(1-\alpha_{A^{A}_{EtOH}}) n_{EtOH} F (E_a - E^{a}_{EtOH})}{RT} \right] \right]$$

Eq.7- 26

$$J_{EtOH}^{cct} = j_{EtOH}^{0}\left[\exp\left[\frac{\alpha_{A_{EtOH}}^{C} n_{EtOH} F\left(E_c - E_{EtOH}^{c}\right)}{RT}\right] - \exp\left[\frac{-(1-\alpha_{A_{EtOH}}^{C}) n_{EtOH} F\left(E_c - E_{EtOH}^{c}\right)}{RT}\right]\right]$$

Eq.7- 27

$$J_{O_2}^{act} = j_{B_{O_2}}^{0}\left[\exp\left[\frac{(1-\alpha_{C_{O_2}}^{A}) n_{O_2} F\left(E_a - E_{O_2}^{a}\right)}{RT}\right] - \exp\left[\frac{-\alpha_{C_{O_2}}^{A} n_{EtOH} F\left(E_a - E_{O_2}^{a}\right)}{RT}\right]\right]$$

Eq.7- 28

$$J_{O_2}^{cct} = j_{O_2}^{0}\left[\exp\left[\frac{(1-\alpha_{C_{O_2}}^{C}) n_{O_2} F\left(E_c - E_{O_2}^{c}\right)}{RT}\right] - \exp\left[\frac{-\alpha_{C_{O_2}}^{C} n_{O_2} F\left(E_c - E_{O_2}^{c}\right)}{RT}\right]\right]$$

Eq.7- 29

where $j_{B_{EtOH}}^{0}$ and $j_{B_{O_2}}^{0}$ are the exchange current densities (A/m^2) of ethanol oxidation and oxygen reduction in the biofilm, j_{EtOH}^{0} and $j_{O_2}^{0}$ are the exchange current densities (A/m^2) of ethanol oxidation and oxygen reduction at the cathode, $\alpha_{A_{EtOH}}^{A}$ and $\alpha_{C_{O_2}}^{A}$ are the charge transfer coefficients of ethanol oxidation and oxygen reduction at the anode, and $\alpha_{A_{EtOH}}^{C}$ and $\alpha_{C_{O_2}}^{C}$ are the charge transfer coefficients of ethanol oxidation and oxygen reduction at the cathode. The average ethanol concentration within and alongside the anode electrode is estimated by calculating the logarithmic mean of the inlet and the outlet concentration using:

$$C_{EtOH} = \frac{C_{in} - C_{out}}{\ln C_{in} - \ln C_{out}}$$

Eq.7- 30

The pH of the cathode is estimated taking into account the proton transport number of the separator and calculating the protons concentration at the cathode during the current generation [75]:

$$pH = -\log\left(\frac{10^{-14}}{10^{(pH_{in}-14)}+(1-n_{H^+})\frac{10}{0.05.F}}\right) \quad \text{Eq.7- 31}$$

7.2.2 Parameter estimation

Table 7-1 presents the operating conditions, constants, and parameters of the experimental setup for the model system of Eq. 7-1 through Eq. 7-31. Table 7-2 lists the characteristics of the separators investigated previously in Chapter 6. The 8 model parameters listed in

Table 7-3 cannot be determined from the experimental data, hence are estimated through an iterative optimization algorithm using a sequential quadratic programming (SQP) method for solving the constrained non-linear optimization problem [127] using the experimental results reported in Table 6-3 (except for the J-cloth). These parameters are estimated by minimizing the summation of the square roots of the difference between the measured and the predicted current densities, minimizing an objective function defined as:

$$F_{obj} = \sum_{i=1}^{N}\sum_{j=1}^{M}\sum_{k=1}^{K}(J'_{i,j,k} - J_{i,j,k})^2 \quad \text{Eq.7- 32}$$

where N, M, and K represent the number of the separators, the data points, and the FPMFCs used for the optimization problem. Integration of model equations into the optimization problem is performed in MATLAB (The Mathworks Inc., Natick, MA, USA). The estimated parameters are then used to solve the model equations during the sensitivity analysis and

electrode potentials estimation. The characteristics data of one of the separators (J-cloth) are used for the model validation.

Table 7-1 Parameters of operation and the constants of the ethanol-air MFC model

Symbol	Definition	Value	Unit
R	Universal gas constant	8.314	J/mol/K
T	Temperature	303	K
F	Faraday constant	96485.3	C/mol
n_{EtOH}	Number of electrons transferred in ethanol full oxidation	12	-
n_{O_2}	Number of electrons transferred in oxygen full reduction	4	-
pH_{out}	Outlet pH	7	-
pH_{in}	Inlet pH	8.5	-
$j^0_{O_2}$	Exchange current density of oxygen reduction on Pt	0.015	A/m^2
j^0_{EtOH}	Exchange current density of ethanol oxidation on Pt	0.003	A/m^2
$K^c_{O_2}$	Mass transfer coefficient of oxygen in the air cathode	2.7×10^{-5}	m/s
$D^E_{O_2}$	Diffusion coefficient of oxygen in the electrolyte	2×10^{-9}	m^2/s
C_{in}	Ethanol concentration in the inlet stream	0.085	M
E^0_{EtOH}	Standard half-cell potential of ethanol oxidation at 298 K	0.084	V vs. SHE
$E^0_{O_2}$	Standard half-cell potential of oxygen reduction at 298 K	0.401	V vs. SHE
P_{O_2}	Partial pressure of oxygen in the air	0.21	Atm
C_{O_2}	Oxygen concentration at the cathode	8.3	mol/ m^3
κ_E	Ionic conductivity of the synthetic wastewater	0.5	S/m

Table 7-2 Characteristics of the separators measured in the non-inoculated setups. Error values represent the standard deviation between the measurements of three experiments.

Separator	Thickness ($\times 10^{-6}$ m)	k_O ($\times 10^{-6}$ m/s)	k_E ($\times 10^{-6}$ m/s)	R_S ($\times 10^{-4}$ Ω.m^2)	n_{H+}
Nafion®117	178	0.29±0.02	0.49±0.01	5.4±0.1	0.59±0.01
Aquivion®	30	0.77±0.05	0.98±0.01	0.8±0.1	0.72±0.01
Celgard®	200	1.20±0.06	0.84±0.01	4.4±0.2	0.92±0.01
Zirfon®	500	1.47±0.06	0.58±0.01	14±0.4	0.92±0.01
Nylon mesh	55	2.19±0.08	2.2±0.2	1.4±0.1	0.89±0.03
Glass fiber	380	0.87±0.06	1.02±0.05	7.8±0.2	0.62±0.02
SciMat®	144	2.6±0.1	1.93±0.08	3.1±0.1	0.66±0.03
J-cloth	300	9.5±0.6	33±3	6.2±0.2	0.78±0.02

7.3 Results and discussion

7.3.1 Parameters estimation and model validation

Table 7-3 lists the estimated kinetic and mass transfer parameters. The estimated exchange current densities in the biofilm were 0.36 A/m^2 and 0.40 A/m^2 for ethanol oxidation and oxygen reduction which were within the range of the values reported in the literature [128–132]. The charge transfer coefficients were estimated by assuming transfer of 2 electrons at the rate-determining step for both ethanol oxidation and oxygen reduction reactions. The estimated exchange current density and mass transfer coefficients in the biofilm suggested that ethanol

oxidation within the biofilm was kinetically controlled while oxygen reduction was limited by the oxygen diffusion through the separator towards the anaerobic anode.

Oxidation of ethanol and reduction of oxygen in the biofilm were assumed to happen at the biofilm-electrode interface, hence the mass transfer coefficients of ethanol and oxygen in the biofilm estimated by the model are virtual. This is because both ethanol and oxygen were being consumed within the biofilm. Also, the experimentally measured CE values of lower than 15% indicated that only up to ca. 15% of the ethanol content of wastewater degraded yielding electrical current and over 85% of the ethanol was consumed by the communities not using the anode as the final electron acceptor. This ethanol degradation was likely accompanied by oxygen reduction (up to 3 moles of oxygen per mole of ethanol), as the *methanogenic* activities were inhibited by addition of 2-bromoethanesulfonate.

Table 7-3 Estimated kinetic parameters of the ethanol-air passive air-breathing FPMFC

Parameter	Definition	Value	Unit
$j^{o}_{B_{O_2}}$	Exchange current density of oxygen reduction in the biofilm	0.36	A/m^2
$j^{o}_{B_{EtOH}}$	Exchange current density of ethanol reduction in the biofilm	0.40	A/m^2
$K^{B}_{O_2}$	Mass transfer coefficient of oxygen in the biofiom	2.7×10^{-6}	m/s
K^{B}_{EtOH}	Mass transfer coefficient of ethanol in the biofilm	9.3×10^{-6}	m/s
$\alpha_{A^{A}_{EtOH}}$	Anodic charge transfer coefficient of ethanol oxidation	7×10^{-2}	-
$\alpha_{C^{A}_{O_2}}$	Anodic charge transfer coefficient of oxygen reduction	0.24	-
$\alpha_{A^{C}_{EtOH}}$	Cathodic charge transfer coefficient of ethanol oxidation	3×10^{-3}	-
$\alpha_{C^{C}_{O_2}}$	Cathodic charge transfer coefficient of oxygen reduction	0.11	-

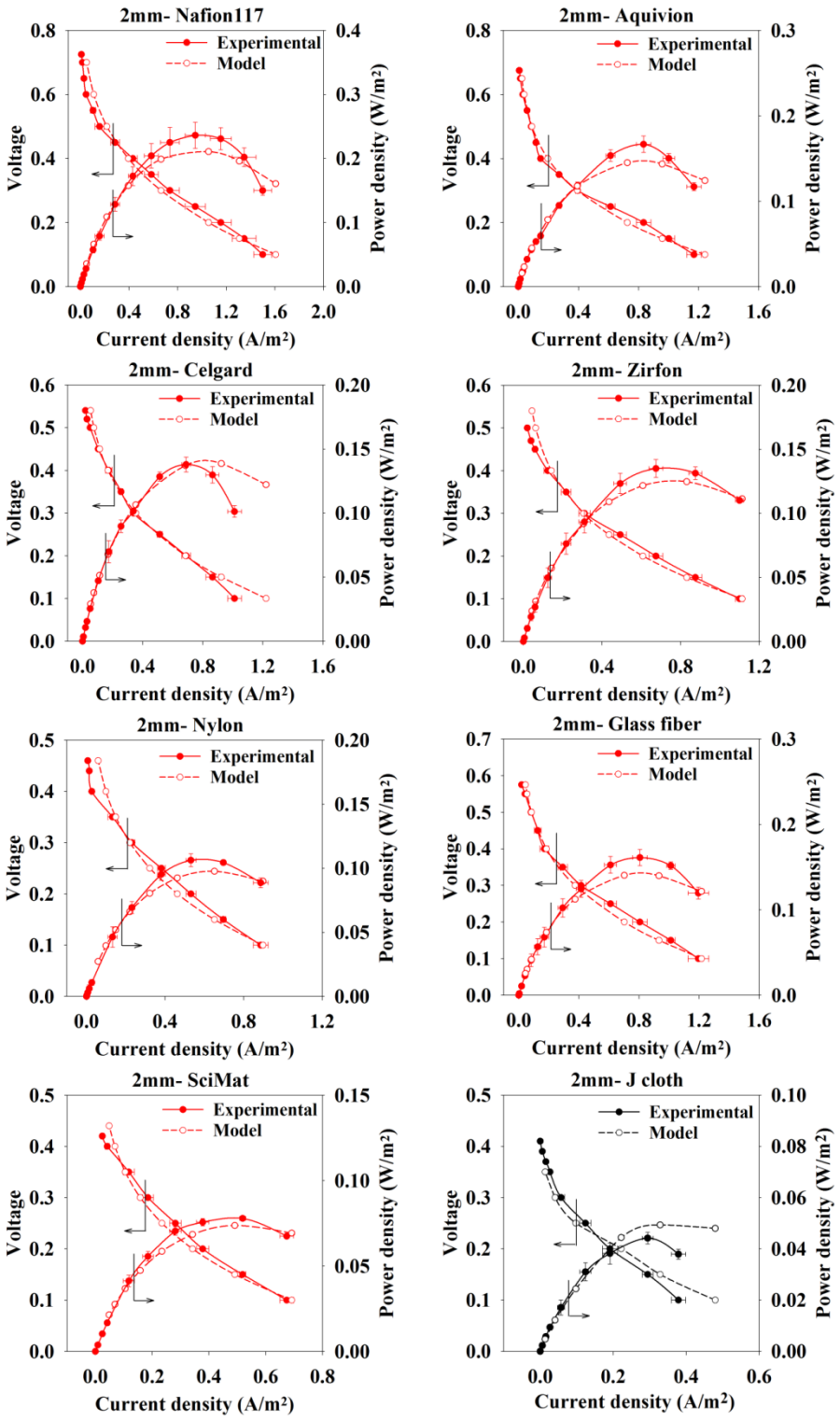

Figure 7-2 Polarization and power density curves predicted by the model, using different separators (red) and model validation (black) in the 2 mm FPMFC. Error bars represent the standard deviation between three experiments done in chapter 6.

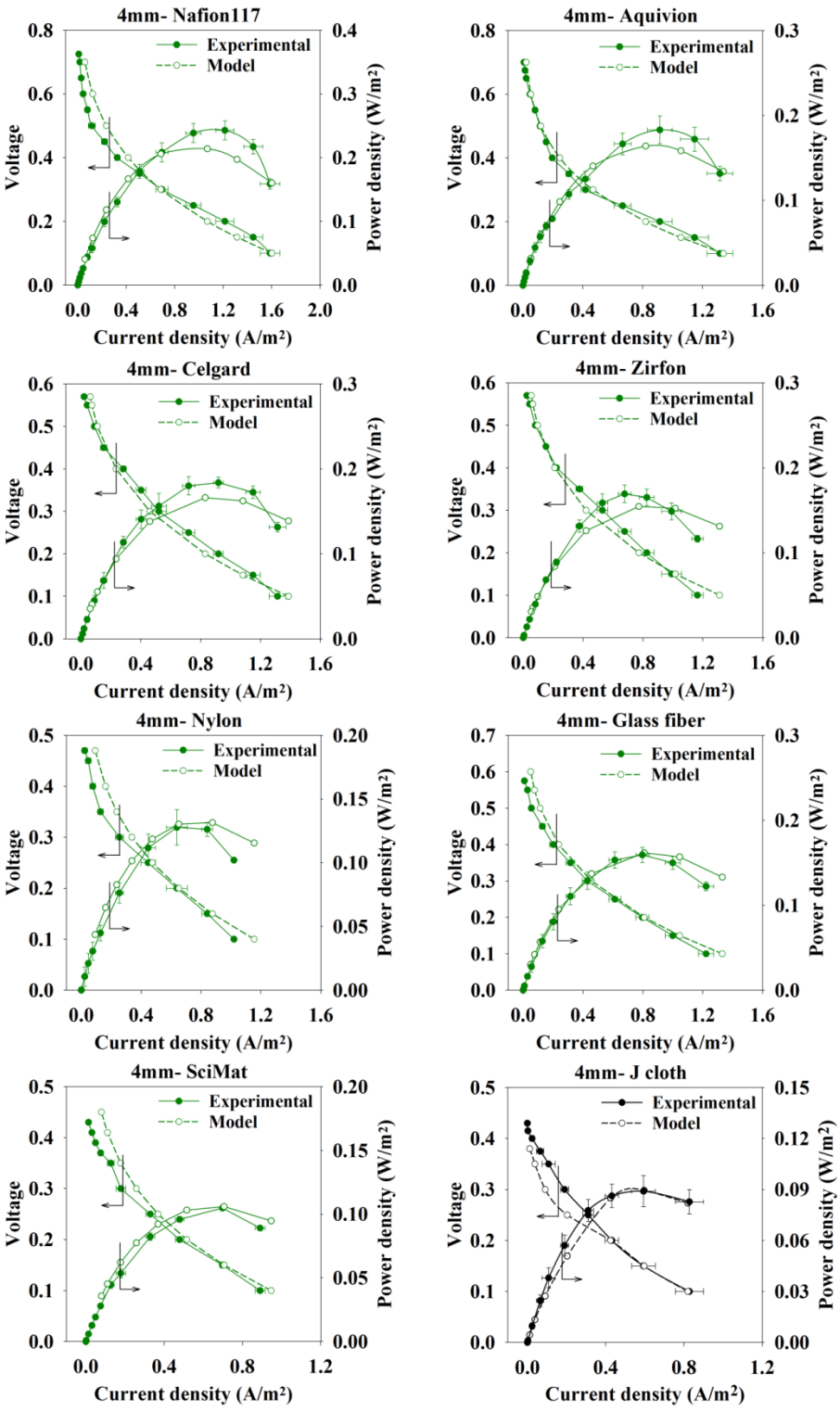

Figure 7-3 Polarization and power density curves predicted by the model, using different separators (green) and model validation (black) in the 4 mm FPMFC. Error bars represent the standard deviation between three experiments done in chapter 6.

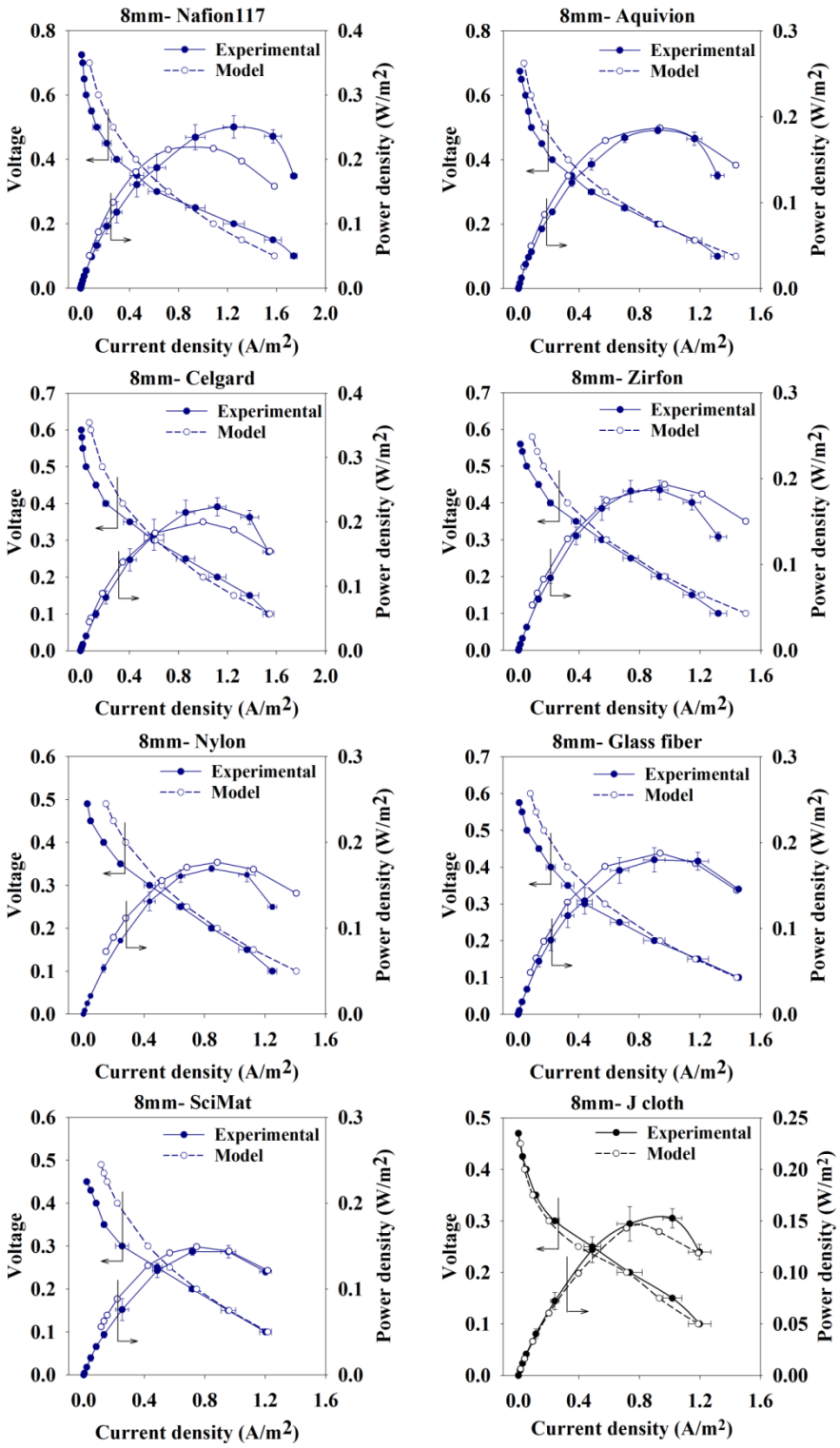

Figure 7-4 Polarization and power density curves predicted by the model, using different separators (blue) and model validation (black) in the 8 mm FPMFC. Error bars represent the standard deviation between three experiments done in chapter 6.

The average deviation of the predicted current density by the model from the measured current density values was 0.08 A/m^2. The model was further validated by solving the equations of the voltage and charge balance for the three FPMFCs using J-cloth (Figure 7-2, Figure 7-3, Figure 7-4 (black)).

The electrode potentials estimated by the model showed the critical role of the oxygen crossover on the anodic mixed potentials and the resulted anode depolarization. The oxygen crossover yielded a positive shift in the anode potential when the mass transfer coefficient of oxygen in the separators increased (Figure 7-5). In the 2 mm FPMFC, the anode depolarization increased more significantly as separators with larger coefficients were used. The effect of the oxygen crossover on the anode potential became less significant as the electrode spacing increased (in the 4 mm and 8 mm FPMFCs), due to decreased concentration of oxygen at the anode.

Nafion®117 gave the lowest anode potential values in all three FPMFCs (ca. -0.3 V vs. SHE at open circuit), similar to the values reported in the MFCs using ferricyanide and ferric iron as the oxidant [36, 133], as well as the passive air-breathing MFCs with electrode spacing of 0.02 m and larger [31, 80]. This indicated that the extent of the anode depolarization matched that reported for the passive air-breathing MFCs with larger electrode spacing, as a result of the lower susceptibility of the polymeric Nafion®117 membrane to oxygen diffusion. At the largest electrode spacing applied (ca. 6.5×10^{-3} m) in the 8 mm FPMFC, the applied diaphragms and the Aquivion® membrane indicated relatively similar anode depolarization. The estimated low anode depolarization by oxygen for the FPMFCs using Nafion®117 and Aquivion® could be an indicator that the low CEs of the FPMFCs using these membranes was due to the

oxidation of ethanol by the communities using electron acceptors other than oxygen (e.g., sulfate).

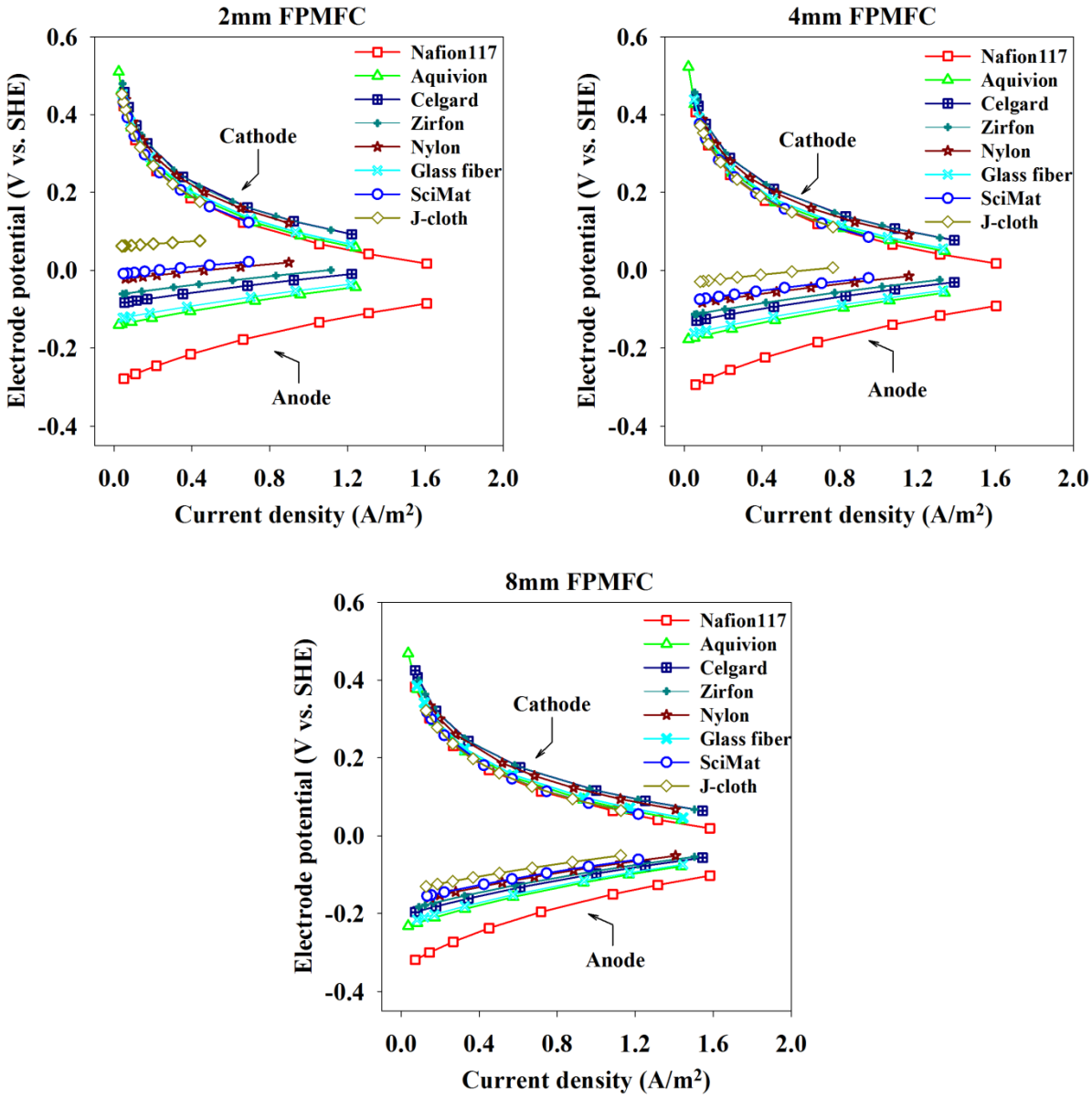

Figure 7-5 Estimated electrode potentials using different separators in the 2 mm, 4 mm, and 8 mm FPMFCs

The variation of the cathode potential using different separators was ca. 0.04 V in all three FPMFCs, as predicted previously in Chapter 6, attributed to the variation in the proton transport number of the selected separators. Ethanol oxidation at the cathode, on the other hand, was most likely limited by its slow kinetics; hence a possible variation in the extent of the ethanol crossover using different separators did not seem to be affecting the cathode activity, in the short-term. In reality, the permeability of the applied diaphragms to the electrolyte can likely improve the proton transport number of the diaphragms in the FPMFC environment, yielding more stable pH values at the cathode. In the long-term, however, it exposes the cathode to the synthetic wastewater as well as the suspended bacterial cells.

The estimated cathode potentials were similar at the open circuit to those reported for the ferrcyanide and ferric iron cathodes (ca. 0.5 V vs. SHE), followed by a substantial drop at the kinetic region (Figure 7-5), which resulted in lower values compared to the ferricyanide and ferric iron cathodes [36, 133] with the circuit connected. This was due to the sluggish kinetic of oxygen reduction over Pt [134–136], whereas a smaller kinetic overpotential has been reported for the ferricyanide and ferric iron cathodes. The mass transfer limitations and the resulted local oxygen starvation were also likely to decrease the air-breathing cathode performance.

7.3.2 Sensitivity analysis

7.3.2.1 Performance sensitivity to separator characteristics

A preliminary analysis was performed to investigate the sensitivity of the power output with respect to the separator characteristics, by changing one of the investigated separator

characteristics at a time while leaving the remaining unchanged, and solving the voltage and charge balance equations. The sensitivity analysis was performed for Nafion®117, as an insensitive separator to the electrode spacing and for J-cloth, as one of the most sensitive separators to the electrode spacing. Table 7-4and Table 7-5 present the percentage change in the peak power density in the FPMFCs when multiplying the separator characteristics by the indicated ratios, one at a time.

The sensitivity analysis results indicated that the power output of the passive air-breathing FPMFCs using Nafion®117 was more sensitive to the oxygen crossover compared to its other characteristics (Figure 7-6). Decreasing the oxygen crossover by 95% resulted in an increase by 49%, 45%, and 40% in peak power density of the 2 mm, 4 mm, and 8 mm FPMFCs, respectively. Hence, at a very low extent of oxygen crossover, the superficial peak power density was still relatively insensitive to a change in the electrode spacing. In addition, the increased peak power densities due to the decreased oxygen crossover suggested that even using Nafion®117, which was the least susceptible separator to oxygen, the performance was still being affected by the oxygen crossover.

Increasing the oxygen crossover by 100%, on the other hand, affected the peak power less significantly resulting in 25%, 19%, and 13% decrease in the peak power of the 2 mm, 4 mm, and 8 mm FPMFCs, respectively. The sensitivity of the peak power density to the electrode spacing, however, increased. A further increase in the oxygen crossover by 1000% decreased the peak power density by 70%, 54%, and 34% in the 2 mm, 4 mm, and 8 mm FPMFCs, respectively.

The proton transport number affected the peak power through affecting the cathode potential [28, 71]. A 60% increase in proton transport number of Nafion®117 (from 0.59 to 0.94) was estimated to increase the peak power similarly in all three FPMFCs by 23-24% (Figure 7-7). The same percentage of decrease in the proton transport number (from 0.59 to 0.24), on the other hand, slightly decreases the peak power (6-7%).

The peak power density did not indicate any sensitivity to the variation in neither the mass transfer coefficient of ethanol nor the ionic resistivity within the measured ranges. Ethanol oxidation on the cathode was controlled by its slow kinetics, thus a potential increase in the ethanol crossover did not reflect on the cathodic mixed potentials. Although the experimental results indicated that the performance was hindered when separators with greater ethanol crossover were used, the model showed that this performance drop was due to the increased oxygen crossover that came along with the increased ethanol crossover. The ionic resistivity, on the other hand, was an indicator of the Ohmic resistance of the separator which was small compared to the Ohmic resistance of the cell.

Table 7-4 Percentage change in the superficial peak power density of the 2 mm, 4 mm, and 8 mm FPMFCs with one at a time change of the characteristics of Nafion®117

Characteristics/Value	Ratio	Change in the superficial peak power density		
		2 mm	4 mm	8 mm
$\mathbf{k_O = 0.29\times10^{-6}}$ **m/s**	0.05	49%	45%	40%
	2	-25%	-19%	-13%
	11	-70%	-54%	-34%
$\mathbf{k_E = 0.49\times10^{-6}}$ **m/s**	0.05	0	0	0
	2	0	0	0
$\mathbf{n_{H^+} = 0.59}$	0.4	-7%	-7%	-6%
	1.6	24%	23%	23%
$\mathbf{R_S = 5.4\times10^{-4}\ \Omega.m^2}$	0.05	0	0	0
	2	0	0	0

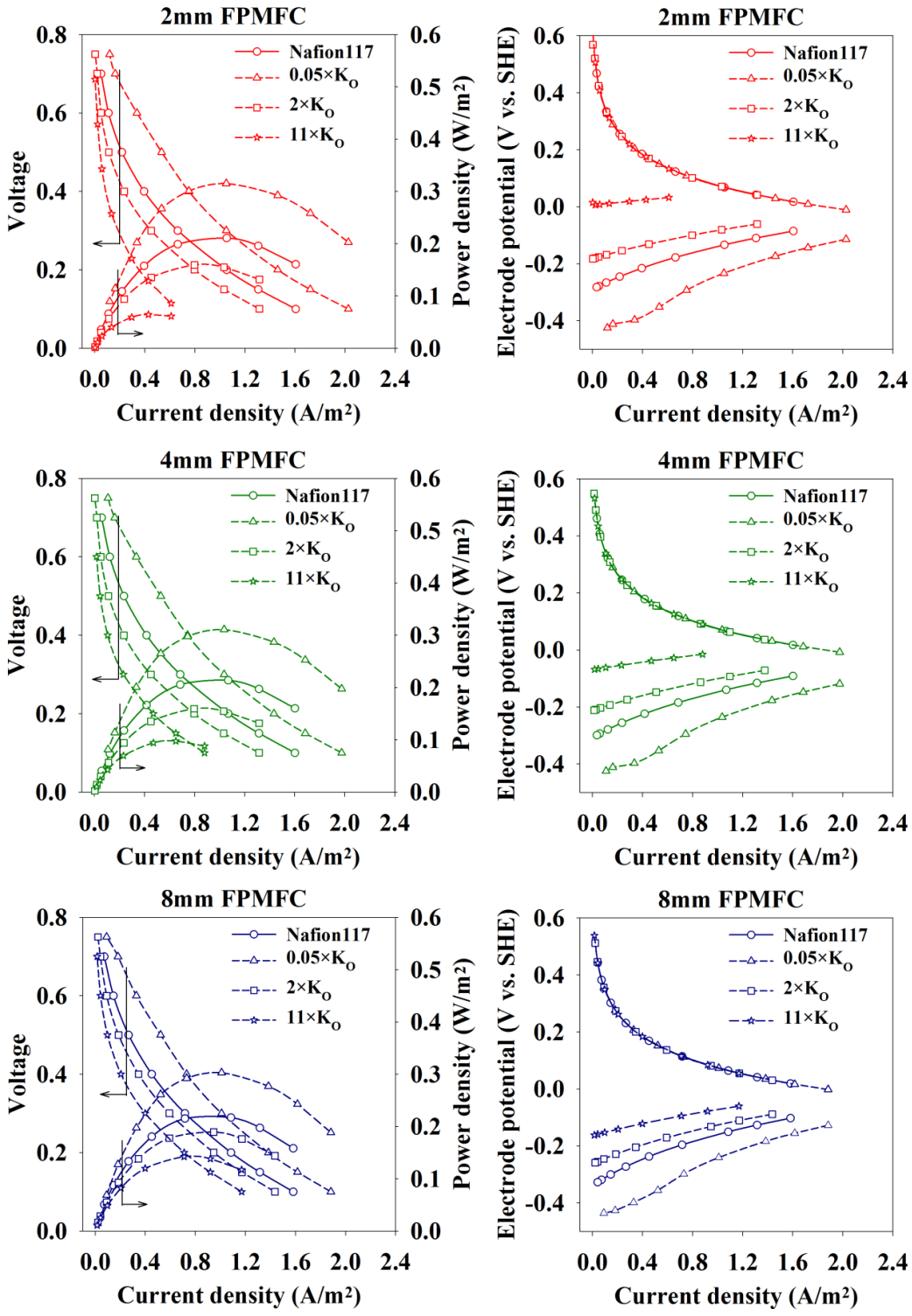

Figure 7-6 Sensitivity of the polarization and power density curves and electrode potentials to the oxygen crossover in Nafion®117

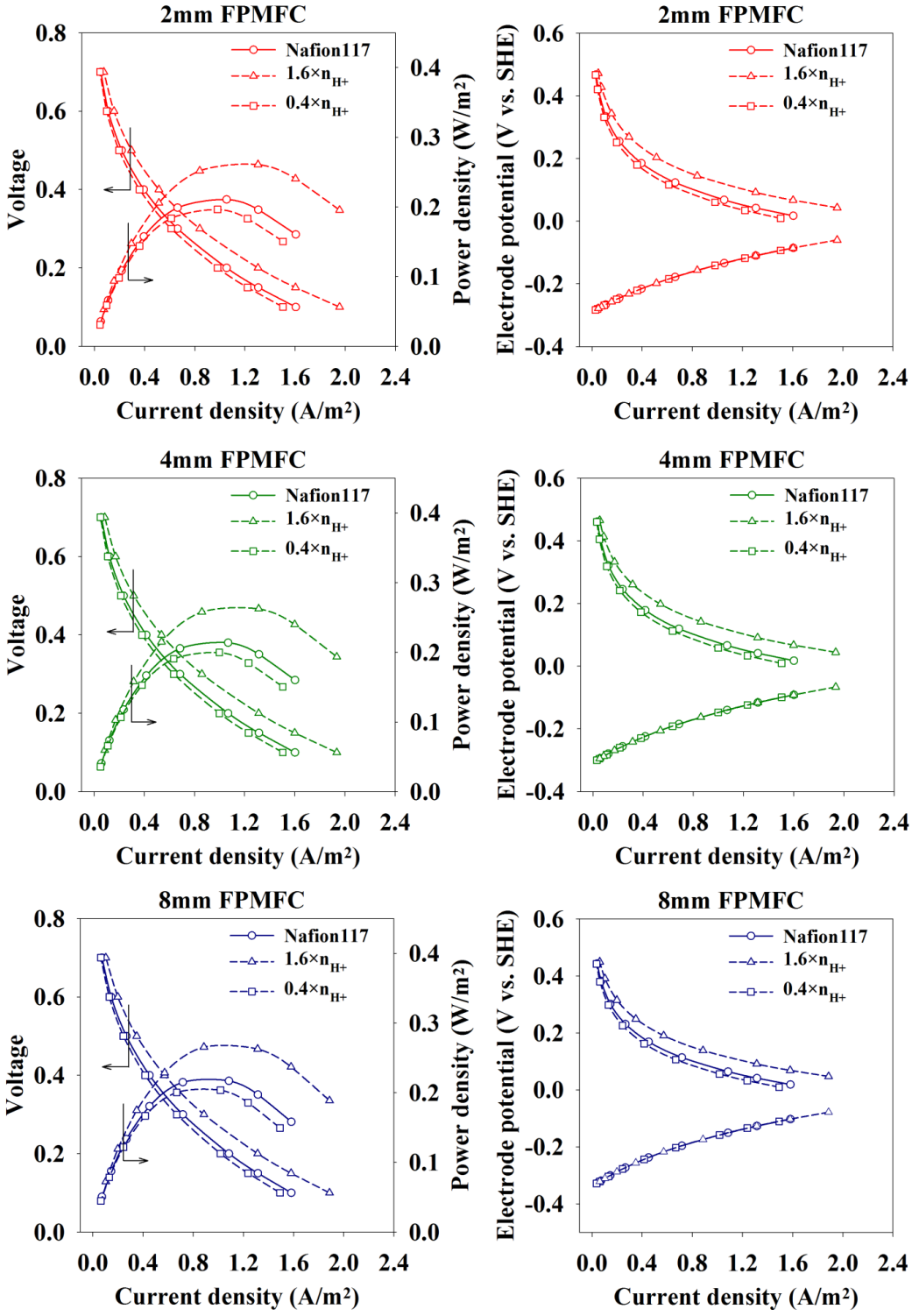

Figure 7-7 Sensitivity of the polarization and power density curves and electrode potentials to the proton transport number in Nafion®117

The sensitivity analysis using J-cloth characteristics indicated that the power output of the passive air-breathing FPMFCs were more sensitive to the mass transfer coefficient of oxygen (Figure 7-8) compared to Nafion®117. The sensitivity of the peak power density decreased as the electrode spacing increased, resulting in an increase of 286%, 121%, and 48% in the peak power density of the 2 mm, 4 mm, and 8 mm FPMFCs, respectively, when decreasing the oxygen crossover by 95%. The increase in the peak power density of the 2 mm FPMFC using J-cloth was ca. 6 times higher than that using Nafion®117, which was an indicator of the excessive flux of oxygen towards the anaerobic anode using J-cloth. The predicted electrode potentials also showed that all three FPMFCs were suffering from anodic mixed potentials.

The increase of the oxygen crossover by 100% decreased the peak power much less significantly resulting in less than 10% of a decrease in the peak power density. The 10% decrease in the peak power density with a 100% increase in the oxygen crossover using J-cloth was an interesting observation, indicating that a separator-free FPMFC would likely yield a slightly lower peak power density compared to that using J-cloth. This questions functionality of 1 layer of J-cloth in the passive air-breathing FPMFCs.

Similar to Nafion®117, a variation in the proton transport number of the J-cloth altered the peak power density through affecting the cathode potential [31, 80]. For example, a 20% increase in the proton transport number was estimated to increase the peak power density by 31%, 25%, and 20% in the FPMFCs (Figure 7-9). The same percentage of decrease in the proton transport number slightly decreased the peak power (less than 10%).

The peak power density was not sensitive to the variation in neither the mass transfer coefficient of ethanol nor the ionic resistivity within the measured ranges, due to the kinetically

controlled ethanol oxidation at the cathode as well as the overshadowing effect of the oxygen crossover. Ethanol crossover may not affect the peak power significantly, but it could result in cathodic biofilm development in the long-term.

Table 7-5 Percentage change in the superficial peak power density of the 2 mm, 4 mm, 8 mm FPMFCs with one at a time change of the characteristics of J-cloth

Characteristics/Value	Ratio	Change in the superficial peak power density		
		2 mm	4 mm	8 mm
$k_O = 9.5\times10^{-6}$ m/s	0.05	286%	121%	48%
	2	-10%	-5%	-2%
$k_E = 32.8\times10^{-6}$ m/s	0.05	0	0	0
	2	0	0	0
$n_{H+} = 0.78$	0.8	-10%	-9%	-8%
	1.2	31%	25%	20%
$R_S = 6.2\times10^{-4}$ Ω.m^2	0.05	0	0	0
	2	0	0	0

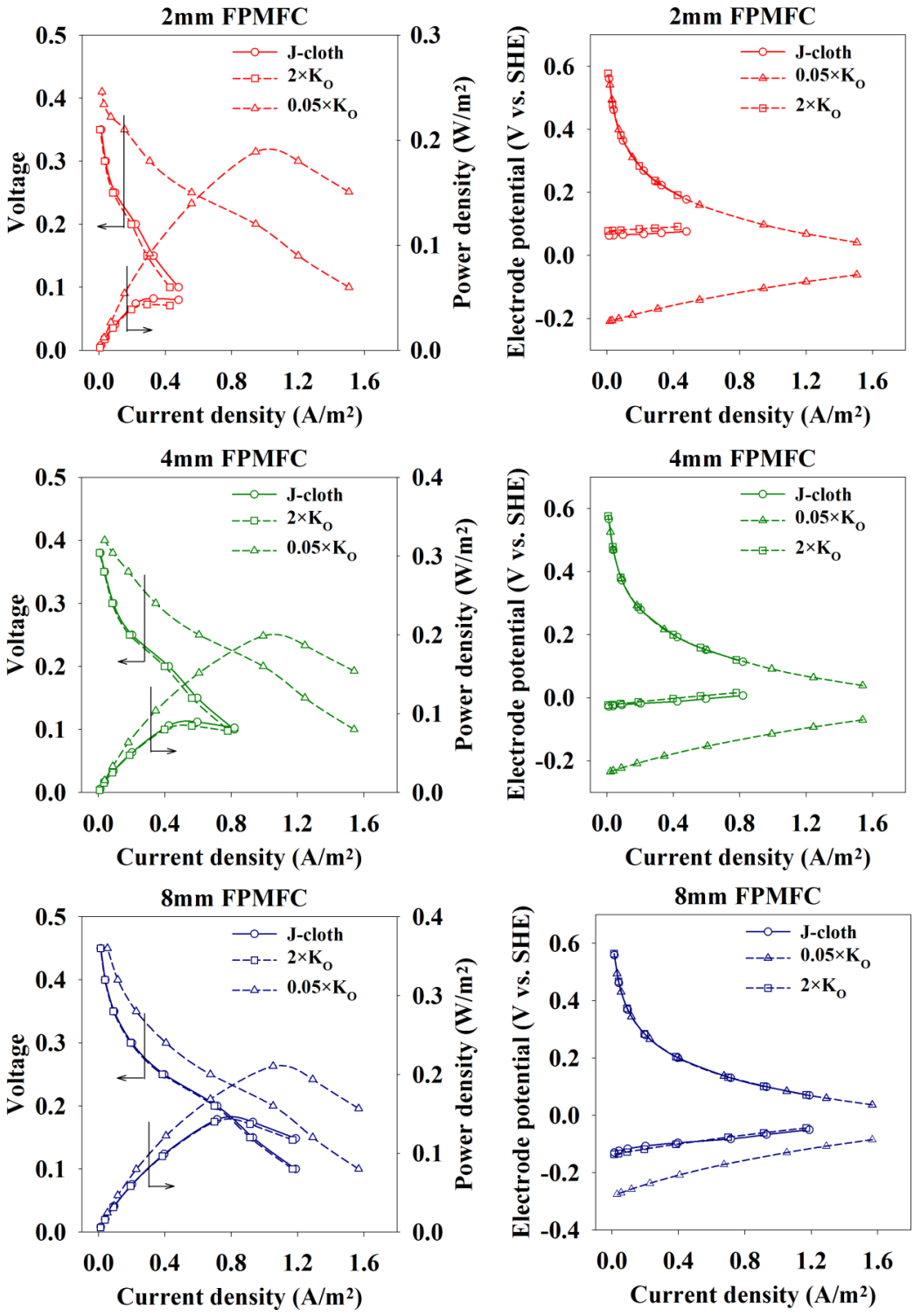

Figure 7-8 Sensitivity of the polarization and power density curves and the electrode potentials to the oxygen crossover in J-cloth

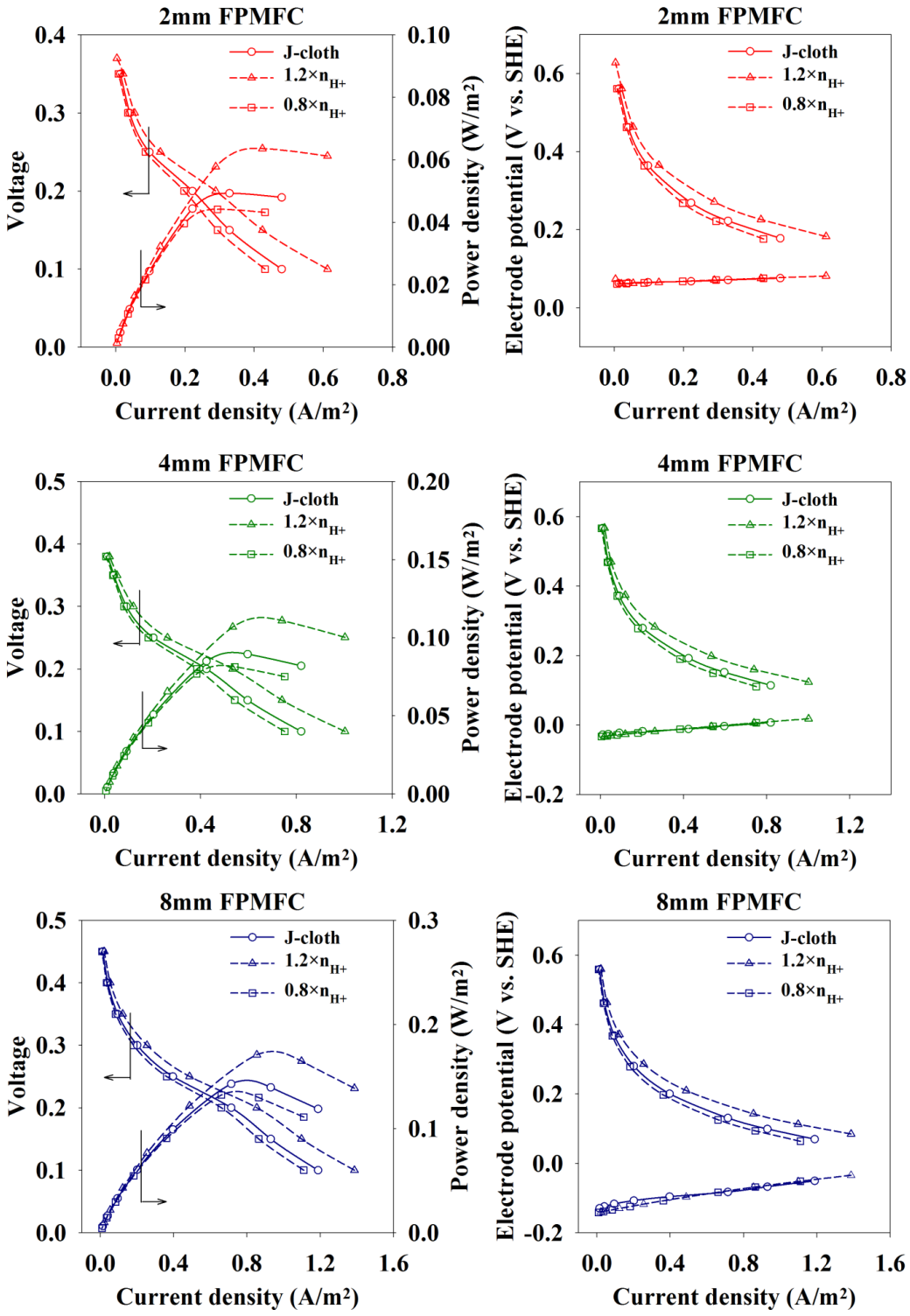

Figure 7-9 Sensitivity of the polarization and power density curves and the electrode potentials to the proton transport number in J-cloth

7.3.2.2 Performance sensitivity to electrode spacing

The electrode spacing was increased in the model to investigate the sensitivity of the superficial peak power density, using different separators. Increasing the electrode spacing up to 0.02 m using J-cloth increased the peak power density from 0.05 W/m^2 to 0.2 W/m^2, as a result of the decreased oxygen concentration at the anode (Figure 7-10). The decreased anodic mixed potentials likely alleviated the negative effect of the increased Ohmic overpotential that was attributed to the increased electrode spacing. The peak power density decreased at the electrode spacing larger than 0.02 m, where the Ohmic overpotential of the system became critical. The peak power density using Nafion®117 slightly increased as the electrode spacing increased, and similar to J-cloth, dropped at the electrode spacing of over 0.02 m.

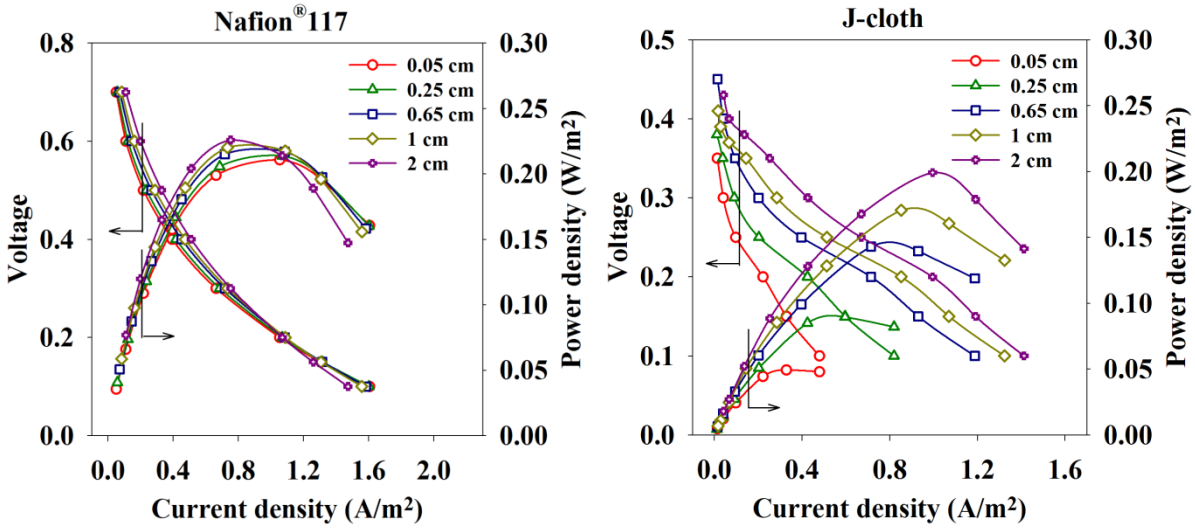

Figure 7-10 Sensitivity of the polarization and power density curves to the electrode spacing using Nafion®117 and J-cloth

As the electrode spacing increased, the effect of the oxygen crossover became less significant resulting in a more significant role played by the proton transport number of the separator. At the electrode spacing of 0.02 m, Celgard® and Zirfon® gave the highest peak power densities, as a result of their higher proton transport number (Figure 7-11). SciMat® and J-cloth, on the other hand, produced the lowest peak power densities showing that the oxygen crossover was still hindering the performance. Overall, it is concluded that the appropriate characteristics of the separator component for the passive air-breathing MFCs are dependent on the MFC configuration. Hence, while in the configuration with a small electrode spacing, the oxygen crossover can be critical for the sustainable power generation, in the configurations with larger electrode spacing, the pH splitting as well as the high Ohmic overpotential issues play a detrimental role on the performance.

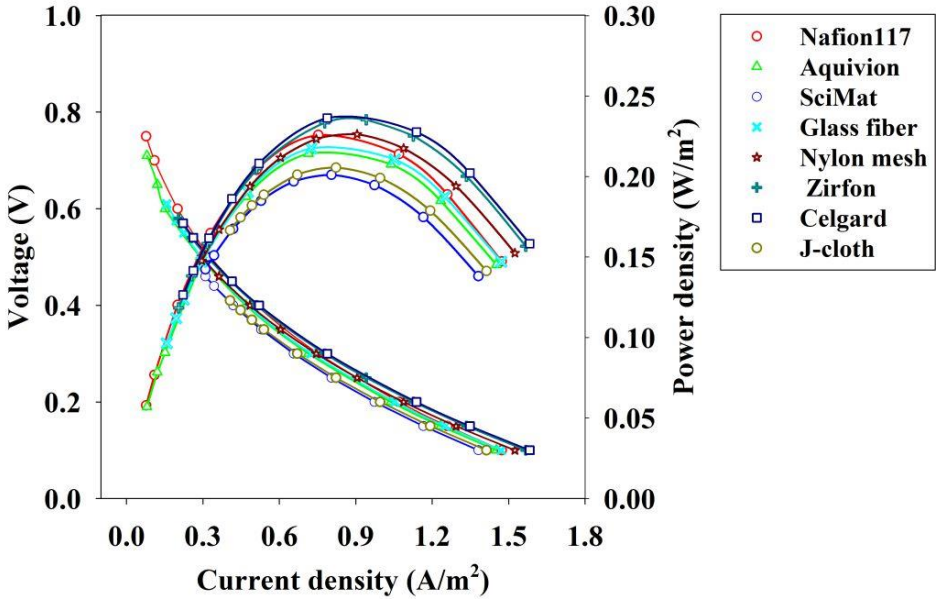

Figure 7-11 Predicted polarization and power density curves of an FPMFC with an electrode spacing of 0.02 m using the selected separators

7.4 Conclusions

A numerical model was developed to estimate the kinetic parameters of the bio-electrochemical system, predict the anodic and cathodic mixed potentials, and polarization and power density curves of the passive air-breathing FPMFCs using different separators. The principle anodic and cathodic reactions were predicted to be controlled purely by the slow kinetics. Thus, the mass transfer was not indicated to be an issue in the current generation. The oxygen crossover played a critical role on the anode performance, causing mixed potentials especially at the small electrode spacing. The significance of the oxygen crossover on the peak power density decreased as the electrode spacing increased. This was due to the decreased anodic mixed potentials. The performance was also affected by the proton transport number of the separator. The cathode potential increased as the proton transport number of the separator increased resulting in an increased peak power density.

The ethanol crossover and the separator ionic resistivity did not play significant roles on the performance, mainly due to the combined effect of the slow kinetics of ethanol oxidation at the cathode, the relatively high Ohmic overpotential of the synthetic wastewater used as the electrolyte, and the oxygen crossover overshadowing the effect of the resistivity. Although the power output was not sensitive to the ethanol crossover in the short-term, it could be affected in the long-term, when a biofilm is developed on the cathode. For the present cell configuration, increasing the electrode spacing beyond 0.02 m decreased the peak power density, due to the increased Ohmic overpotential, but below 0.02 m it increased the peak power density as a result of the decreased anodic mixed potentials.

Chapter 8: Economic considerations

8.1 Introduction

To be able to implement the MFCs into the current wastewater systems, it is critical to reduce the capital cost while increasing the power output so that this technology can be considered a viable alternative. Currently, PEMs and the Pt-based cathodes contribute to up to 90% of the capital cost of the MFCs in lab-scale setups (resulting in a capital cost of ca. $15/kg COD, Figure 8-1, [26]). At this stage, the capital cost of the MFCs can hardly compete with the AS (ca. $0.2/kg COD) and the AD (ca. $0.02/kg COD) processes (assuming a reactor lifetime of 25 years) [5, 137]. A major step in commercializing MFCs, therefore, seems to be the replacement of the currently used expensive polymeric membranes as well as the Pt-based cathodes with less expensive alternatives. In this section, a simple cost analysis was performed based on the cost of the FPMFC components and the performance data presented in previous chapters to evaluate the economic viability of the selected separators.

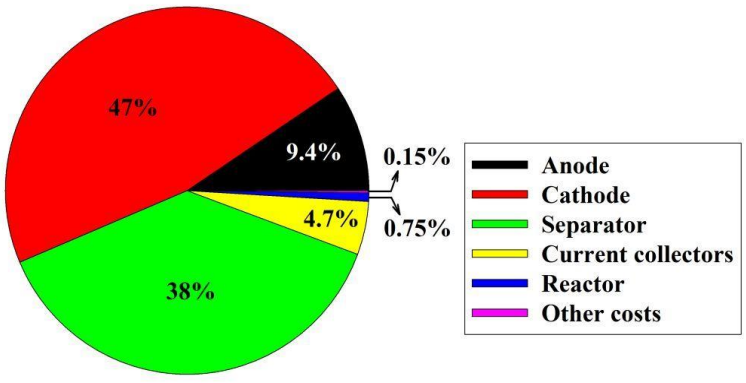

Figure 8-1 Contribution of each MFC component to the total capital cost, estimated based on the materials used in lab-scale setups [26]

8.2 Capital cost of the FPMFC

The cost of the separators as well as the cost of the other MFC components such as the Pt-based cathode, graphite felt anode, end plates, and current collectors are estimated based on the material used in the laboratory scale setup used in this research as well as some literature data (Table 8-1 and Table 8-2). The costs of the separators have been collected in some cases from the suppliers and in some other cases, from the literature, hence these are rough estimates.

A lifetime of 5 years is assumed for the MFC components such as the separator (except for J-cloth with a lifetime of 1 year), anode, cathode, and current collectors, with no significant performance degradation, whereas a longer lifetime (ca. 25 years) is considered for the MFC end plates. The annual costs of the MFC components are calculated based on the lifetime of the different components and an annual interest rate of 6% in a 25-year period.

The configuration of the MFC clearly determines the output power, and thus, the cost of the separator per unit power (Table 8-2). Because of the decreased oxygen concentration at the anode, increasing the anode chamber depth (from 2×10^{-3} m to 8×10^{-3} m) increases the power output and consequently decreases the separator cost per unit power. The removal efficiency, on the other hand, decreases as the anode chamber depth increases, since the portion of wastewater bypassing the anode increases.

Table 8-1 Annual cost of the MFC components estimated based on the lab-scale material, assuming a lifetime of 5 years for the anode, cathode, and current collectors, and 25 years for the end plates, with an interest rate of 6% over a 25-year period

Component	Cost	Source	Estimated annual cost
Graphite felt anode	200 $/m^2	This research	170 $/m^2
Pt-based cathode	500 $/m^2	This research	430 $/m^2
Current collectors	50 $/m^2	[26]	40 $/m^2
End plates	7000 $/m^3	[138]	1200 $/m^3
Other costs	2000 $/m^3	[26]	340 $/m^3

Table 8-2 Annual cost of the separator per watt of power output, based on a lifetime of 1 year for J-cloth and 5 years for the other separators with an interest rate of 6% in a 25-year period

Separator	Cost ($/m^2)	Source	Annual cost ($/m^2)	Annual cost ($/W)		
				2mm	4mm	8mm
Nafion®117	500	[138]	430	1800	1800	1700
Aquivion®E79-03	500	Supplier	430	2500	2400	2400
Celgard®5511	20	Supplier	20	120	100	80
Zirfon®Perl	200	Supplier	170	1200	1000	900
Nylon mesh	5	Supplier	5	40	30	20
Glass fiber filter	5	[80]	5	30	30	20
SciMat®700/20	20	Supplier	20	210	170	120
J-cloth	5	Supplier	20	540	240	140

8.3 Cost of energy production

The cost imposed by the separator per kWh of the energy produced, the energy density, and the revenue produced per unit area of the separator within 5 years of continuous FPMFC operation is presented in Table 8-3. The revenue per unit area of the separator was calculated taking into account the business energy rate of $0.1/kWh from BC Hydro. Since the costs of the other MFC components do not vary when different separators are used, the costs of the separators were compared only. The analysis was also performed based on the assumption that the superficial power density would remain the same when scaling up the FPMFC, which in reality is not the case.

Overall, Nafion®117, Aquivion®, and Zirfon® impose the highest costs to the FPMFC construction per kWh of the energy produced. When the estimated revenue values using these separators are compared to their cost per unit area, it is clear that it is not economically viable to use these separators in the FPMFC construction in large-scale applications. The cost of the porous diaphragms, on the other hand, indicates that there is a higher possibility for a positive offset (product revenue minus the capital cost) using these separators. The application of the micro-porous diaphragms, which yield higher power output than the coarse-pore diaphragms, is a necessary step for this technology to become practically viable.

Assuming an FPMFC setup with an anode chamber depth and volume of 0.008 m and 1 m^3 using a Pt-based cathode and glass fiber separator, the capital cost of the FPMFC sums up to ca. $650/$m^2$/year. The 8 mm FPMFC using the glass fiber filter can produce an energy density of ca. 2 kWh/m^2/yr, therefore an energy price of at least ca. $330/kWh is required for this technology to be profitable. It is worth noting that a high loading of Pt was adopted here to

assure that the cathode was not limiting the FPMFC performance, whereas expensive catalysts like Pt are not going to be adopted in large-scale applications such as wastewater treatment. Eliminating the Pt-cathode with a less expensive bio-cathode will reduce the energy price to ca. $200/kWh. This is still significantly higher than the energy price in Canada, without even taking into account the additional costs such as the cost of the design and engineering, installation, pumps, etc. This indicates that the power output requires a substantial improvement before it can be profitable.

Table 8-3 Cost of the separator, energy density, and revenue of the energy produced over 5 years, estimated based on an interest rate of 6% in a 25-year period and the business energy rate of $0.1/kWh from BC Hydro

Separator	Cost ($/m^2)	Energy density (kWh/m^2)			Separator cost ($/kWh)			Revenue ($/m^2)		
		2mm	4mm	8mm	2mm	4mm	8mm	2mm	4mm	8mm
Nafion®117	2150	10	10	11	200	200	200	1.0	1.0	1.0
Aquivion®E79-03	2150	7	8	8	290	270	270	0.7	0.8	0.8
Celgard®5511	100	6	8	10	10	10	10	0.6	0.8	1.0
Zirfon®Perl	850	6	7	8	140	110	100	0.6	0.7	0.8
Nylon mesh	30	5	6	7	5	5	5	0.5	0.6	0.7
Glass fiber filter	30	7	7	8	5	5	5	0.7	0.7	0.8
SciMat®700/20	100	4	4	6	20	20	10	0.4	0.4	0.6
J-cloth	30	2	4	7	60	30	20	0.2	0.4	0.7

Chapter 9: Conclusions

9.1 Overall conclusions

The goal of this work was to systematically study the separator and its complex effect on the performance of passive air-breathing flat-plate microbial fuel cells (FPMFC). A brief description of each chapter along with the highlights of its conclusions is presented as follows:

1. A passive air-breathing FPMFC was developed using a 3D GF anode, Pt-based cathode, and Nafion®117 membrane, and operated utilizing synthetic wastewater containing ethanol. The preliminary results of the FPMFC engineering and operation indicated that:

   - The presence of a proton exchange membrane (Nafion®117) is necessary during the inoculation of the FPMFC, to act as a barrier to the oxygen diffusing through the air-breathing cathode towards the anaerobic anode. The application of an open structure diaphragm such as J-cloth yields a much lower OCV and peak power density.

   - The continuous operation of FPMFC indicates better stability and peak power density compared to the batch operation, due to a more controlled feed composition and slower biomass accumulation within the 3D anode matrix during the continuous operation.

2. Operation of three passive air-breathing FPMFCs with different depth of the anode chamber (and hence, different electrode spacing) utilizing synthetic wastewater containing ethanol indicated that:

- Activating the surface of the GF substrate, using a boiling solution of HNO_3, results in superior performance over the entire polarization curve, compared to that using an inactivated electrode. The performance using the activated GF indicates major improvement, especially in the kinetic region, due to the increased hydrophilicity and therefore the increased active surface area of the GF substrate. The passive air-breathing FPMFCs using activated GF electrodes produced a peak power density of ca. 0.25 W/m^2, which matched that achieved in the active air flow FPMFCs reported in the literature.

- The effectiveness values of the 3D GF electrode thicknesses of 2×10^{-3} m, 4×10^{-3} m, and 6×10^{-3} m are calculated to be 0.99, 0.98, and 0.96, respectively, indicating that the electrodes are electro-active over 96% of the applied thicknesses. This shows that up to a thickness of 6×10^{-3} m, uniform distribution of current and voltage can be assumed for the GF electrode.

- Increasing the surface area of the anode (through increasing the thickness of the GF substrate) increases the superficial peak power density and the CE, due to an increase in the population of the microbial community contributing to current generation. The peak power densities of ca. 0.35 W/m^2 and ca. 0.52 W/m^2 achieved with 2 and 3 packed layers of GF in the 4 mm and 8 mm FPMFCs, respectively, is higher than those achieved in the active air flow FPMFCs reported in the literature.

- The improved COD removal efficiencies using 2 and 3 layers instead of only 1 layer of GF in the 4 mm and 8 mm FPMFCs is a result of the more efficient utilization of

the anode chamber space, which reduces the portion of wastewater bypassing the 3D GF anode.

3. Characterization of 8 separators (selected from the two category of IEMs and diaphragms) in passive air-breathing and aqueous non-inoculated setups indicated that:

- Oxygen, ethanol, and acetate crossover through the separators are directly related to the pore size of the separators. Hence, the crossover increases as the pore size of the diaphragms increases. The polymeric membranes show the lowest crossover of oxygen, ethanol, and acetate, as opposed to the porous diaphragms.

- The ionic resistivity of the separators is dependant mainly on their thickness and pore size. Overall, the resistivity of the separators increases as their thickness increases. The pore size of the diaphragms, on the other hand, indicates an inverse relationship with the resistivity, that is, there is an increase in the resistivity with a decrease in the pore size.

- Nafion®117 gives the lowest proton transport number of 0.59, and Celgard® and Zirfon® give the highest (0.92), corresponding to an anodic and cathodic pH of 2.9-11 using Nafion®117 and 3.3-10.2 using Celgard® and Zirfon®. The presence of cations other than protons and the neutral pH of the electrolyte are the reasons why a CEM such as Nafion®117 does not conduct protons as efficient as it does in a chemical fuel cell, compared to a diaphragm that is permeable to the electrolyte.

- The equilibrium potential of the oxygen reduction reaction (ORR) increases ca. 0.04 V moving from Nafion®117 to Celgard® and Zirfon®, due to an increase in the

proton transport number of the separator. The increase in the equilibrium potential of ORR is ca. 0.14 V when the cathode is exposed to the PBS with a pH of ca. 8.5. This indicates that even with high proton transport number of 0.92 in the Celgard® and Zirfon®, cathode pH can locally rise up to 10, hindering the ORR.

- All separators, except the Nylon mesh filter, have a hydrophilic surface. The hydrophobic surface of the Nylon can potentially affect its ionic resistivity by trapping the produced gases within the mesh matrix, especially at high current densities.

4. Evaluation of the selected separators in three passive air-breathing FPMFCs with different electrode spacing indicated that:

- The oxygen and ethanol crossover through the separators seem to play a more important role than the other separator characteristics on the FPMFC performance, as they can cause mixed potentials and consequently, electrodes depolarization. The superficial peak power density using diaphragms indicates a direct relationship with the electrode spacing and increases as the electrode spacing increases. The peak power density using different IEMs, however, indicates a relatively independent trend from the electrode spacing within the applied range. Nafion®117 gives the highest peak power in all three FPMFCs, due to its low mass transfer coefficient for oxygen and ethanol. Celgard® indicates comparable performance to Nafion®117 in the 8 mm FPMFC, due to its high proton transport number.

- In general, no significant trend in the performance is observed with the proton transport number and the resistivity of the separator. The effect of the oxygen and fuel crossover seems to be overshadowing the effect of other separator characteristics.

- The hydrophilicity of the separators works in favor of the biofilm growth on their surface. The SEM images from the surface of the (bio)fouled separators show significant biofilm growth on the surface of the hydrophilic separators after 4 weeks of operation. Biofilm growth is observed mainly on the surface of the cathode when using the hydrophobic Nylon mesh, advancing through the pores of the mesh. Biofilm growth is observed on the surface of the cathode when using the diaphragms, whereas no visible biofilm growth on the cathode is observed when using the IEMs, during the operation period.

- The analysis of the cost of the FPMFC indicates that, with the materials used in the laboratory scale, the annual capital cost to construct a passive air-breathing FPMFC (not including the cost of installation, pumps, etc.) with an electrode spacing of 0.008 m, using glass fiber filter as the separator, can be ca. \$650/m^2. The produced power, therefore, requires to be sold at least for ca. \$330/kWh for this technology to be profitable. Replacing the Pt-cathode with a less expensive bio-cathode can reduce the cost; however, other MFC components have to be replaced with less expensive alternatives as well. In addition, the power output of the FPMFC has to increase substantially, for this technology to be a viable alternative in wastewater treatment.

5. Modeling of the passive air-breathing FPMFC based on the mixed potential theory indicated that:

- Ethanol oxidation reaction by the biofilm is kinetically controlled while oxygen reduction reaction by the biofilm is mainly controlled by the transfer of oxygen through the separator.

- Oxygen crossover plays the most important role on the FPMFC performance within the applied range of the electrode spacing. The estimated electrode potentials by the model indicate significant anodic mixed potentials and anode depolarization using the separators with high oxygen crossover. The mixed potentials decrease as the electrode spacing increases.

- The estimated electrode potentials indicate that due to the slow kinetics of the ethanol oxidation reaction on Pt, the mixed potentials at the cathode and the extent of the cathode depolarization does not vary as separators with greater ethanol crossover are used.

- The proton transport number of the separators affects the FPMFC performance through adjusting the cathode potential. The larger estimated cathode potentials by the model using the separators with greater proton transport numbers indicate the importance of the separator ability in transferring protons, as opposed to the other cations present in the MFC environment.

- The peak power densities of the FPMFCs show the greatest sensitivity to the oxygen crossover through the separator. The sensitivity of the peak power to the oxygen crossover decreases as the electrode spacing increases, as the extent of the mixed potentials caused by oxygen at the anode decreases.

- The peak power is relatively less sensitive to the proton transport number of the separator within the measured range. The peak power also shows no sensitivity to the ethanol crossover and the ionic resistivity of the separator, due to kinetically controlled ethanol oxidation on Pt, low ionic conductivity of the electrolyte, and the overshadowing effect of the anodic mixed potentials, caused by oxygen crossover, on the peak power.

- Increasing the electrode spacing beyond the tested values using the model predicts an increase in the peak power density, for the electrode spacing up to 0.02 m. When using electrode spacing larger than 0.02 m, the Ohmic overpotential becomes critical resulting in a decrease in the peak power.

9.2 Significance of research

This research intended to systematically study a variety of applicable separators for the application in the passive air-breathing FPMFC configuration. For this purpose, a novel passive air-breathing FPMFC was developed which offered a high specific surface area and a low Ohmic overpotential. In addition, unlike the FPMFCs reported in the literature developed in two-chamber configurations, the FPMFC developed here consisted of a single chamber offering a simplified configuration with a reduced volume as well as a reduced operating cost

due to the passive supplementation of the oxidant (air) to the cathode. Furthermore, the efficient utilization of the space in the anode chamber and the consequent improved wastewater treatment efficiency is another advantage that the FPMFC configuration using a 3D anode offers over the MFC configurations with large electrode spacing. The passive air-breathing FPMFCs developed here indicate peak power densities that match and are even higher than those reported for the active air flow FPMFCs in the literature [13], [37].

The investigated characteristics of the separators in the non-inoculated passive air-breathing setups can be generalized to any passive air-breathing MFC design using oxygen as the oxidant, as they represent the separators when exposed to air on one side, and the electrolyte on the other side. The evaluation of a variety of separators in the FPMFCs with different electrode spacing, on the other hand, specifies the separator characteristics that are detrimental for the successful operation of a passive air-breathing FPMFC within the applied range of the electrode spacing.

Of high potential application in this study is the developed model. The numerical model developed here is the first model describing the MFC based on the mixed potential theory, which estimates the electrode potentials based on more than one redox reaction happening at the electrodes with the net electrode current of zero. It simply describes a microbial fuel cell as chemical fuel cell and provides valuable information on the anodic and cathodic mixed potentials as well as the electrical current generation controlled by the mass transfer and the kinetics of the redox reactions. This model can be generalized to any MFC system, provided that the appropriate redox reactions as well as the proper kinetic parameters are applied. It also provides valuable insight into the effect of the separator characteristics and the electrode

spacing on the performance of each MFC component as well as the power output. While testing different separator alternatives in the MFC can be time-consuming and costly, plugging the separator characteristics into the developed model can potentially predict the power output of the planar MFC configurations with different electrode spacing.

9.3 Future work and recommendations

In practice, a real MFC system is much more complex than a chemical fuel cell. Hence, it should be noted that the kinetic parameters estimated by the model here are virtual, meaning that all the biological activities of the microbial communities such as the growth and death rate of the cells are ulterior in the estimated parameters. The actual values of the exchange current densities and charge transfer coefficients as well as the mass transfer coefficients can be estimated incorporating biological terms into the applied model, which can provide more accurate information on the bio-electrochemical system while making it more complicated. A more complex model can also provide valuable information on the active thickness of the biofilm and the activity of the biofilm in the formation of byproducts such as the volatile fatty acids (VFA), which is the case in reality. The developed model can also be refined to investigate the optimal combination of the separator characteristics and the electrode spacing that can yield an optimized peak power density and capital cost.

In addition, the developed model here provides a short-term prediction of the peak power and does not consider the long-term stability of the separator, anode, and cathode. Aside from the developed knowledge on the important separator characteristics and their effect on the performance of the passive air-breathing MFC components, extensive material study is also

necessary to further proceed in designing appropriate separators that are proton-specific while insusceptible to oxygen diffusion.

Also, operation of the FPMFC in active mode (through aeration of the cathode) could provide useful information on energy efficiency of an active system in terms of the balance between the operating cost and power output. Although active aeration may affect the performance negatively when coarse pore diaphragms are applied, it can potentially improve the cathode performance when polymeric membranes that are less susceptible to oxygen are applied.

In addition, the time dependant performance of the passive air-breathing FPMFC using different separators is of great importance and needs to be studied in a practical period of time. This is due to the long-term transformation of the bio-catalytic activities as well as the long-term changes in the separator matrix. The bio-catalytic activities of the biofilm can transform over time, due to the characteristics of the separator which alters the DO and cations concentration of the anode compartment, and consequently may alter the build-up of metabolites and sludge within the electrode matrix. The separator itself can suffer from a performance decay due to the (bio)fouling and biodegradation of its matrix over time.

Furthermore, like chemical fuel cells, the local impedance and polarization studies using a segmented test cell (multi-channel synchronized characterization devices) are strongly recommended for further development of the passive air-breathing FPMFCs, as they can provide valuable information on the mass transfer limitations within the biofilm due to inhomogeneous electrode conditions such as local fuel concentration, potential, and current generation.

Bibliography

[1] I. Shizas and D. M. Bagley, "Experimental Determination of Energy Content of Unknown Organics in Municipal Wastewater Streams", *J. Energy Eng.,* 130 (2) 45-53, 2004.

[2] G. Tchobanoglous, F. Burton, and H. D. Stensel, *Wastewater Engineering: Treatment and Reuse*. McGraw-Hill Companies, 2002.

[3] B. E. Logan, *Microbial Fuel Cells*. 2nd ed., John Wiley & Sons, 2008.

[4] O. Lefebvre, A. Uzabiaga, I. S. Chang, B.-H. Kim, and H. Y. Ng, "Microbial fuel cells for energy self-sufficient domestic wastewater treatment-a review and discussion from energetic consideration", *Appl. Microbiol. Biotechnol.*, 89 (2) 259–70, 2011.

[5] T. H. Pham, K. Rabaey, P. Aelterman, P. Clauwaert, L. De Schamphelaire, N. Boon, and W. Verstraete, "Microbial Fuel Cells in Relation to Conventional Anaerobic Digestion Technology", *Eng. Life Sci.*, 6 (3) 285–292, 2006.

[6] S. D. Minteer, N. L. Akers, and C. M. Moore, "Enzyme immobilization for use in biofuel cells and sensors", US Patent, 2009.

[7] J. Kim, H. Jia, and P. Wang, "Challenges in biocatalysis for enzyme-based biofuel cells", *Biotechnol. Adv.*, 24 (3) 296–308, 2006.

[8] G. C. Gil, I. S. Chang, B. H. Kim, M. Kim, J. K. Jang, H. S. Park, and H. J. Kim, "Operational parameters affecting the performannce of a mediator-less microbial fuel cell", *Biosens. Bioelectron.*, 18 (4) 327–334, 2003.

[9] J. K. Jang, T. H. Pham, I. S. Chang, K. H. Kang, H. Moon, K. S. Cho, and B. H. Kim, "Construction and operation of a novel mediator- and membrane-less microbial fuel cell", *Process Biochem.*, 39 (8) 1007–1012, 2004.

[10] B. H. Kim, I. S. Chang, G. C. Gil, H. S. Park, and H. J. Kim, "Novel BOD (biological oxygen demand) sensor using mediator-less microbial fuel cell" *Biotechnol. Lett.*, 25 (7) 541–545, 2003.

[11] B. H. Kim, I. S. Chang, and G. M. Gadd, "Challenges in microbial fuel cell development and operation" *Appl. Microbiol. Biotechnol.*, 76 (3) 485–94, 2007.

[12] H. Liu, R. Ramnarayanan, and B. E. Logan, "Production of Electricity during Wastewater Treatment Using a Single Chamber Microbial Fuel Cell" *Environ. Sci. Technol.*, 38 (7) 2281–2285, 2004.

[13] B. Min and B. E. Logan, “Continuous Electricity Generation from Domestic Wastewater and Organic Substrates in a Flat Plate Microbial Fuel Cell” *Environ. Sci. Technol.*, 38 (21) 5809–5814, 2004.

[14] M. M. Ghangrekar and V. B. Shinde, “Performance of membrane-less microbial fuel cell treating wastewater and effect of electrode distance and area on electricity production” *Bioresour. Technol.*, 98 (15) 2879–85, 2007.

[15] Y. Feng, X. Wang, B. E. Logan, and H. Lee, “Brewery wastewater treatment using air-cathode microbial fuel cells”, *Appl. Microbiol. Biotechnol.*, 78 (5) 873–80, 2008.

[16] J. R. Kim, J. Dec, M. A. Bruns, and B. E. Logan, “Removal of odors from Swine wastewater by using microbial fuel cells”, *Appl. Environ. Microbiol.*, 74 (8) 2540–3, 2008.

[17] Z. He and L. T. Angenent, “Application of Bacterial Biocathodes in Microbial Fuel Cells”, *Electroanalysis,* 18 (19–20) 2009–2015, 2006.

[18] L. M. Tender, C. E. Reimers, H. A. Stecher, D. E. Holmes, D. R. Bond, D. A. Lowy, K. Pilobello, S. J. Fertig, and D. R. Lovley, “Harnessing microbially generated power on the seafloor”, *Nat. Biotechnol.*, 20 (8) 821–5, 2002.

[19] H. Moon, I. S. Chang, K. H. Kang, J. K. Jang, and B. H. Kim, “Improving the dynamic response of a mediator-less microbial fuel cell as a biochemical oxygen demand (BOD) sensor” *Biotechnol. Lett.*, 26 (22) 1717–1721, 2004.

[20] I. S. Chang, J. K. Jang, G. C. Gil, M. Kim, H. J. Kim, B. W. Cho, and B. H. Kim, “Continuous determination of biochemical oxygen demand using microbial fuel cell type biosensor”, *Biosens. Bioelectron.*, 19 (6) 607–613, 2004.

[21] S. Wilkinson, “Hungry for success – future directions in gastrobotics research” *Ind. Robot An Int. J.*, 28 (3) 213–219, 2001.

[22] C. Melhuish, I. Ieropoulos, J. Greenman, and I. Horsfield, “Energetically autonomous robots: Food for thought”, *Auton. Robots*, 21 (3) 187–198, 2006.

[23] I. Kelly, “The design of a robotic predator: The SlugBot”, *Robotica*, 21 (4) 399–406, 2003.

[24] R. A. Bullen, T. C. Arnot, J. B. Lakeman, and F. C. Walsh, “Biofuel cells and their development”, *Biosens. Bioelectron.*, 21 (11) 2015–2045, 2006.

[25] R. K. Jung, S. Cheng, S.-E. Oh, and B. E. Logan, “Power generation using different cation, anion, and ultrafiltration membranes in microbial fuel cells”, *Environ. Sci. Technol.*, 41 (3) 1004 – 1009, 2007.

[26] R. A. Rozendal, H. V. M. Hamelers, K. Rabaey, J. Keller, and C. J. N. Buisman, "Towards practical implementation of bioelectrochemical wastewater treatment", *Trends Biotechnol.*, 26 (8) 450–459, 2008.

[27] W. W. Li, G. P. Sheng, X. W. Liu, and H. Q. Yu, "Recent advances in the separators for microbial fuel cells", *Bioresour. Technol.*, 102 (1) 244-252, 2010.

[28] F. Harnisch, R. Warmbier, R. Schneider, and U. Schröder, "Modeling the ion transfer and polarization of ion exchange membranes in bioelectrochemical systems", *Bioelectrochemistry*, 75 (2) 136–141, 2009.

[29] F. Harnisch and U. Schröder, "Selectivity versus mobility: separation of anode and cathode in microbial bioelectrochemical systems", *ChemSusChem*, 2 (10) 921–6, 2009.

[30] T. Ha. Pham, J. K. Jang, H. S. Moon, I. S. Chang, and B. H. Kim, "Improved Performance of Microbial Fuel Cell Using Membrane-Electrode Assembly", 15 (2) 438–441, 2005.

[31] X. Zhang, S. Cheng, X. Huang, and B. E. Logan, "The use of nylon and glass fiber filter separators with different pore sizes in air-cathode single-chamber microbial fuel cells", *Energy Environ. Sci.*, 3 (5) 659, 2010.

[32] A. ter Heijne, H. V. M. Hamelers, and C. J. N. Buisman, "Microbial Fuel Cell Operation with Continuous Biological Ferrous Iron Oxidation of the Catholyte", *Environ. Sci. Technol.*, 41 (11) 4130–4134, 2007.

[33] P. L. McCarty and R. E. McKinney, "Salt toxicity in Anaerobic Digestion", *J. Water Pollution Control Federation*, 33 (4) 399-415, 1961.

[34] S. Cheng, H. Liu, and B. E. Logan, "Increased Power Generation in a Continuous Flow MFC with Advective Flow through the Porous Anode and Reduced Electrode Spacing", *Environ. Sci. Technol.*, 40 (7) 2426–2432, 2006.

[35] M. Helder, D. P. Strik, H. V. Hamelers, and C. J. Buisman, "The flat-plate plant-microbial fuel cell: the effect of a new design on internal resistances", *Biotechnol. Biofuels*, 5 (1) 70, 2012.

[36] A. ter Heijne, H. V. M. Hamelers, V. de Wilde, R. A. Rozendal, and C. J. N. Buisman, "A Bipolar Membrane Combined with Ferric Iron Reduction as an Efficient Cathode System in Microbial Fuel Cells", *Environ. Sci. Technol.*, 40 (17) 5200–5205, 2006.

[37] A. Dekker, A. Ter Heijne, M. Saakes, H. V. M. Hamelers, and C. J. N. Buisman, "Analysis and improvement of a scaled-up and stacked microbial fuel cell", *Environ. Sci. Technol.*, 43 (23) 9038–42, 2009.

[38] B. Tartakovsky, M.-F. Manuel, V. Neburchilov, H. Wang, and S. R. Guiot, "Biocatalyzed hydrogen production in a continuous flow microbial fuel cell with a gas phase cathode", *J. Power Sources*, 182 (1) 291–297, 2008.

[39] B. K. Kho, B. Bae, M. A. Scibioh, J. Lee, and H. Y. Ha, "On the consequences of methanol crossover in passive air-breathing direct methanol fuel cells", *J. Power Sources*, 142 (1) 50–55, 2005.

[40] V. Saarinen, O. Himanen, T. Kallio, G. Sundholm, and K. Kontturi, "A 3D model for the free-breathing direct methanol fuel cell: Methanol crossover aspects and validations with current distribution measurements", *J. Power Sources*, 172 (2) 805–815, 2007.

[41] R. Chen, T. S. Zhao, and J. G. Liu, "Effect of cell orientation on the performance of passive direct methanol fuel cells", *J. Power Sources*, 157 (1) 351–357, 2006.

[42] T. Shimizu, T. Momma, M. Mohamedi, T. Osaka, and S. Sarangapani, "Design and fabrication of pumpless small direct methanol fuel cells for portable applications", *J. Power Sources*, 137 (2) 277–283, 2004.

[43] R. C. T. S. Zhao, "Small direct methanol fuel cells with passive supply of reactants", *J. Power Sources*, 191 (2) 185–202, 2009.

[44] X. Zhang, S. Cheng, X. Wang, X. Huang, and B. E. Logan, "Separator Characteristics for Increasing Performance of Microbial Fuel Cells", *Environ. Sci. Technol.*, 43 (21) 8456–8461, 2009.

[45] M. Ghasemi, W. R. Wan Daud, M. Ismail, M. Rahimnejad, A. F. Ismail, J. X. Leong, M. Miskan, and K. Ben Liew, "Effect of pre-treatment and biofouling of proton exchange membrane on microbial fuel cell performance", *Int. J. Hydrogen Energy*, 38 (13) 5480–5484, 2013.

[46] J. Winfield, I. Ieropoulos, J. Rossiter, J. Greenman, and D. Patton, "Biodegradation and proton exchange using natural rubber in microbial fuel cells", *Biodegradation*, 24 (6) 733-739, 2013.

[47] G. J. Lamont, C. Schwab, H. H. Voss, and D. P. Wilkinson, "Embossed fluid flow field plate for electrochemical fuel cells", US Patent,1996.

[48] C. Y. Chow and H. H. Voss, "Coolant flow field plate for electrochemical fuel cells", US Patent, 1993.

[49] C. A. Reiser, "Water and heat management in solid polymer fuel cell stack", US Patent, 1989.

[50] C. A. Resier and R. D. Sawyer, “Solid polymer electrolyte fuel cell stack water management system.” US Patent, 1988.

[51] N. W. DeLuca and Y. A. Elabd, “Polymer electrolyte membranes for the direct methanol fuel cell: A review”, *J. Polym. Sci. Part B Polym. Phys.*, 44 (16) 2201–2225, 2006.

[52] M. Helder, D. P. B. T. B. Strik, H. V. M. Hamelers, A. J. Kuhn, C. Blok, and C. J. N. Buisman, “Concurrent bio-electricity and biomass production in three Plant-Microbial Fuel Cells using Spartina anglica, Arundinella anomala and Arundo donax”, *Bioresour. Technol.*, 101 (10) 3541–3547, 2010.

[53] H. Liu and B. E. Logan, “Electricity Generation Using an Air-Cathode Single Chamber Microbial Fuel Cell in the Presence and Absence of a Proton Exchange Membrane”, *Environ. Sci. Technol.*, 38 (14) 4040–4046, 2004.

[54] B. Logan, S. Cheng, V. Watson, and G. Estadt, “Graphite Fiber Brush Anodes for Increased Power Production in Air-Cathode Microbial Fuel Cells”, *Environ. Sci. Technol.*, 41 (9) 3341–3346, 2007.

[55] Y. Fan, H. Hu, and H. Liu, “Enhanced Coulombic efficiency and power density of air-cathode microbial fuel cells with an improved cell configuration”, *J. Power Sources*, 171 (2) 348–354, 2007.

[56] Y. Fan, H. Hu, and H. Liu, “Sustainable Power Generation in Microbial Fuel Cells Using Bicarbonate Buffer and Proton Transfer Mechanisms”, *Environ. Sci. Technol.*, 41 (23) 8154–8158, 2007.

[57] M. Rosenbaum, F. Zhao, U. Schröder, and F. Scholz, “Interfacing electrocatalysis and biocatalysis with tungsten carbide: a high-performance, noble-metal-free microbial fuel cell”, *Angew. Chem. Int. Ed. Engl.*, 45 (40) 6658–61, 2006.

[58] K. Rabaey, G. Lissens, S. D. Siciliano, and W. Verstraete, “A microbial fuel cell capable of converting glucose to electricity at high rate and efficiency”, *Biotechnol. Lett.*, 25 (18) 1531–1535, 2003.

[59] K. Rabaey, N. Boon, S. D. Siciliano, M. Verhaege, and W. Verstraete, “Biofuel cells select for microbial consortia that self-mediate electron transfer”, *Appl. Environ. Microbiol.*, 70 (9) 5373–82, 2004.

[60] U. Schr\öder, J. Nie\ssen, and F. Scholz, “A generation of microbial fuel cells with current outputs boosted by more than one order of magnitude”, *Angew. Chemie*, 115 (25) 2986–2989, 2003.

[61] B. R. Ringeisen, R. Ray, and B. Little, “A miniature microbial fuel cell operating with an aerobic anode chamber”, *J. Power Sources*, 165 (2) 591–597, 2007.

[62] M. Vera, A. Schippers, and W. Sand, “Progress in bioleaching: fundamentals and mechanisms of bacterial metal sulfide oxidation--part A”, *Appl. Microbiol. Biotechnol.*, 97 (17) 7529–41, 2013.

[63] M. Helder, D. P. B. T. B. Strik, H. V. M. Hamelers, R. C. P. Kuijken, and C. J. N. Buisman, “New plant-growth medium for increased power output of the Plant-Microbial Fuel Cell”, *Bioresour. Technol.*, 104, 417–423, 2012.

[64] Y. Zuo, S. Cheng, and B. E. Logan, “Ion Exchange Membrane Cathodes for Scalable Microbial Fuel Cells”, *Environ. Sci. Technol.*, 42 (18) 6967–6972, 2008.

[65] A. Bergel, D. Féron, H.-C. Flemming, I. Ieropoulos, J. Greenman, and C. Melhuish, “Improved energy output levels from small-scale Microbial Fuel Cells”, *Bioelectrochemistry*, 78 (1) 44–50, 2010.

[66] J. R. Kim, S. H. Jung, J. M. Regan, and B. E. Logan, “Electricity generation and microbial community analysis of alcohol powered microbial fuel cells”, *Bioresour. Technol.*, 98 (13) 2568–2577, 2007.

[67] B. Min, J. Kim, S. Oh, J. M. Regan, and B. E. Logan, “Electricity generation from swine wastewater using microbial fuel cells”, *Water Res.*, 39 (20) 4961–4968, 2005.

[68] K. Rabaey, P. Clauwaert, P. Aelterman, and W. Verstraete, “Tubular Microbial Fuel Cells for Efficient Electricity Generation”, *Environ. Sci. Technol.*, 39 (20) 8077–8082, 2005.

[69] J. R. Kim, G. C. Premier, F. R. Hawkes, R. M. Dinsdale, and A. J. Guwy, “Development of a tubular microbial fuel cell (MFC) employing a membrane electrode assembly cathode”, *J. Power Sources*, 187 (2) 393–399, 2009.

[70] Y. Zuo, S. Cheng, D. Call, and B. E. Logan, “Tubular Membrane Cathodes for Scalable Power Generation in Microbial Fuel Cells”, *Environ. Sci. Technol.*, 41 (9) 3347–3353, 2007.

[71] J. Sun, Y. Hu, Z. Bi, and Y. Cao, “Improved performance of air-cathode single-chamber microbial fuel cell for wastewater treatment using microfiltration membranes and multiple sludge inoculation”, *J. Power Sources*, 187 (2) 471–479, 2009.

[72] K. J. Chae, M. J. Choi, J. W. Lee, K. Y. Kim, and I. S. Kim, “Effect of different substrates on the performance, bacterial diversity, and bacterial viability in microbial fuel cells”, *Bioresour. Technol.*, 100 (14) 3518–3525, 2009.

[73] J. C. Biffinger, R. Ray, B. Little, and B. R. Ringeisen, “Diversifying Biological Fuel Cell Designs by Use of Nanoporous Filters”, *Environ. Sci. Technol.*, 41 (4) 1444–1449, 2007.

[74] R. A. Rozendal, H. V. M. Hamelers, and C. J. N. Buisman, “Effects of Membrane Cation Transport on pH and Microbial Fuel Cell Performance”, *Environ. Sci. Technol.*, 40 (17) 5206–5211, 2006.

[75] F. Harnisch, U. Schröder, and F. Scholz, “The suitability of monopolar and bipolar ion exchange membranes as separators for biological fuel cells”, *Environ. Sci. Technol.*, 42 (5) 1740–1746, 2008.

[76] I. Ieropoulos, J. Greenman, and C. Melhuish, “Improved energy output levels from small-scale Microbial Fuel Cells”, *Bioelectrochemistry*, 78 (1) 44–50, 2010.

[77] X. Zhang, S. Cheng, X. Huang, and B. E. Logan, “Improved performance of single-chamber microbial fuel cells through control of membrane deformation”, *Biosensors and Bioelectronics*, 25 (7) 1825–1828, 2010.

[78] P. J. Kulesza, N. Alonso-Vante, J. Augustynski, D. Pant, G. Van Bogaert, M. De Smet, L. Diels, and K. Vanbroekhoven, “Use of novel permeable membrane and air cathodes in acetate microbial fuel cells”, *Electrochim. Acta*, 55 (26) 7710–7716, 2010.

[79] A. Basile, M. De Falco, S. S. Lim, W. R. W. Daud, J. Md Jahim, M. Ghasemi, P. S. Chong, and M. Ismail, “Sulfonated poly(ether ether ketone)/poly(ether sulfone) composite membranes as an alternative proton exchange membrane in microbial fuel cells”, *Int. J. Hydrogen Energy*, 37 (15) 11409–11424, 2012.

[80] A. Pandey, D. J. Lee, B. E. Logan, X. Zhang, S. Cheng, P. Liang, and X. Huang, “Scalable air cathode microbial fuel cells using glass fiber separators, plastic mesh supporters, and graphite fiber brush anodes”, *Bioresour. Technol.*, 102 (1) 372–375, 2011.

[81] S. Venkata Mohan, S. Veer Raghavulu, and P. N. Sarma, “Biochemical evaluation of bioelectricity production process from anaerobic wastewater treatment in a single chambered microbial fuel cell (MFC) employing glass wool membrane”, *Biosens. Bioelectron.*, 23 (9) 1326–32, 2008.

[82] L. Zhuang, S. Zhou, Y. Wang, C. Liu, and S. Geng, “Membrane-less cloth cathode assembly (CCA) for scalable microbial fuel cells”, *Biosens. Bioelectron.*, 24 (12) 3652–3656, 2009.

[83] Y. Zuo, S. Cheng, and B. E. Logan, “Ion Exchange Membrane Cathodes for Scalable Microbial Fuel Cells”, *Environ. Sci. Technol.*, 42 (18) 6967–6972, 2008.

[84] B. R. Breslau and I. F. Miller, "A Hydrodynamic Model for Electroosmosis", *Ind. Eng. Chem. Fundam.*, 10 (4) 554–565, 1971.

[85] K. D. Kreuer, S. J. Paddison, E. Spohr, and M. Schuster, "Transport in Proton Conductors for Fuel-Cell Applications: Simulations, Elementary Reactions, and Phenomenology", *Chem. Rev.*, 104 (10) 4637–4678, 2004.

[86] K. J. Chae, M. Choi, F. F. Ajayi, W. Park, I. S. Chang, and I. S. Kim, "Mass Transport through a Proton Exchange Membrane (Nafion) in Microbial Fuel Cells", *Energy & Fuels*, 22 (1) 169–176, 2008.

[87] S. Oh and B. E. Logan, "Hydrogen and electricity production from a food processing wastewater using fermentation and microbial fuel cell technologies", *Water Res.*, 39 (19) 4673–4682, 2005.

[88] S. V. Raghavulu, S. V. Mohan, R. K. Goud, and P. N. Sarma, "Effect of anodic pH microenvironment on microbial fuel cell (MFC) performance in concurrence with aerated and ferricyanide catholytes", *Electrochemistry Communications*, 11 (2) 371–375, 2009.

[89] B. Min, J. Kim, S. Oh, J. M. Regan, and B. E. Logan, "Electricity generation from swine wastewater using microbial fuel cells", *Water Res.*, 39 (20) 4961–4968, 2005.

[90] Z. He, S. D. Minteer, and L. T. Angenent, "Electricity Generation from Artificial Wastewater Using an Upflow Microbial Fuel Cell", *Environ. Sci. Technol.*, 39 (14) 5262–5267, 2005.

[91] S. Chen, G. Liu, R. Zhang, B. Qin, and Y. Luo, "Development of the microbial electrolysis desalination and chemical-production cell for desalination as well as acid and alkali productions", *Environ. Sci. Technol.*, 46 (4) 2467–72, 2012.

[92] X. Cao, X. Huang, P. Liang, K. Xiao, Y. Zhou, X. Zhang, and B. E. Logan, "A New Method for Water Desalination Using Microbial Desalination Cells", *Environ. Sci. Technol.*, 43 (18) 7148–7152, 2009.

[93] M. Kim, M. S. Hyun, G. M. Gadd, G. T. Kim, S.-J. Lee, and H. J. Kim, "Membrane-electrode assembly enhances performance of a microbial fuel cell type biological oxygen demand sensor", *Environ. Technol.*, 30 (4) 329–36, 2009.

[94] S. J. You, J. Y. Wang, N. Q. Ren, X. H. Wang, and J. N. Zhang, "Sustainable conversion of glucose into hydrogen peroxide in a solid polymer electrolyte microbial fuel cell", *ChemSusChem*, 3 (3) 334–8, 2010.

[95] R. A. Rozendal, H. V. M. Hamelers, R. J. Molenkamp, and C. J. N. Buisman, "Performance of single chamber biocatalyzed electrolysis with different types of ion exchange membranes", *Water Res.*, 41 (9) 1984 – 1994, 2007.

[96] H. . Hurwitz and R. Dibiani, "Investigatin of electrical properties of bipolar membranes at steady state and with transient methods", *Electrochim. Acta*, 47 (5) 759–773, 2001.

[97] R. W. Baker, *Membrane technology and applications*. John Wiley and Sons, 2004.

[98] X. Zhang, H. Sun, P. Liang, X. Huang, X. Chen, and B. E. Logan, "Air-cathode structure optimization in separator-coupled microbial fuel cells", *Biosens. Bioelectron.*, 30 (1) 267–271, 2011.

[99] M. J. Tatton, D. B. Archer, G. E. Powell, and M. L. Parker, "Methanogenesis from Ethanol by Defined Mixed Continuous Cultures", *Appl. Envir. Microbiol.*, 55 (2) 440–445, 1989.

[100] H. Liu, S. Cheng, and B. E. Logan, "Power generation in fed-batch microbial fuel cells as a function of ionic strength, temperature, and reactor configuration", *Environ. Sci. Technol*, 39 (14) 5488–5493, 2005.

[101] K. J. Chae, M. Choi, F. F. Ajayi, W. Park, I. S. Chang, and I. S. Kim, "Mass Transport through a Proton Exchange Membrane (Nafion) in Microbial Fuel Cells", *Energy & Fuels*, 22 (1) 169–176, 2008.

[102] L. Giorgi, E. Antolini, A. Pozio, and E. Passalacqua, "Influence of the PTFE content in the diffusion layer of low-Pt loading electrodes for polymer electrolyte fuel cells", *Electrochim. Acta*, 43 (24) 3675–3680, 1998.

[103] S. Cheng, H. Liu, and B. E. Logan, "Increased performance of single-chamber microbial fuel cells using an improved cathode structure", *Electrochemistry Communications*, 8 (3) 489–494, 2006.

[104] S. Cheng and B. E. Logan, "Ammonia treatment of carbon cloth anodes to enhance power generation of microbial fuel cells", *Electrochemistry Communications*, 9 (3) 492–496, 2007.

[105] N. Zhu, X. Chen, T. Zhang, P. Wu, P. Li, and J. Wu, "Improved performance of membrane free single-chamber air-cathode microbial fuel cells with nitric acid and ethylenediamine surface modified activated carbon fiber felt anodes", *Bioresour. Technol.*, 102 (1) 422–6, 2011.

[106] S.-E. Oh and B. E. Logan, “Proton exchange membrane and electrode surface areas as factors that affect power generation in microbial fuel cells”, *Appl. Microbiol. Biotechnol.*, 70 (2) 162–9, 2006.

[107] M. Di Lorenzo, K. Scott, T. P. Curtis, and I. M. Head, “Effect of increasing anode surface area on the performance of a single chamber microbial fuel cell”, *Chem. Eng. J.*, 156 (1) 40–48, 2010.

[108] L. Lianhua, K. Xiaoying, S. Yongming, Y. Zhenhong, and L. Ying, “Performance of microbial fuel cell in different anode and cathode electrode sizes”, *International Conference on Remote Sensing, Environment and Transportation Engineering*, 7707–7710, 2011.

[109] P. D. Kiely, G. Rader, J. M. Regan, and B. E. Logan, “Long-term cathode performance and the microbial communities that develop in microbial fuel cells fed different fermentation endproducts”, *Bioresour. Technol.*, 102 (1) 361–6, 2011.

[110] T. Shimoyama, S. Komukai, A. Yamazawa, Y. Ueno, B. E. Logan, and K. Watanabe, “Electricity generation from model organic wastewater in a cassette-electrode microbial fuel cell” *Appl. Microbiol. Biotechnol.*, 80 (2) 325–30, 2008.

[111] S. K. Chaudhuri and D. R. Lovley, “Electricity generation by direct oxidation of glucose in mediatorless microbial fuel cells”, *Nat. Biotechnol.*, 21 (10) 1229–32, 2003.

[112] D. Prasad, T. K. Sivaram, S. Berchmans, and V. Yegnaraman, “Microbial fuel cell constructed with a micro-organism isolated from sugar industry effluent”, *Journal of Power Sources*, 160 (2) 991–996, 2006.

[113] T. Song, W. Tan, X. Wu, and C. C. Zhou, “Effect of graphite felt and activated carbon fiber felt on performance of freshwater sediment microbial fuel cell”, *J. Chem. Technol. Biotechnol.*, 87 (10) 1436–1440, 2012.

[114] C. Oloman, *Electrochemical processing for the pulp and paper industry*, 2nd ed., The electrochemical consultancy, 1997.

[115] J. R. Kim, B. Min, and B. E. Logan, “Evaluation of procedures to acclimate a microbial fuel cell for electricity production.”, *Appl. Microbiol. Biotechnol.*, 68 (1) 23–30, 2005.

[116] K. Scott, *Electrochemical reaction engineering*. 2nd ed., Academic Press, 1991.

[117] Y. Feng, Q. Yang, X. Wang, and B. E. Logan, “Treatment of carbon fiber brush anodes for improving power generation in air–cathode microbial fuel cells”, *Journal of Power Sources*, 195 (7) 1841–1844, 2010.

[118] A. Brennsteiner, J. W. Zondlo, A. H. Stiller, P. G. Stansberry, D. Tian, and Y. Xu, "Environmental Pollution Control Devices Based on Novel Forms of Carbon: Heavy Metals", *Energy & Fuels*, 11 (2) 348–353, 1997.

[119] Z. K. Ma and J. Liu, "Effect of surface oxygenic functional groups of modified carbon fibres on immobilization of denitrifying bacterium", *Funct. Mater.*, 34, 592–594, 2003.

[120] A. Aziznia, C. W. Oloman, and E. L. Gyenge, "Platinum- and membrane-free swiss-roll mixed-reactant alkaline fuel cell", *ChemSusChem*, 6 (5) 847–55, 2013.

[121] J. Lipkowski, S. Roscoe, A. Lam, D. P. Wilkinson, and J. Zhang, "Novel approach to membraneless direct methanol fuel cells using advanced 3D anodes", *Electrochim. Acta*, 53 (23) 6890–6898, 2008.

[122] H. Richter, K. P. Nevin, H. Jia, D. A. Lowy, D. R. Lovley, and L. M. Tender, "Cyclic voltammetry of biofilms of wild type and mutant Geobacter sulfurreducens on fuel cell anodes indicates possible roles of OmcB, OmcZ, type IV pili, and protons in extracellular electron transfer", *Energy Environ. Sci.*, 2 (5) 506, 2009.

[123] M. Ghangrekar, V. B,. Shinde, and N. Duteanu, "Effect of Wastewater Characteristics and Biomass Growth in Cathode Compartment on Performance of Membrane-less Microbial Fuel Cell", *Revista de Chimie*, 61 (3) 272-280, 2010.

[124] A. Kato Marcus, C. I. Torres, and B. E. Rittmann, "Conduction-based modeling of the biofilm anode of a microbial fuel cell," *Biotechnol. Bioeng.*, vol. 98, no. 6, pp. 1171–1182, 2007.

[125] C. Picioreanu, M. C. M. van Loosdrecht, K. P. Katuri, K. Scott, and I. M. Head, "Mathematical model for microbial fuel cells with anodic biofilms and anaerobic digestion.," *Water Sci. Technol.*, vol. 57, no. 7, pp. 965–71, Jan. 2008.

[126] C. Picioreanu, I. M. Head, K. P. Katuri, M. C. M. van Loosdrecht, and K. Scott, "A computational model for biofilm-based microbial fuel cells," *Water Res.*, vol. 41, no. 13, pp. 2921–2940, Jul. 2007.

[127] J. M. Correa, F. A. Farret, V. A. Popov, and M. G. Simoes, "Sensitivity Analysis of the Modeling Parameters Used in Simulation of Proton Exchange Membrane Fuel Cells", *IEEE Trans. Energy Convers.*, 20 (1) 211–218, 2005.

[128] L. Pons, M.-L. Délia, and A. Bergel, "Effect of surface roughness, biofilm coverage and biofilm structure on the electrochemical efficiency of microbial cathodes", *Bioresour. Technol.*, 102 (3) 2678–83, 2011.

[129] C. Dumas, R. Basseguy, and A. Bergel, "Microbial electrocatalysis with Geobacter sulfurreducens biofilm on stainless steel cathodes", *Electrochim. Acta*, 53 (5) 2494–2500, 2008.

[130] B. Erable, L. Etcheverry, and A. Bergel, "Increased power from a two-chamber microbial fuel cell with a low-pH air-cathode compartment", *Electrochemistry Communications*, 11 (3) 619–622, 2009.

[131] J. l. Liu, D. a. Lowy, R. g. Baumann, and L. m. Tender, "Influence of anode pretreatment on its microbial colonization", *J. Appl. Microbiol.*, 102 (1) 177–183, 2007.

[132] S. Srikanth and S. Venkata Mohan, "Change in electrogenic activity of the microbial fuel cell (MFC) with the function of biocathode microenvironment as terminal electron accepting condition: influence on overpotentials and bio-electro kinetics", *Bioresour. Technol.*, 119, 241–51, 2012.

[133] S. Oh, B. Min, and B. E. Logan, "Cathode Performance as a Factor in Electricity Generation in Microbial Fuel Cells", *Environ. Sci. Technol.*, 38 (18) 4900–4904, 2004.

[134] B. Wang, "Recent development of non-platinum catalysts for oxygen reduction reaction", *J. Power Sources*, vol. 152, 1–15, 2005.

[135] J. X. Wang, N. M. Markovic, and R. R. Adzic, "Kinetic Analysis of Oxygen Reduction on Pt(111) in Acid Solutions: Intrinsic Kinetic Parameters and Anion Adsorption Effects", *J. Phys. Chem. B*, 108 (13) 4127–4133, 2004.

[136] J. K. Nørskov, J. Rossmeisl, A. Logadottir, L. Lindqvist, J. R. Kitchin, T. Bligaard, and H. Jónsson, "Origin of the Overpotential for Oxygen Reduction at a Fuel-Cell Cathode," *J. Phys. Chem. B*, 108 (46) 17886–17892, 2004.

[137] S. Aiyuk, I. Forrez, D. K. Lieven, A. van Haandel, and W. Verstraete, "Anaerobic and complementary treatment of domestic sewage in regions with hot climates- A review", *Bioresour. Technol.*, 97 (17) 2225–2241, 2006.

[138] H. Tsuchiya and O. Kobayashi, "Mass production cost of PEM fuel cell by learning curve", *Int. J. Hydrogen Energy*, 29 (10) 985–990, 2004.

[139] R. M. Atlas, *Handbook of Microbiological Media*, 3rd ed., CRC Press, 2004.

[140] Apha, E. W. Rice, A. W. W. Association, R. B. Baird, A. D. Eaton, Wef, and L. S. Clesceri, *Standard Methods for Examination of Water and Wastewater 2012*, 22nd ed., Washington: Amer Public Health Assn, 2012.

Appendices

Appendix A Experimental procedures

A.1 Cathode preparation

The air cathode consisted of a carbon cloth substrate (projected surface area: 0.05 m × 0.10 m; 50 wt.% wet-proofing, E-TEK, USA) coated on one side with Pt catalyst facing the membrane and on the other side, with three layers of a 60 wt.% PTFE suspension [98]. A high loading of Pt was adopted to assure that the cathode was not limiting the performance. A carbon base layer ink was prepared by mixing carbon powder (Vulcan XC-72), 60 wt.% PTFE solution (weight ratio of carbon powder to PTFE: 4), and isopropyl alcohol together, and sonicating the ink for 1 hour. The carbon base layer was applied onto one side of the carbon cloth using the CNC sprayer, placed on top of a hot-plate at 323 K. The electrode was further heated in a furnace at 643 K for 30 minutes. The resulting base layer loading was 0.025 kg/m^2 (2.5 mg/cm^2).

Three layers of the 60% PTFE suspension were then applied onto the carbon base layer using a brush. Application of each layer was followed by 10 minutes of air-drying and 10 minutes of heating at 643 K. The catalyst ink was prepared by addition of Pt (Platinum/XC72R, 40 wt.%, Johnson Matthey, USA) and Nafion solution (0.05 kg per kg of catalyst powder) into a mixture of methanol and water (0.05 m^3 of each per kg of catalyst powder), followed by vigorous mixing and sonication, each for 1 hour. The ink was then applied onto the other side of the carbon cloth using the CNC sprayer. The resulting Pt loading was 0.01 kg/m^2 (1 mg/cm^2).

A.2 Nafion®117 treatment

Nafion®117 (DuPont, USA) was used as the PEM. Nafion®117 was soaked in a 3 wt.% boiling solution of H_2O_2 for 30 minutes, and rinsed with DI water. It was then soaked in a 0.5 M boiling solution of H_2SO_4 for 30 minutes, rinsed with DI water, and was stored in DI water prior to being used.

A.3 Synthetic wastewater preparation

A nutrient medium containing mineral and vitamin solutions (0.0125 m^3/m^3 of the medium solution) in 0.05 M phosphate buffer solution (PBS) was prepared as the synthetic wastewater. Ethanol was added as the fuel (0.085 M). Table A- 1 through A-3 present the composition of the nutrient medium, mineral, and vitamin solutions. The synthetic wastewater was autoclaved at 393 K for 20 minutes prior being utilized to the FPMFC.

Table A- 1 Composition of the nutrient solution representing the synthetic wastewater [133]

Compound	Concentration (kg/m^3)
KCL	0.13
$NaHCO_3$	3.13
NH_4Cl	1.0
$NaH_2PO_4.H_2O$	2.92
$Na_2HPO_4.7H_2O$	7.73
Yeast extract	1.0

Table A- 2 Composition of the mineral solution [139]

Compound	Concentration (kg/m^3)
Nitrilotriacetic acid	1.5
$MgSO_4.7H_2O$	3.0
$MnSO_4.H_2O$	0.5
NaCl	1.0
$FeSO_4.7H_2O$	0.1
$CoCl_2.6H_2O$	0.1
$CaCl_2$	0.1
$ZnSO_4.7H_2O$	0.1
$CuSO_4.5H_2O$	0.01
$KAl(SO_4)_2.12H_2O$	0.01
H_3BO_3	0.01
$Na_2MoO_4.2H_2O$	0.01

Table A- 3 Composition of the vitamin solution [139]

Compound	Concentration $\times 10^{-3}$ (kg/m^3)
Biotin	2.0
Folic acid	2.0
Pyridoxine HCl	10.0
Thiamine HCl	5.0
Riboflavin	5.0
Nicotinic acid	5.0
Calcium D-(+)-pantothenate	5.0
Cyanocobalamine	0.1
P-Aminobenzoic acid	5.0
Thioctic acid	5.0

A.4 Development of the polarization and power density curves

A Potentiostat (VERSASTATE 3, Princeton Applied Research, USA) was used to develop the polarization curves. Chronoamperometry was used to obtain the curves allowing 1 hour for the stabilization of each step. The superficial current and power densities were calculated by dividing the current and power, respectively, by the geometrical surface area of the membrane (50×10^{-4} m^2). The volumetric current and power densities were calculated by dividing the current and power, respectively, by the empty anode chamber volume (10^{-5} m^3, 2×10^{-5} m^3, and 4×10^{-5} m^3 in the 2 mm, 4 mm , and 8 mm FPMFCs, respectively).

A.5 Electrochemical impedance spectroscopy

The Potentiostat was used for the impedance measurements. The internal resistance was measured using the electrochemical impedance spectroscopy (EIS) technique, which consisted of superimposing, at open circuit, a sinusoidal signal with an amplitude of 0.01 V and a frequency varying from 100 KHz to 0.005 Hz. The internal resistance values were then extracted from the intersection of the Nyquist plot and the axis of the real component of the impedance (Z_{re}).

A.6 Organic content measurements

The COD of the samples was investigated by oxidizing the organic contents through digestion with an acid-dichromate solution in the presence of a silver sulfate catalyst. The COD measurements were carried out according to the standard method 5220 [140] (Hach COD system, Hach Company, Canada). Absorbance measurement was carried out using a UV-vis spectrophotometer (Shimadzu UV-Mini 1240). The COD removal efficiency values were then

calculated by dividing the COD removed by the inlet COD content. In addition to COD measurements, the total organic carbon (TOC) of the collected samples was analyzed using a UV/persulfate oxidation TOC analyzer (Shimadzu TOC-VCPH). The results were in agreement with the COD values and hence, were not presented here.

Appendix B Model programming code from MATLAB

B.1 Parameter estimation

```
clear all

close all

clc

format long

global Ea Ec joa jea Koa_b Kea_b Po Eoc0 Eoa0 Eec0 Eea0 alfaea alfaec alfaoa alfaoc jec joc

global N M K R T ne no F Co d S RR Ce pHa pHc Doa_s Koc Koa Kea Jexp Jpred Eexp Eohm Jmtea
Jmtoa Jmtec Jmtoc Jctea Jctoa Jctec Jctoc Jao Jae Jce Jco
```

Parameters and variables

```
N=7;    % # of membranes

M=8;    % # of data points for each membrane

K=3;    % # of fuel cells

R=8.314;        % Universal gas constant (J/mol/K)

T=303; % Temperature (K)

ne=12;  % # of electrons transferred in EtOH oxidation

no=4;           % # of electrons transferred in oxygen reduction

F=96485.3;      % Faraday constant (C/mol)

Co=8.3;% Oxygen concentration at the cathode (mol/m^3)

Po=0.21;        % Oxygen pressure at the cathode (atm)

S=0.5;  % Ionic conductivity of synthetic wastewater (S/m)

pHa=8.5;        % Anode pH
```

```
Doa_s=2.06e-9; % Oxygen diffusion coefficient in water (m^2/s)
Koc=3e-5;              % Oxygen mass transfer coefficient in cathode (m/s)
jec=0.003;             % Exchange current density of EtOH on Pt/C (A/m^2)
joc=0.015;             % Exchange current density of oxygen on Pt/C (A/m^2)
Cin=85;                % EtOH concentration in the inlet (mol/m^3)
Cout=[29.8 20.4 17.9 16.2 17.0 27.2 15.3];
                       % EtOH concentration in the outlet (mol/m^3)
d=[0.0005 0.0025 0.0065];          % Electrode spacing (m)
RR=[5.4e-4 0.8e-4 4.4e-4 14e-4 1.4e-4 7.8e-4 3.1e-4];
                       % Separator resistivity (Ω.m^2)
nH=[0.59 0.72 0.92 0.92 0.89 0.62 0.66];
                       % Separator Proton transport number
Ko=[0.29e-6 0.57e-6 0.80e-6 0.97e-6 1.19e-6 0.57e-6 1.87e-6];
                       % Oxygen mass transfer coefficient in the separator (m/s)
Ke=[0.49e-6 0.97e-6 0.84e-6 0.59e-6 2.22e-6 1.02e-6 1.93e-6];
                       % EtOH mass transfer coefficient in the separator (m/s)
```

Calculation of the cathode pH

```
for i=1:N
   deltaCOH(i)=(1-nH(i))*10/(0.05*F);
   COH(i)=10^(-5.5)+deltaCOH(i);
   pHc(i)=-log10(10^(-14)/COH(i));
end
```

Calculation of the average ethanol concentration

```
for i=1:N
   Ce(i)=(Cin-Cout(i))/(log(Cin)-log(Cout(i)));
end
```

Experimental data

```
Jexp(:,:,1)=[ 1.5   1.35  1.15  0.74  0.43  0.16  0.05  0.02;...
              1.17  1.00  0.83  0.39  0.15  0.09  0.03  0.01;...
              1.01  0.87  0.69  0.34  0.17  0.05  0.04  0.01;...
              1.10  0.88  0.67  0.49  0.31  0.12  0.02  0.01;...
              0.89  0.7   0.53  0.38  0.23  0.13  0.03  0.01;...
              1.20  1.01  0.81  0.41  0.17  0.09  0.04  0.01;...
              0.67  0.52  0.38  0.28  0.19  0.12  0.03  0.01];

Jexp(:,:,2)=[ 1.59  1.45  1.21  0.69  0.33  0.12  0.04  0.02;...
              1.32  1.15  0.91  0.42  0.20  0.11  0.05  0.02;...
              1.31  1.15  0.92  0.52  0.28  0.09  0.04  0.02;...
              1.16  0.99  0.83  0.53  0.22  0.08  0.04  0.01;...
              1.02  0.84  0.64  0.45  0.25  0.06  0.03  0.03;...
              1.22  1.00  0.80  0.43  0.20  0.13  0.08  0.03;...
              0.89  0.70  0.48  0.33  0.18  0.13  0.03  0.01];
```

```
Jexp(:,:,3)=[ 1.74  1.57  1.25  0.62  0.30  0.13  0.05  0.02;...
              1.31  1.16  0.92  0.48  0.22  0.09  0.03  0.02;...
              0.84  0.72  0.57  0.31  0.17  0.10  0.05  0.02;...
              1.32  1.15  0.93  0.74  0.55  0.21  0.05  0.01;...
              1.25  1.08  0.85  0.64  0.44  0.24  0.05  0.03;...
              1.46  1.19  0.90  0.44  0.22  0.06  0.03  0.01;...
              1.54  1.38  1.12  0.60  0.21  0.05  0.03  0.01];

Eexp(:,:,1)=[0.1  0.15  0.2   0.3   0.4   0.5   0.6   0.7;...                    0.1  0.15  0.2   0.3   0.4
0.5   0.6   0.65;...
             0.1  0.15  0.2   0.3   0.4   0.45  0.5   0.54;...
             0.1  0.15  0.2   0.25  0.3   0.4   0.5   0.54;...
             0.1  0.15  0.2   0.25  0.3   0.35  0.4   0.46;...
             0.1  0.15  0.2   0.3   0.4   0.5   0.55  0.57;...
             0.1  0.15  0.2   0.25  0.3   0.35  0.4   0.44];

Eexp(:,:,2)=[0.1  0.15  0.2   0.3   0.4   0.5   0.6   0.7;...
             0.1  0.15  0.2   0.3   0.4   0.5   0.6   0.7;...
             0.1  0.15  0.2   0.3   0.4   0.5   0.55  0.57;...
             0.1  0.15  0.2   0.3   0.4   0.5   0.55  0.57;...
             0.1  0.15  0.2   0.25  0.3   0.35  0.4   0.47;...
             0.1  0.15  0.2   0.3   0.4   0.5   0.55  0.6;...
             0.1  0.15  0.2   0.25  0.3   0.35  0.41  0.45];
```

```
Eexp(:,:,3)=[0.1  0.15  0.2   0.3   0.4   0.5   0.6   0.7;...
             0.1  0.15  0.2   0.3   0.4   0.5   0.6   0.7;...
             0.1  0.15  0.2   0.3   0.4   0.5   0.6   0.62;...
             0.1  0.15  0.2   0.3   0.4   0.5   0.54  0.58;...
             0.1  0.15  0.2   0.25  0.3   0.4   0.45  0.49;...
             0.1  0.15  0.2   0.3   0.4   0.5   0.55  0.6;...
             0.1  0.15  0.2   0.25  0.3   0.4   0.45  0.47];
```

Initial values for the anode potential

```
Ea0(:,:,1)=[-0.05 -0.07 -0.08 -0.12 -0.15 -0.18 -0.22 -0.25;...
            -0.05 -0.06 -0.08 -0.11 -0.14 -0.18 -0.21 -0.24;...
            -0.04 -0.05 -0.06 -0.08 -0.11 -0.13 -0.16 -0.18;...
            -0.03 -0.04 -0.06 -0.08 -0.10 -0.12 -0.14 -0.16;...
            -0.03 -0.04 -0.05 -0.07 -0.09 -0.12 -0.14 -0.16;...
            -0.05 -0.06 -0.08 -0.11 -0.14 -0.18 -0.21 -0.24;...
            -0.03 -0.04 -0.05 -0.07 -0.08 -0.10 -0.12 -0.14];

Ea0(:,:,2)=[-0.06 -0.07 -0.09 -0.13 -0.17 -0.20 -0.24 -0.28;...
            -0.05 -0.07 -0.09 -0.12 -0.16 -0.19 -0.23 -0.26;...
            -0.05 -0.07 -0.08 -0.12 -0.15 -0.18 -0.22 -0.25;...
            -0.05 -0.06 -0.08 -0.11 -0.14 -0.17 -0.12 -0.23;...
            -0.04 -0.06 -0.07 -0.10 -0.13 -0.16 -0.19 -0.22;...
            -0.05 -0.07 -0.09 -0.12 -0.16 -0.19 -0.23 -0.26;...
            -0.04 -0.05 -0.07 -0.09 -0.12 -0.14 -0.17 -0.20];
```

```
Ea0(:,:,3)=[-0.06 -0.09 -0.13 -0.16 -0.19 -0.22 -0.25 -0.29;...
        -0.05 -0.08 -0.11 -0.15 -0.18 -0.21 -0.24 -0.27;...
        -0.04 -0.08 -0.11 -0.14 -0.18 -0.21 -0.24 -0.27;...
        -0.04 -0.07 -0.11 -0.14 -0.17 -0.21 -0.24 -0.28;...
        -0.04 -0.07 -0.11 -0.14 -0.17 -0.21 -0.24 -0.27;...
        -0.05 -0.08 -0.11 -0.15 -0.18 -0.21 -0.24 -0.27;...
        -0.03 -0.07 -0.10 -0.14 -0.17 -0.20 -0.24 -0.27];
```

The optimization loop

```
x0=zeros(1,1:8+N*M*K);
x0(1,1:8)=[1e-3 1e-3 1e-5 1e-5 1e-4 1e-4 1e-4 1e-4];

mel=0;
for i=1:N
   for j=1:M
      for k=1:K
         mel=mel+1;
         x0(1,8+mel)=Ea0(i,j,k);
      end
   end
end

options = optimset('Display','iter');
tic
```

```
[x,fval] = fmincon('myfun',x0,[],[],[],[],[1e-4 1e-4 1e-6 1e-6 1e-4 1e-4 1e-4 1e-4 -
0.4.*ones(1,N*M*K)],[1 1 1e-4 1e-4 0.999 0.999 0.999 0.999 0*ones(1,N*M*K)],[],options);
toc

end

save data joa jea Koa_b Kea_b Ea Ec Jpred jec joc alfaea alfaec alfaoa alfaoc
```

Voltage and charge balance equations

```
function f = myfun(x)

global Ea joa jea Koa_b Kea_b Ec Jae Jao Jco Jce Po Eoc0 Eoa0 Eec0 Eea0 alfaea alfaec alfaoa
alfaoc jec joc

global N M K R T ne no F Co d Ce pHa pHc Doa_s Kea_s Ko Jexp Jpred RR Ke Koc  S Eexp Eohm
Jmtea Jmtoa Jmtec Jmtoc Jctea Jctoa Jctec Jctoc

joa=x(1);
joa=x(1);
jea=x(2);
Koa_b=x(3);
Kea_b=x(4);
alfaea=x(5);
alfaec=x(6);
alfaoa=x(7);
alfaoc=x(8);

mel=0;
```

```
for i=1:N
   for j=1:M
      for k=1:K
         mel=mel+1;
         Ea(i,j,k)=x(8+mel);
      end
   end
end

for k = 1:K
   for j=1:M
      for i=1:N
Jmtea(i,j,k)=ne*F*Kea_b*Ce(i);
         % Limiting current of EtOH oxidation at the anode (A/m^2)
Jmtoa(i,j,k)=no*F*(1/(1/Koc+1/Koa(i)+d(k)/Doa_s+1/Koa_b))*Co;
         % Limiting current of oxygen reduction at the anode (A/m^2)
Eea0(i,j,k)=0.084-R*T/(ne*F)*log(Ce(i)/1000/(10^(-pHa))^ne);
         % Equilibrium potential of ethanol oxidation at the anode (V vs. SHE)
Eec0(i,j,k)=0.084-R*T/(ne*F)*log(Ce(i)/1000/(10^(-pHc(i)))^ne);
         % Equilibrium potential of ethanol oxidation at the cathode (V vs. SHE)
Eoc0(i,j,k)=0.401-R*T/(no*F)*log((10^(pHc(i)-14))^no/Po);
         % Equilibrium potential of oxygen reduction at the cathode (V vs. SHE)
Eoa0(i,j,k)=0.401-R*T/(no*F)*log((10^(-14+pHa))^no/Co/1000);
         % Equilibrium potential of oxygen reduction at the anode (V vs. SHE)
```

```
Jctea(i,j,k)=jea*(exp(alfaea*2*F*(Ea(i,j,k)-Eea0(i,j,k))/R/T)-exp((-(1-alfaea))*2*F*(Ea(i,j,k)-
Eea0(i,j,k))/R/T));
        % Kinetically-controlled current of ethanol oxidation at the anode (A/m2)
Jctoa(i,j,k)=joa*(exp(alfaoa*2*F*(Ea(i,j,k)-Eoa0(i,j,k))/R/T)-exp((-(1-alfaoa))*2*F*(Ea(i,j,k)-
Eoa0(i,j,k))/R/T));
        % Kinetically-controlled current density of oxygen reduction at the anode (A/m2)
Jae(i,j,k)=((Jmtea(i,j,k))*abs(Jctea(i,j,k)))/((Jmtea(i,j,k))+abs(Jctea(i,j,k)));
        % Current density of EtOH oxidation at the anode (A/m2)
Jao(i,j,k)=((Jmtoa(i,j,k))*abs(Jctoa(i,j,k)))/((Jmtoa(i,j,k))+abs(Jctoa(i,j,k)));
        % Current density of oxygen reduction at the anode (A/m2)
Jpred(i,j,k)=(Jae(i,j,k)-Jao(i,j,k));
        % Current density predicted by the model (A/m2)
rr(i)=RR(i)+d(k)/S;
        % Resistivity of the MFC (Ω.m2)
Eohm(i,j,k)=Jpred(i,j,k).*rr(i);
        % Ohmic overpotential of the MFC (Ω.m2)
Ec(i,j,k)=Ea(i,j,k)+Eexp(i,j,k)+Eohm(i,j,k);
        % Cathode potential through cell voltage balance (V vs. SHE)
Jmtoc(i,j,k)=no*F*Koc*Co;
        % Limiting current density of oxygen reduction at the cathode (A/m2)
Jmtec(i,j,k)=ne*F*Kea(i)*Ce(i);
        % Limiting current density of EtOH oxidation at the cathode (A/m2)
Jctec(i,j,k)=jec*(exp(alfaec*2*F*(Ec(i,j,k)-Eec0(i,j,k))/R/T)-exp((-(1-alfaec))*2*F*(Ec(i,j,k)-
Eec0(i,j,k))/R/T));
        % Kinetically-controlled current density of EtOH oxidation at the cathode (A/m2)
```

```
Jctoc(i,j,k)=joc*(exp(alfaoc*2*F*(Ec(i,j,k)-Eoc0(i,j,k))/R/T)-exp((-(1-alfaoc))*2*F*(Ec(i,j,k)-
Eoc0(i,j,k))/R/T));
        % Kinetically-controlled current density of oxygen reduction at the cathode (A/m^2)
Jco(i,j,k)=((Jmtoc(i,j,k))*abs(Jctoc(i,j,k)))/((Jmtoc(i,j,k))+abs(Jctoc(i,j,k)));
        % Current density of oxygen reduction at the cathode (A/m^2)
Jce(i,j,k)=((Jmtec(i,j,k))*abs(Jctec(i,j,k)))/((Jmtec(i,j,k))+abs(Jctec(i,j,k)));
        % Current density of EtOH oxidation at the cathode (A/m^2)
      end
   end
end

f = 0;
for i = 1:N
   for k=1:K
      for j=1:M
         f = f+abs(Jae(i,j,k)-Jao(i,j,k)-
                  Jco(i,j,k)+Jce(i,j,k))^2+abs((Jexp(i,j,k)-Jpred(i,j,k)))^2;
      end
   end
end

end
```

B.2 Sensitivity analysis

```
clear all
close all
```

```
clc
format long

global Ea Ec joa jea Koa_b Kea_b Po Eoc0 Eoa0 Eec0 Eea0 alfaea alfaec alfaoa alfaoc jec joc

global N M K R T ne no F Co d S RR Ce pHa pHc Doa_s Koc Koa Kea Jexp Jpred Eexp Eohm Jmtea
Jmtoa Jmtec Jmtoc Jctea Jctoa Jctec Jctoc Jao Jae Jce Jco
```

Parameters and variables

N=1; % # of membranes

M=8; % # of data points for each membrane

K=1; % # of fuel cells

R=8.314; % Universal gas constant (J/mol/K)

T=303; % Temperature (K)

ne=12; % # of electrons transferred in EtOH oxidation

no=4; % # of electrons transferred in oxygen reduction

F=96485.3; % Faraday constant (C/mol)

Co=8.3;% Oxygen concentration at the cathode (mol/m^3)

Po=0.21; % Oxygen pressure at the cathode (atm)

S=0.5; % Ionic conductivity of synthetic wastewater (S/m)

pHa=8.5; % Anode pH

Doa_s=2.06e-9; % Oxygen diffusion coefficient in water (m^2/s)

Koc=3e-5; % Oxygen mass transfer coefficient in cathode (m/s)

jec=0.003; % Exchange current density of EtOH on Pt/C (A/m^2)

joc=0.015; % Exchange current density of oxygen on Pt/C (A/m^2)

Cin=85; % EtOH concentration in the inlet (mol/m^3)

Cout=[ ]; % EtOH concentration in the outlet (mol/m^3)

d=[ ]; % Electrode spacing (m)

RR=[ ]; % Separator resistivity ($\Omega.m^2$)

nH=[ ]; % Separator Proton transport number

Ko=[ ]; % Oxygen mass transfer coefficient in the separator (m/s)

Ke=[ ]; % EtOH mass transfer coefficient in the separator (m/s)

Calculation of the cathode pH

```
deltaCOH=(1-nH)*10/(0.05*F);

COH=10^(-5.5)+deltaCOH;

pHc=-log10(10^(-14)/COH);
```

Calculation of the average ethanol concentration

```
Ce=(Cin-Cout)/(log(Cin)-log(Cout));
```

Voltage values

```
Eexp(:,:,3)=[0.1   0.15   0.20   0.30   0.40   0.50   0.60   0.70];
```

Initial values for the anode potential

```
Ea0(:,:,3)=[-0.05 -0.07 -0.08 -0.12 -0.15 -0.18 -0.22 -0.25];
```

Calculation of the anode potential

```
mel=0;
for i=1:N;
        for k=1:3
                dd=d(k);
                for j=1:M
        mel=mel+1;
        x0(1,mel)=Ea0(i,j,k);
                end
        end
```

```
end

options = optimset('Display','iter');

[x,fval] = fsolve('myfun1',x0,options);
```

Voltage and charge balance equations

```
function f = myfun1(x)

global Ea joa jea Koa_b Kea_b Ec Jae Jao Jco Jce Po Eoc0 Eoa0 Eec0 Eea0 alfaea alfaec alfaoa
alfaoc jec joc

global N M K R T ne no F Co d Ce pHa pHc Doa_s Kea_s Ko Jexp Jpred RR Ke Koc S Eexp Eohm
Jmtea Jmtoa Jmtec Jmtoc Jctea Jctoa Jctec Jctoc

for k = 1:K
   for j=1:M
      for i=1:N
Jmtea(i,j,k)=ne*F*Kea_b*Ce(i);
        % Limiting current of EtOH oxidation at the anode (A/m^2)
Jmtoa(i,j,k)=no*F*(1/(1/Koc+1/Koa(i)+d(k)/Doa_s+1/Koa_b))*Co;
        % Limiting current of oxygen reduction at the anode (A/m^2)
Eea0(i,j,k)=0.084-R*T/(ne*F)*log(Ce(i)/1000/(10^(-pHa))^ne);
        % Equilibrium potential of ethanol oxidation at the anode (V vs. SHE)
Eec0(i,j,k)=0.084-R*T/(ne*F)*log(Ce(i)/1000/(10^(-pHc(i)))^ne);
        % Equilibrium potential of ethanol oxidation at the cathode (V vs. SHE)
Eoc0(i,j,k)=0.401-R*T/(no*F)*log((10^(pHc(i)-14))^no/Po);
        % Equilibrium potential of oxygen reduction at the cathode (V vs. SHE)
```

```
Eoa0(i,j,k)=0.401-R*T/(no*F)*log((10^(-14+pHa))^no/Co/1000);
        % Equilibrium potential of oxygen reduction at the anode (V vs. SHE)
Jctea(i,j,k)=jea*(exp(alfaea*2*F*(Ea(i,j,k)-Eea0(i,j,k))/R/T)-exp((-(1-alfaea))*2*F*(Ea(i,j,k)-
Eea0(i,j,k))/R/T));
        % Kinetically-controlled current of ethanol oxidation at the anode (A/m^2)
Jctoa(i,j,k)=joa*(exp(alfaoa*2*F*(Ea(i,j,k)-Eoa0(i,j,k))/R/T)-exp((-(1-alfaoa))*2*F*(Ea(i,j,k)-
Eoa0(i,j,k))/R/T));
        % Kinetically-controlled current density of oxygen reduction at the anode (A/m^2)
Jae(i,j,k)=((Jmtea(i,j,k))*abs(Jctea(i,j,k)))/((Jmtea(i,j,k))+abs(Jctea(i,j,k)));
        % Current density of EtOH oxidation at the anode (A/m^2)
Jao(i,j,k)=((Jmtoa(i,j,k))*abs(Jctoa(i,j,k)))/((Jmtoa(i,j,k))+abs(Jctoa(i,j,k)));
        % Current density of oxygen reduction at the anode (A/m^2)
Jpred(i,j,k)=(Jae(i,j,k)-Jao(i,j,k));
        % Current density predicted by the model (A/m^2)
rr(i)=RR(i)+d(k)/S;
        % Resistivity of the MFC (Ω.m^2)
Eohm(i,j,k)=Jpred(i,j,k).*rr(i);
        % Ohmic overpotential of the MFC (Ω.m^2)
Ec(i,j,k)=Ea(i,j,k)+Eexp(i,j,k)+Eohm(i,j,k);
        % Cathode potential through cell voltage balance (V vs. SHE)
Jmtoc(i,j,k)=no*F*Koc*Co;
        % Limiting current density of oxygen reduction at the cathode (A/m^2)
Jmtec(i,j,k)=ne*F*Kea(i)*Ce(i);
        % Limiting current density of EtOH oxidation at the cathode (A/m^2)
```

```
Jctec(i,j,k)=jec*(exp(alfaec*2*F*(Ec(i,j,k)-Eec0(i,j,k))/R/T)-exp((-(1-alfaec))*2*F*(Ec(i,j,k)-
Eec0(i,j,k))/R/T));
        % Kinetically-controlled current density of EtOH oxidation at the cathode (A/m^2)
Jctoc(i,j,k)=joc*(exp(alfaoc*2*F*(Ec(i,j,k)-Eoc0(i,j,k))/R/T)-exp((-(1-alfaoc))*2*F*(Ec(i,j,k)-
Eoc0(i,j,k))/R/T));
        % Kinetically-controlled current density of oxygen reduction at the cathode (A/m^2)
Jco(i,j,k)=((Jmtoc(i,j,k))*abs(Jctoc(i,j,k)))/((Jmtoc(i,j,k))+abs(Jctoc(i,j,k)));
        % Current density of oxygen reduction at the cathode (A/m^2)
Jce(i,j,k)=((Jmtec(i,j,k))*abs(Jctec(i,j,k)))/((Jmtec(i,j,k))+abs(Jctec(i,j,k)));
        % Current density of EtOH oxidation at the cathode (A/m^2)
      end
   end
end

for i=1:N
   for k=1:K
      for j=1:M
         f(i,j,k)=Jae(i,j,k)-Jao(i,j,k)-Jco(i,j,k)+Jce(i,j,k);
      end
   end
end


end
```